Studies of magneto-tunneling into donor states and of the breakdown of the quantum Hall effect.

by

Laurie Alan Dickinson B.Sc.

Submitted to the University of Nottingham for the degree of doctor of philosophy in February 2004

Acknowledgments

It is impossible to thank all the people that helped me finish this work. The following people are therefore those without whose help I couldn't have done this. The successive heads of department Professor P. C. Main and Professor P. Beton for providing the facilities for this research. Thank you to my understanding supervisors Professor L. Eaves and Professor P. C. Main. In the lab things went that bit more smoothly and with a smile thanks to Oleg, Amalia and Andreas. I need to thank Professor F. W. Sheard for all the helpful discussions we had and I definitely need to thank Andy Martin for all the countless chats, brainstorms and proof reading that we embarked upon. Thanks to my family for basically everything. Finally, I say thank you to Dave Clubb my partner in crime and physics whose friendship was a constant source of fun and inspiration. Cheers Butt.

Contents

Abstract

This thesis describes an experimental investigation and analysis of two topical problems in condensed matter physics: 1.) the effect of a magnetic field on quantum states of an electron bound to a shallow donor impurity in a quantum well heterostructure and 2.) the breakdown of the quasi-dissipationless state of the integer quantum Hall effect. Two introductory chapters describe important material parameters and the experimental equipment and techniques used. Magneto-tunneling spectroscopy (MTS) is used to probe the spatial form of the eigenfunction of electrons bound in the ground state of a shallow Si-donor impurities in a GaAs/(AlGa)As quantum well. An in-plane magnetic field, $B_{\perp}$, acts to tune the k-vector of the tunnelling electron through the effect of the Lorentz force. The variation with $B_{\perp}$ of the tunnel current through the donor ground state provides a map of the Fourier transform, $|\Psi(k)|^2$, of the probability density of the ground state donor wavefunction in real space. By applying a strong magnetic field component, $B_{||}$, parallel to the direction of tunnel current, it is possible to magneto-compress the donor function in real space. The magneto-compression is investigated using MTS and the data are analysed in terms of a simple model, which is critically discussed.

The breakdown of the integer quantum Hall effect is investigated by measuring the variation of the voltage drop V_{xx} along the direction of current flow for a range of currents and magnetic fields and for a number of sample geometries including Hall bars with narrow channels. The data are discussed in terms of two complementary models of breakdown: the bootstrap electron heating model and magneto-exciton formation at a charged impurity. Evidence is found for both types of breakdown depending on the type of sample used and on experimental parameters. For samples with constrictions, it is found that in the breakdown region the value of V_{xx} measured across a pair of contacts on one side of the Hall bar can differ substantially from that measured on the other side. A model based on magneto-exciton formation at impurities is proposed to explain this unexpected effect. The thesis concludes with a brief summary and suggestions for future work.

Chapter 1

Introduction

1.1 Thesis overview

Two topics have been investigated in the course of this research: one, magneto-tunneling spectroscopy in tilted magnetic fields, used to study the form of the wave-functions of electrons bound to a donor in a quantum well; the other, the breakdown of the quantum Hall effect. The thesis is arranged in the following way. In chapter 1, I introduce the topics and motivation behind this research. Then the properties of gallium arsenide (GaAs) and aluminum gallium arsenide (AlGa)As are discussed. Next the GaAs/(AlGa)As interface is discussed followed by the classical Hall effect. Finally, I deal with the quantum mechanical treatment of electrons in a magnetic field.

In chapter 2 the experimental facilities and sample specification are discussed. This includes a brief outline of the magnetic field facilities followed by a synopsis of the electrical measurement techniques used. Finally, the specifications of the samples measured are outlined.

The first of the experimental results are shown in chapter 3. We start by looking at tunneling in GaAs/(AlGa)As heterostructures, where the simple case of a potential barrier is used to introduce tunneling transport. Next, a transfer Hamiltonian method is presented to describe resonant tunneling through introducing a quantum

well (QW), which is followed by an overview of how the transfer Hamiltonian method can be applied to a real system. Magneto-tunneling spectroscopy (MTS) was used to map the probability density of Si-donors in GaAs by Sakai et al. [1]. To analyse the data we use a different analysis of MTS compared to that of Sakai et al. and determine a slightly different result for the extent of the donor state wavefunction. We then consider MTS in tilted magnetic fields. We show that by using a tilted magnetic field we are able to both compress and map the changing of the donor state. The experimental results for the tilted field measurements show that the proposed model describes the magneto-compression of the donor states, providing an unexpectedly small tunneling distance of 13.5nm is assumed.

Chapter 4 provides an introduction to the quantum Hall effect (QHE) and quantum Hall effect breakdown (QHBD). The QHE is described from an edge state perspective first of all, followed by a description of what actually constitutes quantum Hall effect breakdown (QHBD). The critical current I_c, defined as when the voltage taken along the sample, V_{xx}, starts showing significant dissipation, is used to describe the QHBD. A review of some of the previous work is presented. To aid the structure and for quick reference the review has been split into categories on which the critical current of the QHBD has been found to depend. These are temperature, magnetic field, width and length A final section discusses step-like breakdown. Finally, two models which attempt to describe the many features of the QHBD are described. The first model is the bootstrap electron heating (BSEH) model proposed by Komiyama [2]. BSEH is a model that considers QHBD to be macroscopic in nature. In contrast a microscopic model that considered quasi elastic inter-Landau level scattering (QUILLS) has been extended by Martin et al. [3] by considering the generation of electron-hole pairs or magneto-excitons near an impurity. Both the strengths and deficiencies of the models are highlighted from an experimental viewpoint.

The experimental results for QHBD are presented in chapter 5. The results have been divided into two categories. The first category relates to results that show a step-like nature in the QHBD. Such behavior can only easily be explained using a microscopic model and is therefore labelled 'microscopic breakdown of the quantum

Hall effect'. The properties and dimensions of two samples that showed clear step-like features are shown, followed by an outline of the nature, size and reproducibility of the steps. Finally the step-like nature of the results is discussed and explained in terms of the microscopic model of Martin et al. [3]. The second category of results are from a series of samples containing constrictions. This section has been labelled 'Reconciling the QUILLS and BSEH models'. The reasons why we believe the macroscopic BSEH process will be suppressed in short narrow constrictions are stated [4]. A description of precisely how the critical current is measured follows. The constriction samples were found to display several interesting features in the longitudinal voltage. These are an identity in V_{xx} ($\pm 0.1\%$) measured using contact pairs on the directly opposite sample edge for narrow constrictions, however, wide constriction samples showed a significant difference in V_{xx} measured on the opposite sample edge and a changing dependence of the critical current I_c on the sample width was observed. For narrow samples w<50μm, the width dependence $I_c(w)$, was logarithmic. In the wider samples, the width dependence $I_c(w)$, was linear as predicted by BSEH. Finally the results are discussed in terms of the microscopic and macroscopic models.

A summary of the conclusions and suggestions for further work are given in chapter 6.

1.1.1 Magneto-tunneling spectroscopy in tilted magnetic fields

Classically, an electron incident upon a potential barrier cannot pass the barrier if its energy is lower than that of the barrier. Quantum mechanically, however, the electron will have a finite probability of passing the barrier even if its energy is less than the height of the barrier. An electron of energy less than the barrier height is said to tunnel through the barrier. The probability that the electron tunnels through the barrier decreases exponentially with decreasing energy and increasing barrier height and thickness.

Adding a second barrier creates a potential well between the two barriers. Such

a structure can be made on the nanometer scale by sandwiching a layer of GaAs in-between two layers of (AlGa)As using the molecular beam epitaxy growth technique. An electron incident at a barrier outside the well can tunnel into the well where it will reside on one of the quasi-bound states of the well. After a time the electron may tunnel out of the well via one of the barriers. If the energy of the tunneling electron is coincident with the energy of the quasi bound state then the probability of the electron tunneling through the potential well is significantly increased; such a process is known as resonant tunneling and these devices are called resonant tunneling diodes (RTDs). RTDs are not only of fundamental interest but also have potential of applications as high frequency ($\backsim$ 100GHz) oscillators, mixers [5], [6] and have applications in biology and medicine [7].

Silicon acts as a substitutional donor (Si_{Ga}) state when placed in GaAs, relinquishing its spare 3p electron easily to the crystal to become ionised at all but low temperatures, $T > 20K$. By introducing δ-doped silicon into the central plane of a GaAs potential well new states are available for electrons to resonantly tunnel through. These states lie at a lower energy than the ground state subband of the potential well.

Applying a bias to the well increases the energy of the incident electrons. As the bias voltage is increased, peaks in the transmission of the electrons can be seen in the current-voltage characteristics, I(V). These peaks occur when the energy of the tunneling electrons equals the energy of a bound state within the potential well. Therefore using the bias voltage it is possible to tune the electrons so that they tunnel through a chosen state within the well.

In a magneto-tunnelling spectroscopy experiment (MTS), a magnetic field $B_\perp$ is applied perpendicular to the tunnel current. Due to the action of the Lorentz force that the magnetic field imparts on the tunneling electron, a change of the in-plane momentum occurs, given by $\hbar k = eB_\perp \Delta s$, where Δs is the tunneling distance. Measuring the variation of the tunnel current with $B_\perp$ provides a means of determining the size of the matrix element that governs the quantum transition of an electron as

it tunnels from a plane-wave state in the emitter layer into a given quantum state in the well. This variation in size of the square of the matrix element with $B_\perp$ is equivalent to the variation in probability density in Fourier space, $|\varphi(k)|^2$, of the quantum state [8],[1].

Theoretical studies of the states of quantum systems commonly involve the calculation of the eigenvalues and corresponding wavefunctions by solving the Schrödinger equation. Experimental studies, on the other hand, traditionally focus on the measurement of the energies by spectroscopic techniques. The shape and form of the wavefunctions are often measured indirectly by studying, for example, the intensity of spectral lines in optical spectroscopy experiments. Nevertheless, in recent years it has become possible to probe directly the wavefunctions of a quantum system by using novel tunneling spectroscopy techniques, such as scanning tunneling microscopy (STM) and magneto-tunneling spectroscopy. Images of the electronic charge distributions of low-dimensional systems near a surface, such as Si donors in GaAs can be produced using STM [9], [10]. However, for systems deep below a surface this technique turns out to be invasive and destructive [11]. Conversely, magneto-tunneling spectroscopy has proven to be a non-destructive and non-invasive technique to probe the wavefunction of a variety of systems such as quantum wires [12], self-assembled quantum dots [13], [8], and Si donors states in GaAs/(AlGa)As quantum wells [1]. The MTS technique can be regarded as the momentum-space analogue of STM imaging: in the latter, the moving tip acts as the probe of the wave function in real space, whereas in the former the applied magnetic field acts as a variable probe in Fourier space.

A magnetic field applied to a bound electron will create a compression in the wavefunction's spatial extent [14]. This thesis proposes a further development of the MTS technique aimed at probing how a magnetic field modifies the spatial form of the wavefunctions of quantum systems. The tunnel current through Si-donor states in a QW, in the presence of a strong magnetic field applied at various angles to the QW plane is studied. In a simple picture, the component of magnetic field parallel to the current direction, $B_{||}$, provides a means of compressing the donor

wavefunction in real space. The degree of compression is modified by varying $B_{||}$ and the perpendicular component $B_{\perp}$is used to adjust k and thereby map out the momentum-space probability density $|\varphi(k)|^2$ of the donor ground state at different degrees of compression.

1.1.2 Quantum Hall effect breakdown

The quantum Hall effect (QHE) is a remarkable discovery. Sweeping a magnetic field at constant current shows plateaus of in the Hall resistance of $R_{xy} = h/\nu e^2$, where ν is an integer, and quasi-dissipationless regions in the longitudinal voltage V_{xx}, see figure 1-1. The region of magnetic field where a plateau occurs in V_{xy} and V_{xx} is dissipationless is called the plateau region. There are no free parameters or dependence on the sample properties governing the value of the Hall resistance $R_{xy} = V_{xy}/I$, where I is the current passed along the length of the Hall bar. The electrical resistance standard is now defined in terms of the QHE. Consequently, metrologists have great interest in obtaining as accurate as possible measurement of the plateau in V_{xy}. One way of doing this is to use as large a current as possible and therefore measure a large voltage V_{xy}, leading to increased accuracy. However, at a critical current I_c, the QHE breaks down with the Hall plateaus smearing out and the quasi-dissipationless region in the longitudinal voltage jumping by several orders of magnitude to the mV level of dissipation. By understanding the QHE breakdown (QHBD) we will better understand electrical transport in a two-dimensional electron gas (2DEG) and measurements of the Hall resistance can be optimised for greater accuracy.

Due to its importance in science and metrology there has been a lot of work on the QHBD. A recent review of this topic was written by Nachtwei [15]. There have been a multitude of models which attempt to explain breakdown. For example, electron heating [2],[16], percolation due to the increase in delocalised states [17], phonon emission due to intra-Landau scattering [19], formation of compressible metallic filaments [20], inter-Landau level scattering [18] and resonant scattering by impurities [21]. However, as yet there is no single universal model that can fully explain all the

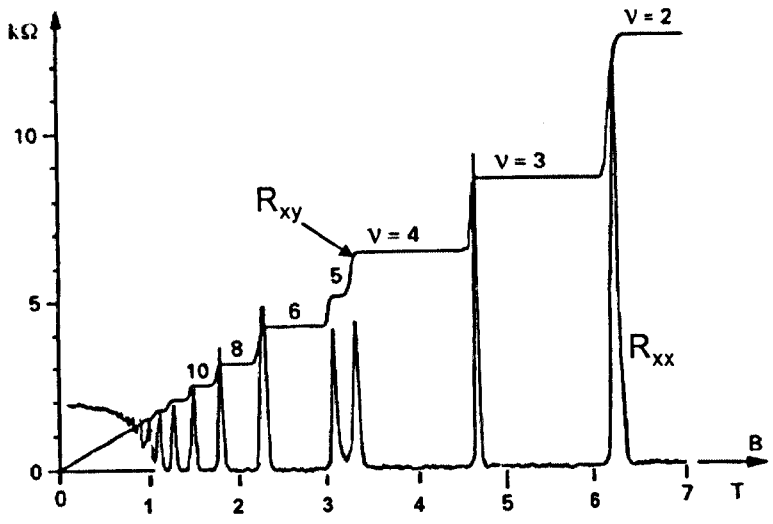

Figure 1-1: The results of the quantum Hall effect. Plateau can be seen in the Hall resistance R_{xy}, accompanied by zeros in the londitudinal resistance R_{xx}. The filling factors ν are labelled. Taken from [22] with adjustments.

features of the QHBD in all experiments. We show here that there exists a state where the breakdown can be considered to be microscopic in nature; this can explain the unusual steps in V_{xx} which are observed in the breakdown of the QHE in the samples used to measure the US resistance standard and in a two-dimensional hole gas (2DHG) sample studied recently at Nottingham.

In this thesis measurements made with standard Hall bars and Hall bars containing short constriction regions are presented. The results are explained using a model based on inter-Landau level tunneling [3]. The results are also compared with that of another model for QHBD, put forward by Komiyama et al, of bootstrap electron heating (BSEH) [2]. It is argued that neither the BSEH model nor the microscopic model proposed can fully explain all the features of QHBD in all the experiments and that a model that can incorporate both is needed. Generally, for long wide samples with medium or low mobilities the BSEH model describes the breakdown most accurately. Samples with constrictions or displaying step-like breakdown are best described by a microscopic model based on the quasi-elastic electron tunneling (QUILLS) [18], of impurity driven inter-Landau level scattering (IDILLS) [3].

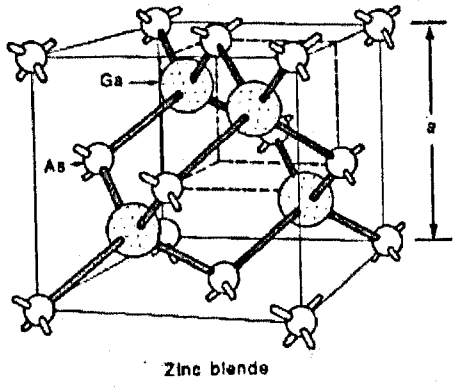

Figure 1-2: The zinc blend structure of the GaAs crystal. The lattice constant is displayed as a. Taken from [23].

1.2 Gallium Arsenide

The devices studied in this thesis are all fabricated from GaAs, (AlGa)As heterostructures. The properties of GaAs and (AlGa)As have been well documented (general texts [24],[23]). The following section is a brief overview of GaAs and some of its properties.

1.2.1 Lattice

The crystal structure of GaAs is such that each gallium atom is bonded to four arsenic atoms in a tetrahedral arrangement. The bonds are predominately covalent in character with a 30% ionic contribution [25]. The compound crystallizes in a zinc-blende structure shown in figure 1-2. The lattice constant a=0.565nm at 300K and the unit volume a^3 contains four atoms of each species. The length of each bond at 300K is $a\sqrt{3}/4 \approx 0.24nm$ [24].

The alloy $(Al_xGa_{1-x})As$, (AlGa)As for short, has a concentration of randomly distributed Al atoms displacing the Ga atoms given as a fraction x, typically $x \leq 0.4$. The lattice mismatch between GaAs and AlAs is very small, about 0.0008nm, allowing almost perfect lattice matching. Consequently, high quality abrupt interfaces can be grown.

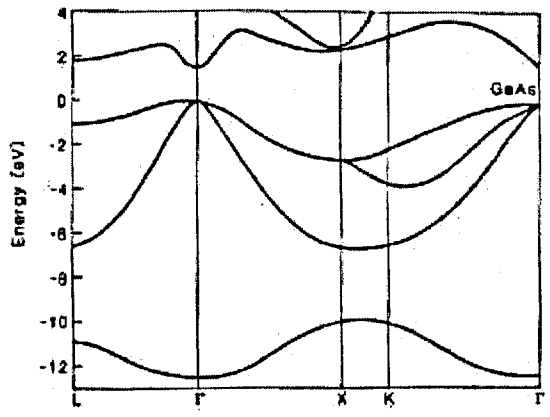

Figure 1-3: The band structure for GaAs. Taken from Davies [24] calculations by Srivastava.

1.2.2 Band structure

The band structure of GaAs is shown in figure 1-3. The Γ minimum in the conduction band lies at the same point in k-space as the maximum in the valence band, at $k = 0$. Consequently, the band gap of GaAs is direct and is 1.424eV at room temperature [24]. The band gap increases with decreasing temperature [25] according to the relation

$$E_g(T)\text{eV} = 1.519\text{eV} - [5.405 \times 10^{-4}T^2/(T + 204)]\text{eV}. \tag{1.1}$$

The other minima in the conduction band of GaAs give the indirect band gaps of the L and X points, which are 1.708eV and 1.900eV respectively. The L and X minima are unlikely to be occupied unless the electric field is very high, so the direct Γ transition is the dominant mechanism in electron excitation. For these reasons the following chapters consider the Γ band gap whenever a band gap is referred to, unless stated otherwise.

The addition of Al to the GaAs creates an increase in the band gaps given by

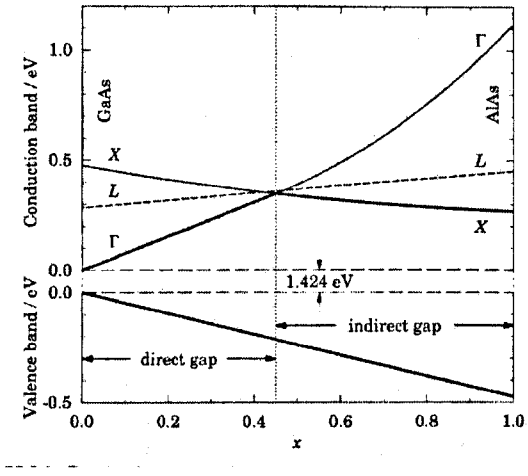

Figure 1-4: Energies of the lowest three conduction bands and top of the valence band in $(Al_xGa_{1-x})As$ as a function of the composition x. Taken from Davies [24].

the following relations

$$E_g^{\Gamma}(\text{eV}) = 1.424 + 1.247x \ (x < 0.45), \tag{1.2}$$

$$E_g^{X}(\text{eV}) = 1.9 + 0.125x + 0143x^2, \tag{1.3}$$

$$E_g^{L}(\text{eV}) = 1.708 + 0.624x, \tag{1.4}$$

where x is the percentage concentration of the Al and all values are in eV. Figure 1-4 shows the valence band and conduction band of GaAs as the concentration of Al is increased. A crossover towards an indirect band gap dominance occurs for concentrations of Al where $x \geqslant 0.43$. All the samples studied in this work used $(Al_xGa_{1-x})As$ where $x < 0.43$. For the samples used to study the quantum Hall effect, x=0.33 and for the samples used to study magneto-tunneling x=0.4. Hence, the regime of high Al concentration is not considered here. The energy gap for the direct Γ gap in the (AlGa)As samples measured in this work is calculated to be 1.84eV and 1.92eV at room temperature for the Al donor concentrations x=0.33 and x=0.4 respectively.

1.2.3 Effective mass

The Schrödinger equation in a crystal with many ions and electrons is difficult to solve. Instead the one-electron approximation is used. The ions are regarded as fixed at their lattice sites and one electron is assumed to move through a potential formed by the ions and all the other electrons. The effective one-electron potential V(**r**) is periodic as would be expected from the nature of the underlying lattice. The Hamiltonian for the electron [24],[23] is given by

$$H\psi(\mathbf{r}) = \left[\frac{\hat{\mathbf{p}}^2}{2m_e} + V(\mathbf{r})\right]\psi(\mathbf{r}) = E\psi(\mathbf{r}), \tag{1.5}$$

where $\hat{\mathbf{p}}$ is the momentum operator, m_e the free electron mass, $V(\mathbf{r})$ the potential incorporating the ions of the lattice and the time-averaged electron potential and $\mathbf{r}$ the position vector. Bloch's theorem states that in such a case the wavefunction is given by

$$\psi(\mathbf{r}) = \exp(i\mathbf{k}\cdot\mathbf{r})u(\mathbf{k},\mathbf{r}), \tag{1.6}$$

where $u(\mathbf{k},\mathbf{r})$ is a function varying with the periodicity of the lattice and $\mathbf{k}$ differs from the case of the free electron as it is the crystal momentum.

Adding random impurities or changing the structure of the crystal, a quantum well for example, invalidates the Bloch function assumption by spoiling the periodicity of the potential. A way round this problem [24] is to consider the wavefunction to consist of a linear combination of Bloch functions

$$\psi(\mathbf{r}) = \sum_n \int_{-\pi/a}^{\pi/a} \chi(\mathbf{k}) u_n(\mathbf{k},\mathbf{r}) e^{i\mathbf{k}\cdot\mathbf{r}} \frac{d\mathbf{k}}{2\pi}, \tag{1.7}$$

where $\chi(\mathbf{k})$ are expansion coefficients. We assume that: only one band contributes significantly to the integral and just a small range of states around $\mathbf{k}$ play a significant part. For the case of GaAs this would be the Γ-minimum with values of $|\mathbf{k}|$ around

$\mathbf{k}$ =0. The wave function now takes the form [24]

$$\psi(\mathbf{r}) = u_n(0,\mathbf{r})\chi(\mathbf{r}), \tag{1.8}$$

where $\chi(\mathbf{r})$ is a Fourier transform of $\chi(\mathbf{k})$. The Γ-minimum in the conduction band of GaAs can be treated as parabolic and isotropic for low energies by

$$\varepsilon_c(\mathbf{k}) = E_c + \frac{\hbar^2\mathbf{k}^2}{2m}, \tag{1.9}$$

where the scalar effective mass at the conduction band edge can be taken as $m \approx 0.067m_e$ [26]. The resulting effective Schrödinger equation for the Γ GaAs minimum can be shown to be

$$\left[-\frac{\hbar^2}{2m}\nabla^2 + V_{imp}(\mathbf{r})\right]\chi(\mathbf{r}) = (E - E_c)\chi(\mathbf{r}). \tag{1.10}$$

The above result is equivalent to that of the free electron case but with the mass of the electron being replaced with the effective mass and the energy is considered relative to the base of the conduction band. This is the result of the effective mass approximation and is used for understanding the results presented in this thesis. For the remainder of the thesis the effective mass approximation will be used. Therefore the function $\chi(\mathbf{r})$ will be often labelled as $\psi(\mathbf{r})$ and termed the wavefunction as the effective mass approximation is being used.

For higher energies, more than a few meV from the band edge it is necessary to take into account the changing non-parabolic band structure with $m(\varepsilon) = m(1+\alpha\varepsilon)$ where m is the effective mass as defined above and $\alpha = 3.26(eV)^{-1}$ and ε is measured from the band edge.

The top of the valence band has a p-orbital type symmetry. Electron motion is therefore anisotropic in general as holes will find it easier to travel in the direction of the bond orientation for example the z direction, than the x and y directions. Thus in the z direction the effective mass is low, and in the x and y directions the electrons travel less freely leading to a larger hole mass. It follows then that there are

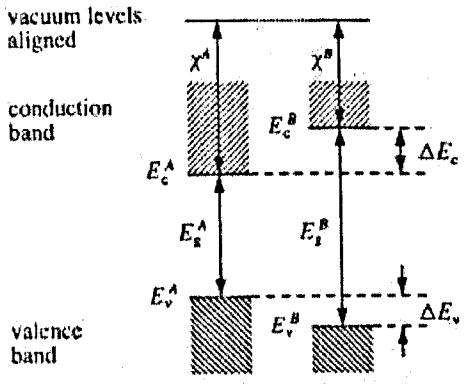

Figure 1-5: The Anderson rule shown for materials A and B. The energies E_c, E_v, E_g and χ correspond to the energy of the conduction, valence, band gap and electron affinity respectively. Davies [24]

two bands of holes, there is a doubly degenerate light hole band, where the energy increases rapidly with k, and a doubly degenerate heavy hole band. At the top of the valence band the light and heavy bands meet. Near Γ, an isotropic and parabolic approximation for the valence band can be made for simplicity which is given by

$$\varepsilon_v(k) = E_v - \frac{\hbar^2 k^2}{2m_h}, \tag{1.11}$$

where m_h is m_{hh} for heavy holes or m_{lh} for light holes. In GaAs $m_{hh} \approx 0.5m_e$ and $m_{lh} \approx 0.082m_e$ [24].

The effective mass in $(Al_xGa_{1-x})As$ can be interpolated from the GaAs value according to the following relation

$$m_{AlGaAs} = 0.067m_e + 0.083xm_e, \tag{1.12}$$

where x is the percentage Ga displacement by the Al. The samples measured in this work had Al percentages of x=0.33%, 0.4%. We can therefore estimate the effective mass of the electrons tunneling through the (AlGa)As at the Γ minimum of the conduction band to be $m_{Al_{0.33}GaAs} = 0.09439m_e$ and $m_{Al_{0.4}GaAs} = 0.1002m_e$.

1.3 The GaAs/(AlGa)As interface

The small lattice mismatch between GaAs and (AlGa)As combined with sample growth by molecular beam epitaxy allows the fabrication of abrupt defect free interfaces between the two materials. The Anderson rule states that the vacuum level of two materials at a heterojunction match each other, see figure 1-5. As GaAs and (AlGa)As have different electron affinities there will be a step-like change in the conduction band accordingly. The (AlGa)As has a smaller electron affinity $\chi = 0.3652eV$ than that of GaAs $\chi = 4.07eV$ and thus a step up in the conduction band edge occurs. Electrons present in the GaAs conduction band will encounter a barrier or potential step of approximately 0.418eV when encountering the (AlGa)As region.

1.3.1 Two dimensional electron gas

Introducing doping, typically silicon for n-type carriers, to (AlGa)As increases the number of delocalised electrons. If the electrons sit on their donors the material is insulating. At finite temperatures this is not the case and the electrons are liberated from the donor sites. For the case of undoped GaAs adjacent to doped (AlGa)As, the electrons can pour into the GaAs until the chemical potentials line up. However, the step in the conduction band between (AlGa)As and GaAs prevents the electrons from returning to the donor sites. The spatial separation of the positively charged donor states and the negatively charged electrons sets up an electrostatic potential which tends to drive the electrons back into the (AlGa)As. The electrons are thus confined in a roughly triangular well in the z direction as indicated by figure 1-6. The energy of an electron relative to the bottom of the conduction band on the GaAs side of the heterojunction is given by

$$E = E_i + \frac{\hbar^2 k_x^2}{2m} + \frac{\hbar^2 k_y^2}{2m} \tag{1.13}$$

where i=0,1,2... and E_i is the quantised energy in the z direction. This equation ignores the effects of impurities but does provide a intuitive guide to the process

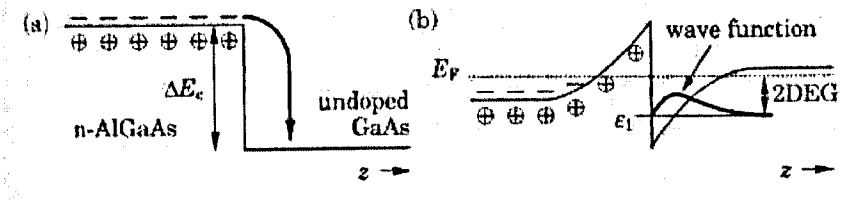

Figure 1-6: The conduction band profile for a modulation-doped (AlGa)As/GaAs heterojunction showing the equalising of the Fermi energies and the formation of a 2DEG. Davies [24]

of forming a 2DEG. The electrons are free to move in the xy direction but not in the z direction. The electrons only take quantised values of kinetic energy in the z direction; they are known as subbands. For low temperatures the separation between subbands can be larger than the Fermi energy and only the lowest subband can be occupied. Motion in the z direction becomes impossible because the electron would need to be in the energetically unfavourable states. Such a system is called a 2DEG.

The disadvantage of the charged donors close to the 2DEG is that they can scatter the electrons through the Coulomb interaction. The motion of the electrons can be inhibited by scattering processes. The devices used through the course of this thesis used modulation doping to minimise this effect. The charged donor states are separated from the 2DEG in the case of the tunneling samples and a spacer layer of (AlGa)As is used in the QHE samples to reduce the Coulomb scattering effects caused by the charged donor atoms.

1.3.2 The tunneling distance of a quantum well with 2DEG emitter states

When using the magneto-tunneling spectroscopy technique (MTS) the precise distance the electrons tunnel is important. If the distance the electrons tunnel is known, the probability density of the state being examined (Si donors in chapter 3) can be measured. For the quantum well systems examined in chapter three, we believe the electrons tunnel from a 2DEG emitter state through the (AlGa)As barrier and into

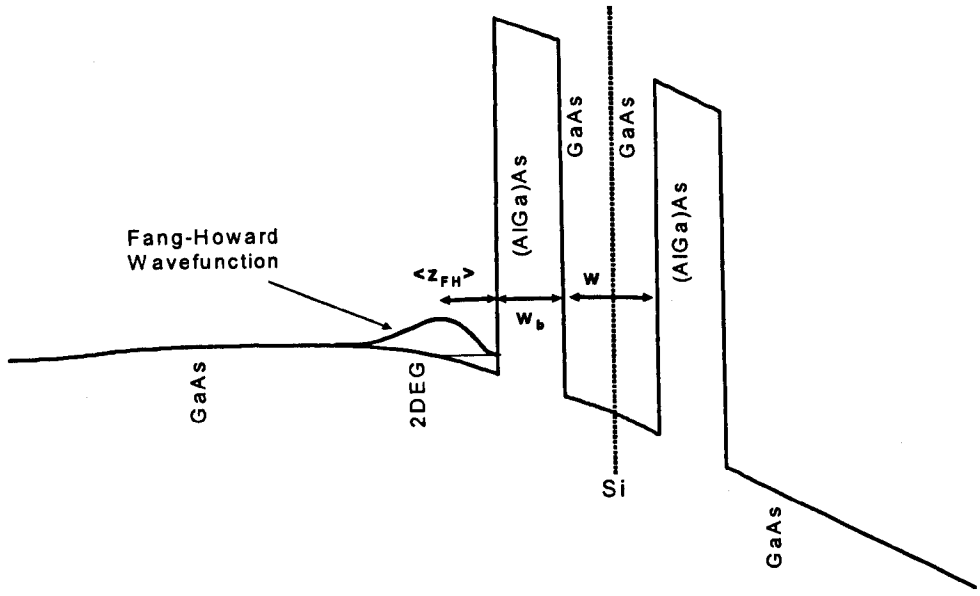

Figure 1-7: A representation of the conduction band profile for a quantum well is shown. The (AlGa)As barriers have a width w_b and the GaAs quantum well has a width w. A delta doping of Si donors is present in the central plane of the quantum well. The emitter state is chosen to be a 2DEG and the Fang-Howard form for the wavefunction is indicated. The average distance of the electrons from the (AlGa)As barrier is indicated by $<z_{FH}>$.

the Si donor states lying in the central plane of a quantum well. The physical boundaries that separate electrons in the 2DEG emitter from the Si donors states are the (AlGa)As barrier width, bw, and half the QW width $w/2$. However, the peak of the 2DEG wavefunction lies at a finite distance, $< z_{FH} >$ from the GaAs/(AlGa)As interface, see figure 1-7. The wavefunction of the 2DEG in the z direction as indicated on figure 1-7 can be described by the Fang-Howard wavefunction,

$$u(z) = \begin{bmatrix} 0 & z < 0 \\ z \exp\left(-\frac{1}{2}bz\right) & z > 0 \end{bmatrix}, \tag{1.14}$$

where b is a unknown parameter. Using a variational method it is possible to calculate the value of the parameter b for the many electron problem of a heterojunction [24]. Thus b is calculated to be

$$b = \left(\frac{33me^2 n_{2D}}{8\hbar^2 \varepsilon_0 \varepsilon_r}\right)^{\frac{1}{3}}, \tag{1.15}$$

where n_{2D} is the areal number density of the electrons, ε_0 is the permittivity of free space and ε_r the relative permittivity of GaAs for our QW structure. Equation 1.15 shows that b depends on the areal electron density, the larger the electron density the larger the value of b. The average position (in the z direction) for electrons in the 2DEG is given by

$$< z_{FH} >= \int_0^\infty z|u(z)|^2 dz = \frac{3}{b}. \tag{1.16}$$

This is an inverse relation to the parameter b and therefore the electron density. In our tunneling experiments we assume that the electrons on average tunnel from a point $< z_{FH} >$ away from the (AlGa)As barrier. The total tunneling distance Δs is therefore given by

$$\Delta s = w_b + w/2 + < z_{FH} > . \tag{1.17}$$

The variational method using Fang-Howard wavefunction has been chosen for its simplicity. The number density of electrons in our tunneling devices is not known exactly. We are able to estimate the number density of electrons from electrostatic models, the determined value is only approximate. Complex calculations which consider the fact that the tail of the wavefunction will enter the (AlGa)As barrier and compensate for the difference in dielectric constant between GaAs and (AlGa)As are possible. However, as the number density is not accurately known, these calculations provide only a marginal increase in accuracy and have not been used.

1.4 The classical Hall effect

Consider a conductor like that shown in figure 1-8. The current I_x in the sample goes from left to right in the x direction. The charge carriers are chosen to be electrons and have a drift velocity v_x. A magnetic field in the z direction causes the electrons

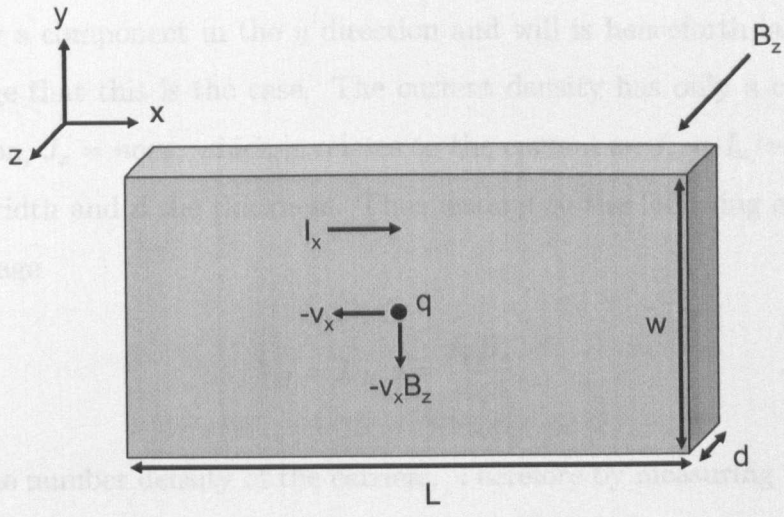

Figure 1-8: A sample of length L, width w, and thickness d is shown. The charge carrier q, its velocity v_x and the force in the y direction due to the magnetic field $-v_x B_z$ are indicated.

to drift to one side of the sample according to the Lorentz force,

$$F_l = q(\mathbf{v} \times \mathbf{B}). \tag{1.18}$$

The charge q is used to keep generality as the only assumption so far is the direction the charge carrier is moving. According to equation 1.18, the charge carriers move in the $-y$ direction, see figure 1-8. One side of the sample now has an excess of electrons (or holes) and the other a deficit. Hence, an electric field is created between the sample sides. This electric field is called the Hall field $\mathbf{E}_H$. Eventually the steady state condition will be reached in which the Hall field balances the Lorentz force. The carriers once again move along the sample with a drift velocity $-v_x$ and are undeviated by the magnetic field. Equating the electric field and Lorentz force we obtain the condition $q(\mathbf{E}_H - (\mathbf{v} \times \mathbf{B})) = 0$ [27] which in the described situation leads to

$$q\mathbf{E}_H = qv_x B_z \tag{1.19}$$

where $\mathbf{E}_H$ is the Hall field and B_z the magnetic field in the z direction. The Hall field has only a component in the y direction and will is henceforth labelled E_H in the knowledge that this is the case. The current density has only a component in the x direction, $J_x = nqv_x$, which is relates to the current as $J_x = I_x/wd$ where w is the sample width and d the thickness. Thus leading to the following expression for the Hall voltage

$$V_H = E_H w = \frac{I_x B_z}{nqd}, \tag{1.20}$$

where n is the number density of the carriers. Therefore by measuring the Hall voltage the type of carrier and its concentration can be deduced and for a precalibrated sample the magnetic field can be determined. The Hall effect is consequently widely used for sample characterisation.

Hall measurements on 2DEG's yield the extraordinary results of the quantum Hall effect. Over quite large ranges of magnetic field the Hall resistance is accurately quantised at values $\mathrm{R}_{xy} = h/\nu e^2$, where ν is an integer Furthermore in the same regions of magnetic field the longitudinal conductivity is zero. A further explanation of the of the quantum Hall effect can be found in chapter 4

1.5 Quantum mechanics of an electron in an uniform magnetic field

Classically, a magnetic field affects an electron system due to the Lorentz force. In a plane perpendicular to the magnetic field, electrons display circular trajectories and in the plane parallel to the magnetic field the motion is unaffected. The quantum mechanical solution for an electron in a magnetic field has a similar result as that of the classical case. However, in the case of a two dimensional system the results show a quantum nature.

The Schrödinger equation for an electron in an electromagnetic field in the effec-

tive mass approximation [24],[28] is given by

$$\left[\frac{1}{2m}\left(-i\hbar\nabla + e\mathbf{A}(\mathbf{r},t)\right)^2 - eV(\mathbf{r},t)\right]\psi(\mathbf{r},t) = i\hbar\frac{\partial}{\partial t}\psi(\mathbf{r},t), \tag{1.21}$$

where V is the scalar potential, $\mathbf{A}$ the vector potential and m the effective mass. For the time independent equation and assuming no electric field, a simple algebraic solution is obtained using the Landau gauge, where the vector potential is given by $\mathbf{A} = (-By, 0, 0)$ which leads to a Schrödinger equation of the form

$$\left(\frac{1}{2m}\left[-\hbar^2\frac{\partial^2}{\partial y^2} + \left(-i\hbar\frac{\partial}{\partial x} + eBy\right)^2 - \hbar^2\frac{\partial^2}{\partial z^2}\right] + V(z)\right)\psi(\mathbf{r}) = E\psi(\mathbf{r}). \tag{1.22}$$

Here the motion along the z direction is unaffected by the magnetic field. This gives

$$\left[-\frac{\hbar^2}{2m}\nabla^2 - \frac{ie\hbar By}{m}\frac{\partial}{\partial x} + \frac{(eBy)^2}{2m} + V(z)\right]\psi(\mathbf{r}) = E\psi(\mathbf{r}). \tag{1.23}$$

The potential V(z) is absent for free electrons. It can, however, be used to describe confinement due to a quantum well or a 2DEG. Generally, the potential in the z direction is unaffected by the magnetic field and as such is additive. Assuming separability of variables we can therefore drop the z term as long as the final wavefunction is multiplied by the function in z and the corresponding energy be added.

The vector potential does not have any dependence on x and we can guess a solution of the form $u(y)exp(ikx)$ for the motion in the x-y plane. Substituting this into the Schrödinger equation shows this is a good solution as the plane wave in x cancels from both sides and we are left with a equation in y only:

$$\left[-\frac{\hbar^2}{2m}\frac{d^2}{dy^2} + \frac{1}{2}m\omega_c^2\left(y + \frac{\hbar k}{eB}\right)^2\right]u(y) = \varepsilon u(y), \tag{1.24}$$

where $\omega_c = |eB/m|$ is the angular cyclotron frequency. Inspection of equation 1.24 shows that it is the Schrödinger equation for a one dimensional simple harmonic oscillator, where the vertex of the parabola has been displaced by $y_k = -\hbar k/eB$. A length scale is defined to aid in the solution of the simple harmonic oscillator [28],

and so we choose the magnetic length to be

$$l_b = \sqrt{\frac{\hbar}{m\omega_c}} = \sqrt{\frac{\hbar}{|eB|}} \tag{1.25}$$

which is independent of the mass of the particle and depends only on the magnetic field. A typical value for a magnetic field of 10T is $l_b \approx 8nm$. The energy and wave function can now be written down for electrons in the x-y plane;

$$\varepsilon_{nk} = (n + \frac{1}{2})\hbar\omega_c, \tag{1.26}$$

$$\phi_{nk}(x, y) \propto H_n\left(\frac{y - y_k}{l_b}\right) \exp\left[-\frac{(y - y_k)^2}{2l_b^2}\right] \exp(ikx), \tag{1.27}$$

where $n = 0, 1, 2, 3$ a positive integer and H_n are Hermite polynomials. The energy in equation 1.26 corresponds to the ideal case where any spatially varying potential fluctuations due the impurity states are not considered. A fundamental feature of equation 1.26 is that the energy depends only on n and not on k. States with the same n but different k are degenerate in the absence of an electric field. The density of states for a two dimensional system therefore collapses into a series of δ functions called Landau levels at energies given by equation 1.26.

Examining equation 1.27 shows that the wavefunctions form into a series of parallel strips in the x direction. The x direction is determined by the choice in vector potential. As the states within a Landau level are all degenerate any linear combination of them remains a solution of the Schrödinger equation with the same energy.

1.5.1 Landau levels

As shown previously, the magnetic field causes the continuous density of states for free electrons to collapse into a series of δ functions called Landau levels. The next section outlines some of the properties of Landau levels.

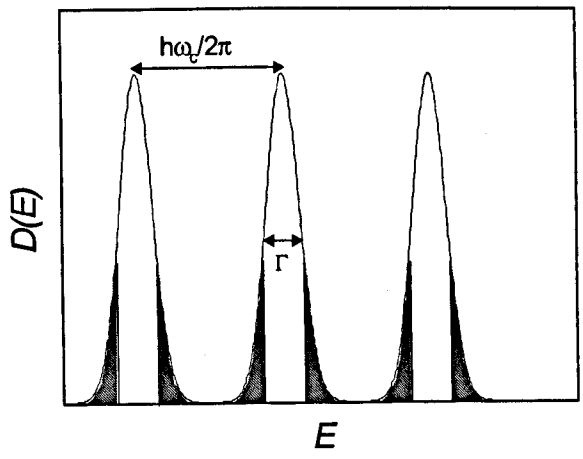

Figure 1-9: The energy distribution of the density of states in a magnetic field showing the Landau level spacing $\hbar\omega_c/2\pi$ and the broadening Γ. The white peaks are the extended states of the Landau levels, the grey tails corresponding to the localised states.

If we consider the boundary conditions of a 2 dimensional sample $L_x \times L_y$ in the Landau gauge, the usual condition in the x direction of $k = (2\pi/L_x)j$, where j is a positive or negative integer, is found. The separation in the y direction is due to the centring of the wave functions on y_k. We require $y_k = \hbar k/eB = -2\pi\hbar j/eBL_x$ is to lie inside the sample [24] so that

$$-L_y < \frac{2\pi\hbar j}{eBL_x} < 0, \qquad \frac{eBL_xL_y}{h} < j < 0. \tag{1.28}$$

Thus the allowed number of states in each Landau level per unit area is given by $n_B = 2|eB/h|$, when spin degeneracy is included. The application of magnetic field does not change the areal electron density. Each block of the constant density of states of width $\hbar\omega_c$ collapses into a δ function containing the same number of states at its centre.

The assumption that the Landau levels are δ functions is only true in the ideal case without disorder. For a real system scattering of the electrons by phonons or impurities causes the Landau levels to be broadened. If the electron has a scattering time τ_i, the single particle lifetime, then the energy can only be defined within the

precision $P = \hbar/\tau_i$, and the Landau levels become broadened. The single particle lifetime treats all collisions as contributing equally. This is different to the transport lifetime used in determining the mobility which considers the change of direction that of the electron momentum. Further broadening can occur due to the impurities within the sample. Extended and localised states within the broadened Landau band are created by the impurities within the Landau levels with a characteristic width of the extended states given by Γ, see figure 1-9. It is thought that $\Gamma > P$ and as such determines the width of the Landau level broadening. It is convenient to define the full width half maximum of the Landau levels to be Γ. The true nature of the Landau levels remains uncertain, common assumptions are that they can be of Gaussian form or Lorentzian in profile [24]. The limit between classical behavior in magnetic fields and quantum behavior is defined as $\hbar\omega_c > \Gamma$. Or it can also be written $\omega_c\tau_i > 1$ which shows that an electron must make at least one full orbit in the magnetic field for the quantum regime to be achieved.

1.5.2 The filling factor

Increasing the magnetic field increases both the Landau level separation and the number of states each Landau level can hold. Normally the areal density of electrons within the system is constant. As the magnetic field is increased more states become available in the Landau levels lying lowest in energy and the electrons depopulate the highest Landau level in favour of the lowest available state. The filling factor of the Landau levels therefore changes with changing magnetic field. The number of filled Landau levels or filling factor ν can be written as

$$\nu = \frac{n_{2D}}{n_B} = \frac{hn_{2D}}{eB}, \tag{1.29}$$

where the spin split levels are considered as separate levels.

We consider the case where there is an absence of disorder, the Landau levels are infinitely sharp. With increasing magnetic field, the highest populated Landau levels depopulate in a step wise fashion as shown in figure 1-10. The Fermi energy lies with

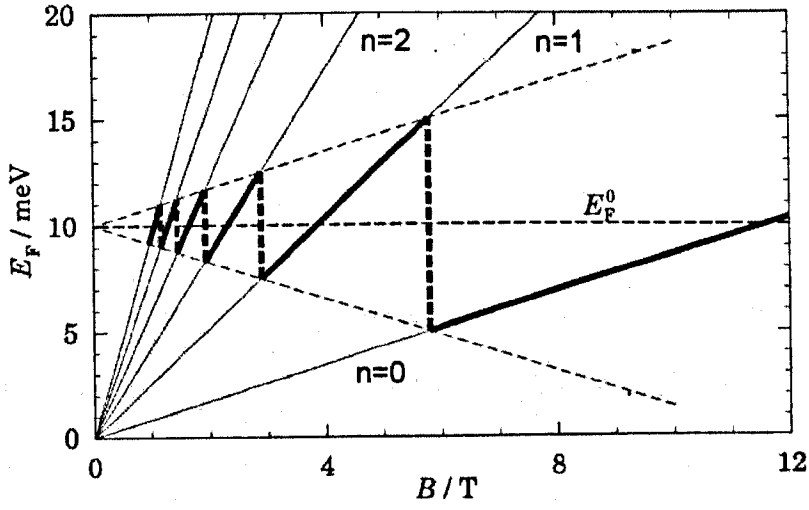

Figure 1-10: The change in Fermi level with magneic field for a 2DEG with $E_0^F = 10meV$ for the zero field case. The thin lines depict the Landau levels the thick line the Fermi energy. Spin splitting is neglected. Taken from [24] with adjustments.

the highest populated electron states as these depopulate in a step-like fashion so does the Fermi energy.

The plateaux in V_{xy} seen in the quantum Hall effect show that in real systems the Fermi energy can lie in-between Landau levels. Therefore, there must be electron states present between Landau levels. In a magnetic field there are said to be extended states, seen in figure 1-9, which run throughout the sample. However, localised states in the tails of the Landau levels exist that do not contribute to conduction. The Fermi energy can then take the values of these localised states. Consequently disorder must be present in a sample to enable the quantum Hall effect to be observed.

Chapter 2

Experimental techniques

2.1 Introduction

The following chapter describes the experimental facilities and the semiconductor samples studied during the course of this research. A brief outline of the magnetic field facilities is given which is followed by a summary of the electrical measurement techniques used. Finally, the composition of the semiconductor heterostructures and processing details are presented.

2.2 Magnetic field facilities

The high magnetic fields used for this research are provided by two different types of magnet. The first type used at Nottingham are superconducting magnets. The second is a resistive water-cooled magnet found at the Service National des Champs Intenses, Grenoble, France.

The superconducting magnets at Nottingham were manufactured by two different companies, Cryogenic Consultants Ltd. (CCL) and Oxford Instruments. The design of the cryostat produced by CCL is shown in figure 2-1. A magnet coil that is superconducting at liquid helium temperatures is immersed in a liquid helium bath located in a superinsulated cryostat. Inside the bore of the magnet a vacuum-insulated insert provides a sample region isolated from the main helium bath. There is a connection

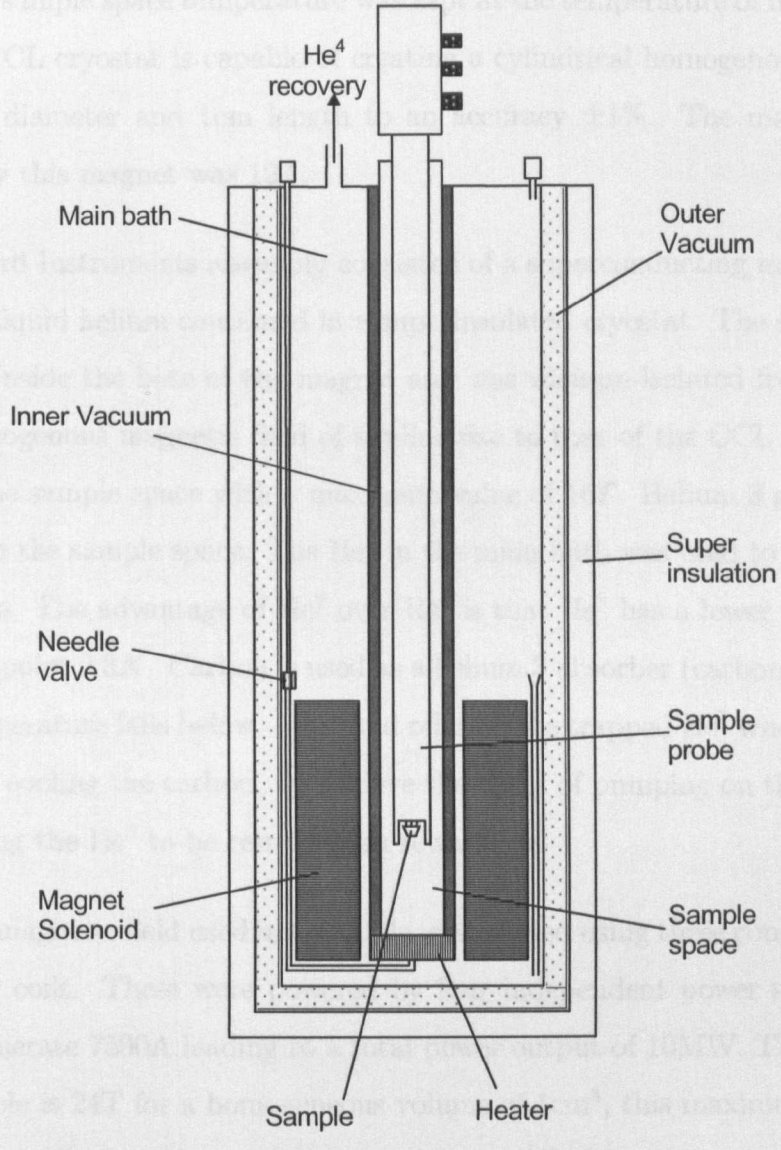

Figure 2-1: A simplified representation of the design of cryostat produced by CCL with the sample probe in-situ. This figure is not to scale.

between the sample space and the main bath via a needle valve through which liquid helium can pass. Varying the amount the needle valve is opened and changing the pumping rate on the sample space, together with a small heater, allows the temperature in the sample space to be varied. During the course of these experiments, however, the sample space temperature was kept at the temperature of liquid helium, $4.2K$. The CCL cryostat is capable of creating a cylindrical homogenous magnetic field of 1cm diameter and 1cm length to an accuracy $\pm 1\%$. The maximum field obtainable by this magnet was $12T$.

The Oxford Instruments assembly consisted of a superconducting magnet placed in a bath of liquid helium contained in a superinsulated cryostat. The sample space was located inside the bore of the magnet and was vacuum-isolated from the main bath. A homogenous magnetic field of similar size to that of the CCL cryostat was possible in the sample space with a maximum value of $16T$. Helium 3 gas ,He^3, was present inside the sample space. The He^4 in the main bath was used to cool the He^3 to liquid form. The advantage of He^3 over He^4 is that He^3 has a lower boiling $3.2K$ and Lambda point $0.3K$. Carbon is used as a helium 3 absorber (carbon absorbs He^3 when its temperature falls below $\backsim$40K and releases the trapped He^3 when reheated). Therefore by cooling the carbon, we achieve the effect of pumping on the liquid He^3 whilst allowing the He^3 to be retrieved on rewarming.

The high magnetic field used in Grenoble was created using three concentric water cooled Bitter coils. These were powered by four independent power supplies each which can generate 7500A leading to a total power output of 10MW. The maximum field obtainable is 24T for a homogeneous volume of $1cm^3$, this maximum, however, does vary depending on the water temperature. All the measurements made at Grenoble were carried out with the sample immersed in He^4 at $4.2K$.

For all the cryostats, the samples were mounted on probes which were inserted into the top of the cryostat. Almost all of the samples measured in this research were mounted upon TO-5 headers. The header could then be plugged into a mounting on the sample probe. Co-axial cables connected the sample mount along the length of

the thin walled cylinder of the probes length and into the BNC ports of the probe head box.

2.3 Measurements

2.3.1 Temperature measurements.

The temperature of the samples was determined depending on sample probe and cryostat. Cryogenic liquids were used to cool the samples. The temperature of the sample being studied was determined from the temperature of the liquid into which it was immersed. The temperature for all experiments was constant throughout. Exact temperature dependence measurements were not taken during this research. We believe an accuracy of $\pm 0.1K$ for the Grenoble and CCL cryostats, and $\pm 0.025K$ for the Oxford Instruments cryostat was achieved. Typically the temperature of the sample was found by measuring a precalibrated rhodium iron thermistor mounted on the sample probe above the sample with a Hewlett Packard $HP3457A$ DMM. The thermistor's resistance was measured using the four wire technique to discount contact and cable resistance. To ensure that the sample was cooled to the correct temperature a delay in the measurement start time of thirty minutes from the point the thermometer reached at $4.2K$was used. This ensured that the sample and apparatus were thermally settled at $4.2K$.

2.3.2 Angular measurements

The measurements in chapter 3 required that the angle of the sample be changed with respect to the magnetic field, which is fixed to a vertical orientation. A sample probe which had a rotating sample mount was used. The sample was rotated about an axis perpendicular to the growth plane. The current in the QW samples in chapter 3, flowed in the direction of the sample growth. Therefore, the sample could be rotated from an orientation where the magnetic field was parallel to the current direction to one where the current was perpendicular to the magnetic field.

The micrometer on the sample probe head was calibrated visually. The sample was mounted horizontally at first, the reading on the gauge taken. The sample was then turned through 90 degrees to a visually vertical alignment and the micrometer read again. The corresponding change in the micrometer gauge for 90 degrees was thus found and calculations of the sample angle were determined from this. During the course of a set of angle measurements, the turning of the sample was always kept unidirectional to avoid backlash. We estimate the error in the angle to be approximately 10% or $\pm 1^0$.

2.3.3 Electrical measurements

The two systems measured in this thesis require different measurement techniques. The electrical measurements of the tunnelling devices discussed in chapter 3 are described first, followed by the electrical measurements used in the quantum Hall effect experiments.

Tunneling measurements

The measurements in Grenoble were made using a Keithley 4300 source meter. The meter supplies a voltage to the sample and the current passing through the sample is measured. The accuracy of the source meter depended on the current limit set. When the current limit is set at 1mA the device is capable of measuring $\sim 10^{-9}A$. Considering the level of the noise within the experiment we believe we were measuring to an accuracy of $\sim 10^{-8}A$, for the 1mA current limit, and $\backsim 10^{-7}A$ for a current limit of 10mA. A C++ program written by D.K. Maude was used to collect the data.

The measurements made in Nottingham used a different technique. The tunnel current of the resonant tunneling diodes is measured whilst sweeping the voltage. The experimental circuit is shown in figure 2-2. The voltage is chosen as the controlled variable whilst we measure the current, via the voltage across the load resister. Such a technique is used because the voltage is normally single valued whereas the current around the resonant peak is sometimes double valued. The value of the load resistor

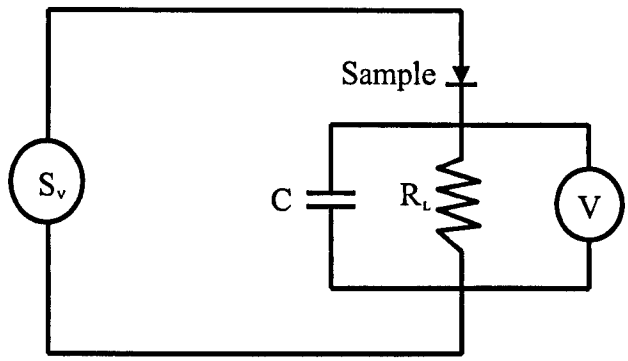

Figure 2-2: The circuit used in measuring the current through a QW heterostructure by sweeping the voltage with source S_v and measuring the voltage V on the precision load resistor R

was typically chosen to be of the order of 10% of that of the sample resistance in the region of interest. Choosing the load resistor value as described ensured that any features in the current voltage curve would be observable in the range of interest. For the sample in chapter 3 the load resistor was $70k\Omega$, giving a current resolution of $\sim 10^{-7}A$. The capacitor placed in parallel to the load resistor in figure 2-2 had a value of $1\mu F$. The actual choice of capacitor size is a compromise. A smaller capacitor may not be able to reduce large noise, hence providing no improvement in accuracy. A larger capacitor may well mask smaller features in the system due to a larger time constant. A Keithley 230 was used to provide the voltage and was swept remotely. A Hewlett Packard 3457A DMM measured the voltage across the load resistor. Coaxial cables were used throughout. A Labview program produced by O. Makarovsky was used to collect the data. Some features of the program that aided accuracy were: a delay between measurements, this ensured each data point was collected and read by the various instruments and computer; a variable averaging procedure of the load resistors voltage for each value of source voltage. Typically four measurements were made for each value of source voltage, the first point was discarded as a possible transient value and the next three averaged. A rough rule for the time taken per sweep was that each measurement taken took approximately one second; consequently, for each value of source voltage set, one averaged point took 4 seconds.

Quantum Hall effect measurements

The QHE group of measurements were all performed using the standard four wire technique. The current was supplied using a Keithley 220 along the length of the sample. Hewlett Packard HP3457A digital multimeters were used for the voltage measurements between contacts positioned along the sample length. The resolution of the measurements was around 6 digits, corresponding to a level of noise less than 10^{-6}V. The integration time of the multimeters was set to 1 second allowing the multimeter to average out around 50 data points. Therefore a low level of noise was observed. An adaptation of the program engineered by O. Makorvsky mentioned previously for the tunneling measurements conducted the remote measurements.

For the purpose of experimental observation of the QHE we believe the following conditions ensure the best results. A mobility greater than $5 \times 10^4 cm^2 V^{-1} s^{-1}$ is a requirement for observation of large regions where $V_{xx} = 0$. Low temperatures $T \leqslant 4.2K$ to ensure the system remains in the quantum limit. Finally high magnetic fields, to obtain reasonable resolution in the magnetic field along the plateau region are needed. It was found that filling factors $\nu = 1$ to 4 were most suitable for this. To ensure reproducibility in measurements of the QHBD a second set of conditions become relevant.

The QHBD is dependant on parameters such as current, sweep rate, sample width, time, length, magnetic field and magnetic field sweep direction. Therefore, recognising the various factors in QHBD is essential in understanding its nature. To ensure that the measurements were as accurate as possible the following points needed consideration for each sample. The contacts should close to the ideal case i.e. ohmic and low resistance. An ideal contact equilibrates the incoming electrons with the outgoing electrons. Some models predict some time dependence or switching between states Komiyama and Kawaguchi [16],Cage et al. [29]. These may be very fast and can only be seen as telegraph noise on a large time frame or conversely they may be slow in formation and need time to fully develop. From either perspective the sweep rates of both the magnetic field and current should be set slow enough so that

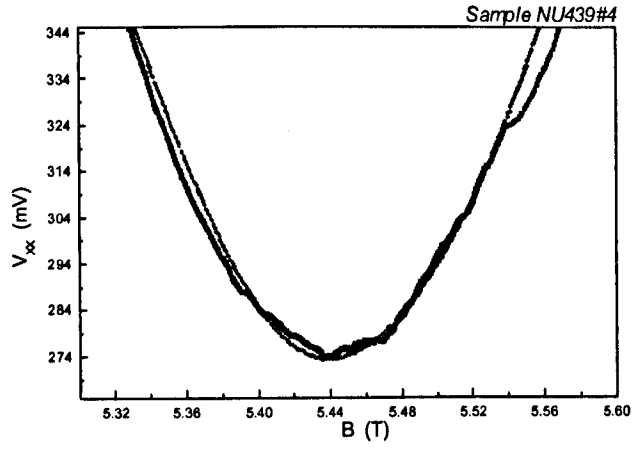

Figure 2-3: The voltage versus magnetic field dependence of a standard Hall bar sample made from wafer NU439. The current I=200mu A and T=4.65K. The smoother grey curve was measured with a magnetic field sweep rate of 0.1T/min. The curve showing slight features was measured using a sweeprate of 0.01T/min.

any time dependence can be seen in the current or field sweeps. Figure 2-3 gives an example of how the magnetic field sweep rate can smooth the QHBD curves. Finally in order to obtain some of the phenomena associated with QHBD, the breakdown parameters, like the current and magnetic field need to be chosen very specifically. The range of interest may be as little as 1% of the parameter being measured as seen for sample P in chapter 5.

When studying QHBD there are two main parameters on which the QHBD depends; these are the current and magnetic field. At a certain critical current I_c, the previously dissipationless longitudinal resistance R_{xx}, has a sudden onset of dissipation, observed as an increase in V_{xx} from around $10^{-6}V$, the rough limit of our measurement techniques, to approximately $10^{-3}V$. Part of the problem in studying the QHBD has been in defining a standard technique for defining QHBD. Within the dissipationless region, breakdown occurs at different critical currents I_c, depending on the magnetic field at which measurements are being taken. At present there is no precisely defined breakdown criterion, therefore to some extent the onset of breakdown is a matter of the judgement of an experimentalist. Some authors choose the

breakdown point to be when the previously dissipationless region shows a dissipation of a specified value. Other authors determine the point of breakdown to be the current at which a sudden sharp jump out of the dissipationless region is observed. Finally we consider the magnetic field dependence of I_c. The lower filling factors of a sample tend to have higher breakdown currents than the higher filling factors i.e. $I_{c,\nu=4} < I_{c,\nu=2}$. This exposes a problem when comparing and contrasting results obtained by different research groups.

Let us now consider the two most common methods for studying the QHBD which are based on the parameters of the current and magnetic field. One method is to take measurements at a fixed magnetic field, sweeping the current. The other measurement technique is to keep the current constant and sweep the magnetic field. For the fixed magnetic field method, different fields are chosen within the plateau region. For each field the current is swept upwards, initially there is no dissipation measured until the current reaches I_c where a sudden sharp step in the voltage measured will be observed. Large errors can arise in determining I_c using this method when the increase in voltage is slowly varying with current or the presence of multiple steps. The second method is to sweep the magnetic field through the plateau region whilst applying a constant current to the sample. After each sweep the current can be altered allowing the entire plateau region to be studied for different currents. By increasing the current applied to the sample carefully, a point can be reached where the previously dissipationless region just starts to show dissipation for all magnetic fields close to the filling factor. The value for the critical current obtained using the second method is less subjective than that of the first method and ensures the minimum value for I_c is found.

2.4 Composition and properties of the samples

All the samples measured in this work are GaAs/AlGaAs samples grown by molecular beam epitaxy (MBE). The following is a simplified description of MBE discussed by Davies [24]. A substrate of GaAs is placed on a heated holder in ultra high vacuum

$\backsim$ $5x10^{-11}$mbar. The required elements for the materials needed for building the structure of the sample are heated in furnaces with openings directed towards the substrate. Such furnaces are called Knudsen cells. The openings are controlled by computer operated shutters. The pressure in the chamber is low enough that the mean free path of the molecules is much greater than the width of the chamber. The molecules entering the chamber from the Knudsen cells do not diffuse as they normally would in a gas but emerge as a beam directed at the substrate. This is known as the Knudsen regime of molecular flow through gases. Growth commences once the shutters are opened and the flux of atoms is controlled by the temperature of the furnaces. The growth rate is controlled by the flux of the group III element. The atoms are mobile on the substrate surface, and settle to form the crystal. In the simplest picture the growth rate is layer by layer. Donors and acceptors can be introduced by additional Knudsen cells, for example Si and Be respectively.

As MBE takes place in ultra high vacuum it is possible to use reflected high energy electron diffraction RHEED to monitor the growth of the sample. A beam of electrons is directed so that it just grazes the sample surface, the resulting diffraction pattern is viewed via a fluorescent screen. The growth of a single monolayer of molecules can be seen by a periodic change in the intensity and pattern of the diffraction. Consequently, the growth can be counted precisely in terms of monolayers, and the structure of the surface can be determined from the pattern of the diffraction. One of the advantages of MBE growth is that highly abrupt interfaces can be manufactured.

MBE does require care and the following points highlight the common problems that need to be avoided. To ensure high quality samples, extremely pure starting materials are needed. Reaching and maintaining UHV is often problematic as well. The cell's temperature needs close monitoring to ensure a constant flux, the sample is rotated to minimise the effect of any small changes in the flux of molecular beams. The substrate temperature can affect the quality of the structure. If the temperature is too high unwanted diffusion can occur and blur the interfaces. A temperature that is too low means that defects will not have time to be removed by annealing.

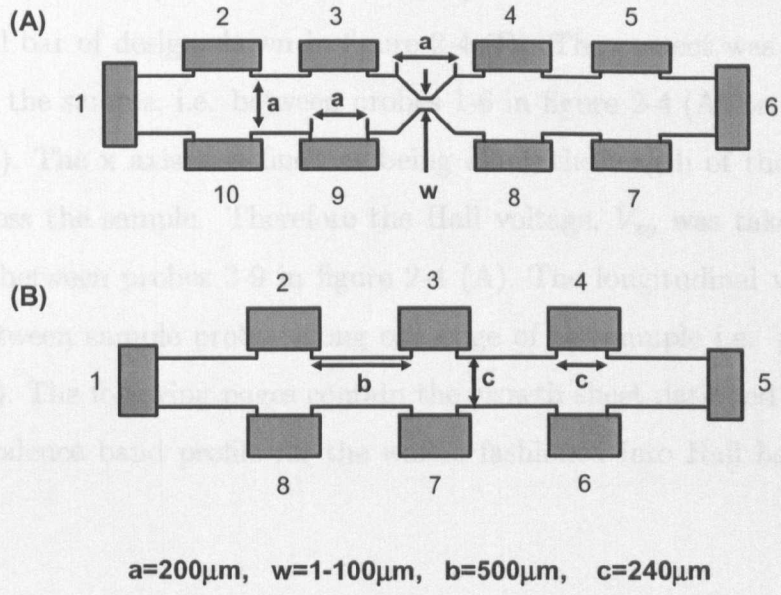

Figure 2-4: Sample schematics for the QHE samples. (A) is the constriction sample design. (B) is the hole gas standard Hall bar sample design

The samples studied in this thesis are all grown by MBE at Nottingham by Dr M. Henini. The two dimensional electron gas quantum Hall effect samples had low temperature mobilities (4K) of between $13.4 - 70m^2V^{-1}s^{-1}$. The tunneling samples measured had I(V) peak to valley ratios for the 1st quantum well resonance of up to 21 indicating that the samples were of high quality and matched those of previous work [30]. The samples were processed by photolithography in Nottingham by Mr J. Chauhan and Mr D. Taylor, in Sheffield by Dr G. Hill and in Glasgow by Dr A. Neuman. The contacts for the all samples were formed using the standard techniques of evaporating a mixture of gold and tin onto the sample and heating the sample so that the metal mixture diffused into the sample to form metal contacts.

2.4.1 Quantum Hall Effect Samples

The electrical characteristics of QHBD, were studied for a variety of samples. The following wafers and sample composition correspond to the samples whose properties are in chapter 5. Wafers NU1624, NU439 were fabricated into Hall bars with constrictions as seen in figure 2-4 (A). The constriction widths ranged from 1-100μm,

with a length of 2 or $10\mu m$ for the narrowest part. NU1156 was fabricated into a standard Hall bar of design shown in figure 2-4 (B). The current was passed along the length of the sample, i.e. between probes 1-6 in figure 2-4 (A) or probes 1-5 in figure 2-4 (B). The x axis is defined as being along the length of the sample, the y axis is across the sample. Therefore the Hall voltage, V_{xy} was taken across the sample, i.e. between probes 3-9 in figure 2-4 (A). The longitudinal voltage V_{xx} is measured between sample probes along one edge of the sample i.e. probes 2-4 in figure 2-4 (B). The following pages contain the growth sheet data and the expected conduction/valence band profile for the wafers fashioned into Hall bars of various designs.

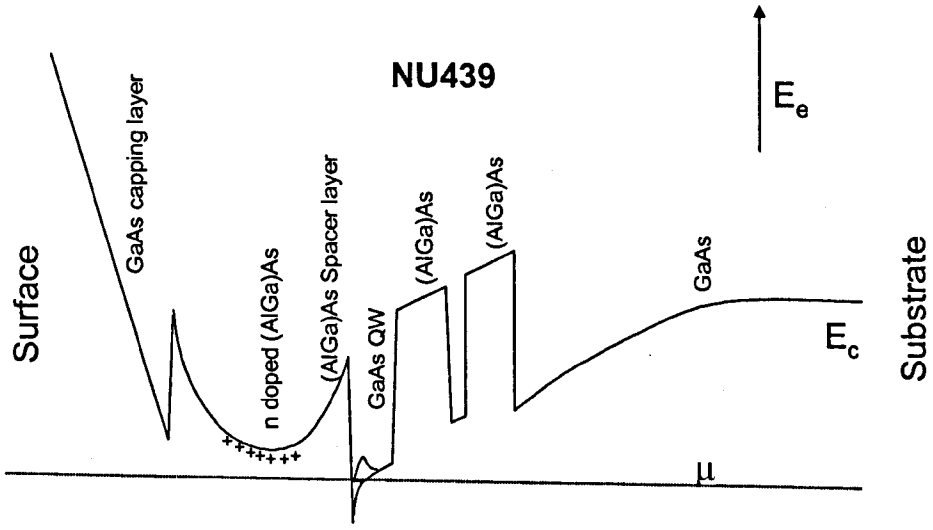

Figure 2-5: The expected conduction band profile for wafer NU439 is shown. The chemical potential is labelled μ.

NU439		
Thickness	Doping	Material
254.4Å		GaAs
305.3Å	$1\times10^{18}n$	$Al_{0.33}Ga_{0.67}As$
63.6Å		$Al_{0.33}Ga_{0.67}As$
101.8Å		GaAs
101.8Å		$Al_{0.33}Ga_{0.67}As$
33.9Å		GaAs
101.8Å		$Al_{0.33}Ga_{0.67}As$
$1.02\mu m$		GaAs
$0.81\mu m$		GaAs
$0.2\mu m$		GaAs
		Si Substrate

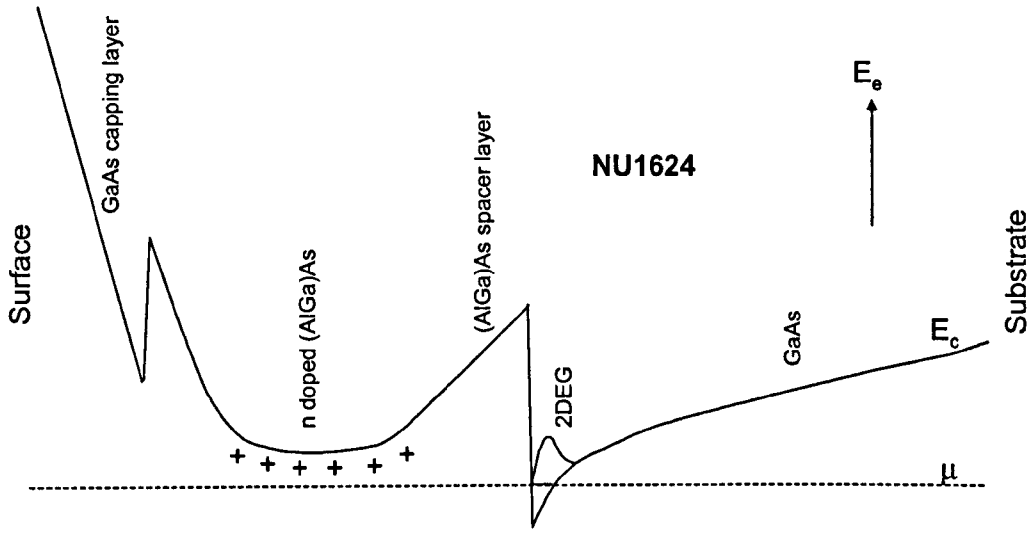

Figure 2-6: The expected conduction band profile for wafer NU1624 is shown. The chemical potential is labelled μ.

NU1624		
Thickness	Doping	Material
168Å		GaAs
391Å	$1.3\times10^{18}n$	$Al_{0.33}Ga_{0.66}As$
202Å		$Al_{0.33}Ga_{0.66}As$
$1\mu m$		GaAs
$0.8\mu m$		GaAs
$0.2\mu m$		GaAs
		Si substrate

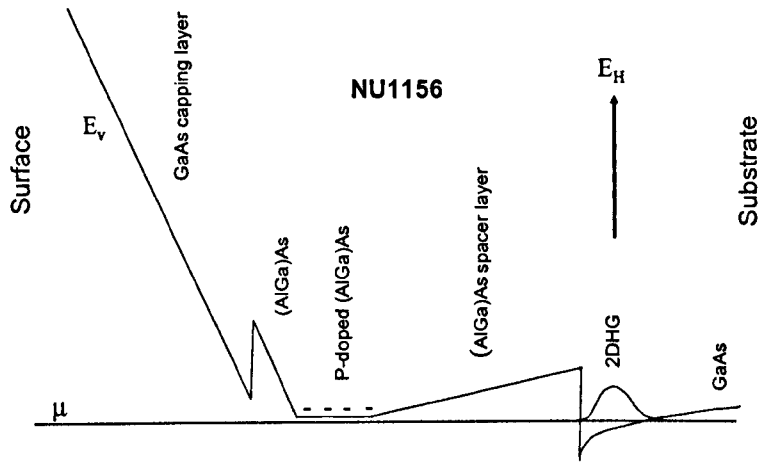

Figure 2-7: The expected valence band profile for wafer NU1156 is shown. Note, the hole energy increases towards the top of the page. The chemical potential is labelled μ.

NU1156		
Thickness	Doping	Material
$0.1\mu m$		GaAs
$0.11\mu m$		GaAs
101.8Å		GaAs
407.0Å		$Al_{0.33}Ga_{0.67}As$
801.3Å	$5\times10^{17}p$	$Al_{0.33}Ga_{0.67}As$
$0.2\mu m$		$Al_{0.33}Ga_{0.67}As$
$0.3\mu m$		GaAs
25.4Å		$Al_{0.33}Ga_{0.67}As$
25.4Å		GaAs
$0.51\mu m$		GaAs
$0.31\mu m$		GaAs
$0.2\mu m$		GaAs
		(311) Si substrate

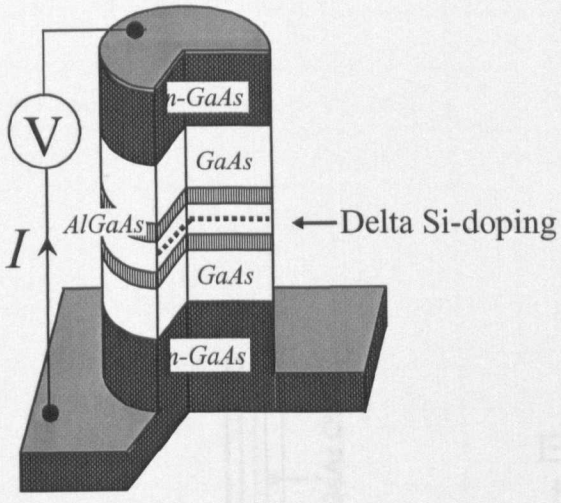

Figure 2-8: The cross section of a mesa fabricated from wafer NU674 is shown. The sample probes connect with the substrate and the mesa cap as shown.

2.4.2 Tunneling samples

The tunneling samples were fabricated from wafer NU674 whose growth sheet and expected conduction band profile can be seen on the following pages. Circular mesas were etched onto the wafer using photolithography. Different diameter mesas were etched. The mesa diameters chosen ranged 20 to 100μm. A typical profile of a mesa can be seen in figure 2-8. The sample probes were contacted to the mesa cap and the substrate, shown in figure 2-8. The convention in this thesis is to label positive bias when the substrate is the ground and the cap is positive.

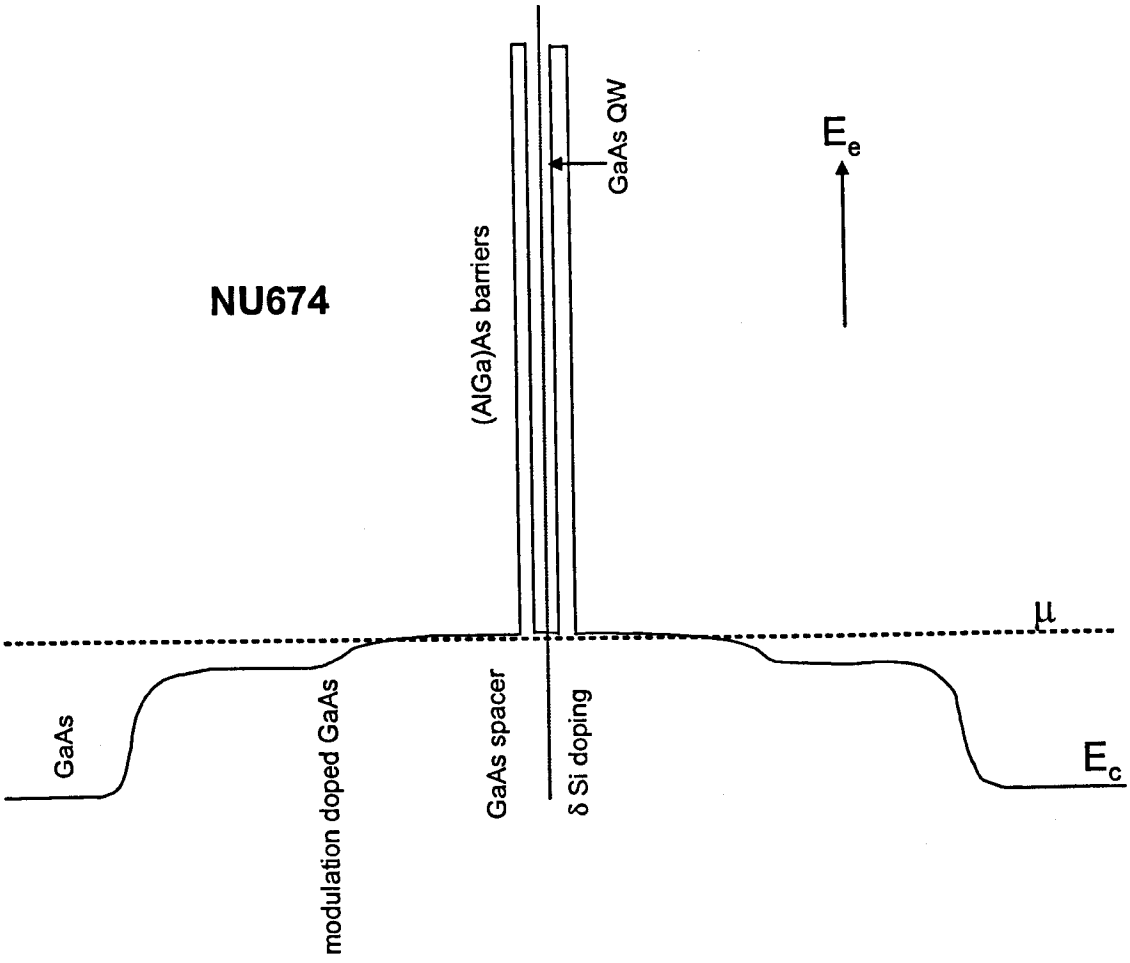

Figure 2-9: The expected conduction band profile for wafer NU674 at zero bias is shown. The chemical potential is labelled μ.

The layer composition of NU674

NU674		
Thickness	Doping	Material
$0.6\mu m$		GaAs
805.6Å	2×10^{16}	GaAs
508.8Å	2×10^{17}	GaAs
203.5Å		GaAs
56.5Å		$Al_{0.40}Ga_{0.60}As$
45.2Å		GaAs
0.00Å	$\delta = 4 \times 10^{9}$	Si
45.2Å		GaAs
56.5Å		$Al_{0.40}Ga_{0.60}As$
203.5Å		GaAs
508.8Å	2×10^{16}	GaAs
805.6Å	2×10^{17}	GaAs
$2.0\mu m$		GaAs
		n^+ substrate

Chapter 3

A study of magneto-compression of a Si-donor state using magneto-tunneling spectroscopy

3.1 Introduction

This chapter examines a further development of the magneto-tunnelling spectroscopy (MTS) technique, aimed at probing how a magnetic field modifies the spatial form of the wave functions of quantum systems. The tunnel current through Si-donor states in a quantum well (QW), in the presence of a strong magnetic field, applied at various angles to the QW plane, is studied. The component of magnetic field parallel to the current direction, $B_{||}$, provides a means of compressing the donor wave function in real space. The perpendicular component $B_{\perp}$ is used to adjust the transverse momentum k of the tunneling electrons and thereby map out the momentum-space probability density $|\varphi(k)|^2$ of the donor ground state at different degrees of magneto-compression.

The experiments and analysis are relevant to recent experiments in which MTS has been used to map out the spatial form of the probability densities of electrons bound to the ground and excited states of self assembled InAs quantum dots [8], [13],

[31], [32], [33], [34], Landau levels [35] and hole dispersion [36]. The hydrogenic states of a donor in a QW provide a useful means of validating the MTS technique since their properties have received considerable experimental and theoretical attention [10], [1], [38], [39], [40], [37] and the confining potential is much better defined than the case of quantum dots. Also, the donor states are more extended than those of quantum dots so that the wavefunctions are much easier to compress by the action of a magnetic field applied perpendicular to the plane of the QW.

The chapter starts by looking at tunneling in GaAs/(AlGa)As heterostructures, starting with the simple case of a potential barrier to illustrate the main features of quantum tunneling. Next, a transfer Hamiltonian method is presented to describe resonant tunneling through a QW, followed by an overview of how the transfer Hamiltonian method can be applied to a real system. We then re-examine the MTS experiment using Si-donors in GaAs for the particular case when the magnetic field is applied perpendicular to the tunnel current, first measured by Sakai et al. [1], [41]. To analyse the data we use a somewhat different model compared to that of Sakai et al., and determine a slightly different result for the extent of the donor state wavefunction. The model used to describe MTS in tilted magnetic fields is outlined in section 3.5 followed by the experimental results for the tilted field measurements. The results in section 3.6 show that the proposed model qualitatively describes the magneto-compression of the donor states, and confirm that the component of magnetic field parallel to the current does indeed significantly compress the donor wavefunction. It is shown that a very good quantitative agreement between the experimental data and the model is obtained if a tunneling distance of 13.5nm is used as a fitting parameter. The value of this parameter is discussed in terms of the sample composition and the physical conditions under which the experiments were performed.

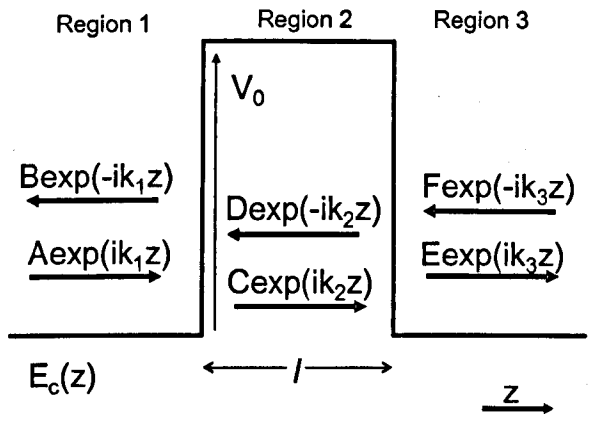

Figure 3-1: The conduction band profile for a barrier of (AlGa)As width l and height V_0 placed in GaAs with the wavefunctions for each region shown.

3.2 Tunneling -an introduction

In chapter one, it was shown that a heterostructure of a thin layer of (AlGa)As embedded in GaAs provides a potential barrier for a incident electron. Figure 3-1 shows such a system. The barrier width is denoted by l and E_c is the conduction band edge. The potential step height is V_0 and the electron energy is E_{el}. Classically, when an electron of energy E_{el}, arrives at a barrier of potential step height V_0, it will be reflected if $E_{el} < V_0$ and be totally transmitted if $E_{el} > V_0$.

However, in the quantum treatment of the problem this is not the case. There is a small probability that an electron incident upon a barrier with energy less than that of the barrier layer may tunnel through the barrier. Consider the problem outlined in figure 3-1. A wave function can be constructed for each of the three regions, region one, $z < -l/2$, two $-l/2 < z < l/2$, three $z > l/2$ with the origin located in the central plane of the QW (see equation 3.1):

$$\Psi = \begin{cases} [A\exp(ik_1 z) + B\exp(-ik_1 z)], & \text{region 1} \\ [C\exp(ik_2 z) + D\exp(-ik_2 z)], & \text{region 2} \\ [E\exp(ik_3 z) + F\exp(-ik_3 z)], & \text{region 3.} \end{cases} \tag{3.1}$$

In equation 3.1, the different values of wave number k correspond to the different

regions. For example k_1 is related to region one and so forth. By considering the transmission of an electron from region 1 to region 3 and describing the resulting wavefunction as the original wavefunction acted on by some transfer function, it is possible to work out the transmission coefficient for the simple system outlined here. One method of solving this problem is to use a transfer matrix technique [24]. The transfer matrix technique uses the wavefunction of a small section of the system to calculate the wavefunction of an adjoining section by using a matrix transformation. Each boundary dividing different regions is considered separately i.e. the interface between regions 1 and two is considered separately from the interface between regions 2 and 3. The method is sequential, first the region 1 to region 2 transfer is evaluated, second the region 2 to region 3 transfer. The condition that both the wave function Ψ and $(1/m)\partial\Psi/\partial x$ [24] must be continuous over each boundary is chosen. For an electron tunneling from region one to region three we set A=1, B=r*, E=t*, F=0, where r* and t* are reflection and transmission amplitude coefficients. Also of note is that the wave numbers are related to the energy of the incoming electrons. Consequently, as the potential of the system is the same on either side of the barrier (considering the zero bias case) the wave numbers of the first and last region are identical i.e. $k_1 = k_3$. Using these conditions, it is possible to derive an expression for the transfer coefficient of a single barrier if $E_{el} < V_0$ as

$$T = \left[1 + \frac{V_0^2}{4E_{el}(V_0 - E_{el})} \sinh^2 k_2' l\right], \tag{3.2}$$

where $k_2' = [2m(V_0 - E_{el})/\hbar^2]^{1/2}$ is complex when $E_{el} < V_0$. For the case where $E_{el} > V_0$ we obtain the following expression

$$T = \left[1 + \frac{V_0^2}{4E_{el}(E_{el} - V_0)} \sin^2 k_2 l\right], \tag{3.3}$$

with $k_2 = [2m(E_{el} - V_0)/\hbar^2]^{1/2}$ taking real values [24]. In figure 3-2, the transmission probability for a single barrier is shown. Note that some tunneling occurs when $E_{el} < V_0$. Also, it is evident that the transmission probability does not become unity for all values of $E_{el} > V_0$. The peaks in the transmission probability correspond to

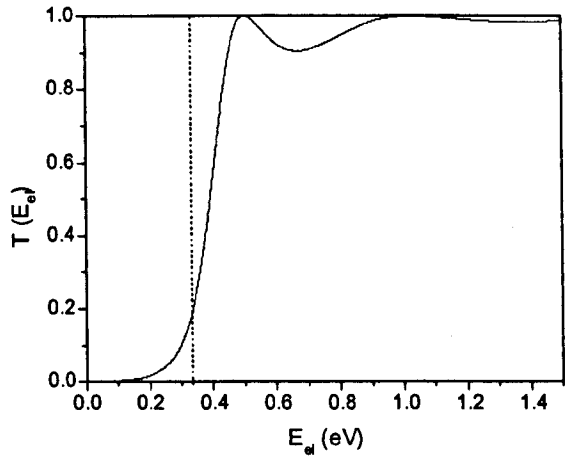

Figure 3-2: The transmission probability $T(E_{el})$ for an (AlGa)As barrier, 5.7nm wide, placed in GaAs is plotted against the electron energy E_{el}(eV). The barrier height V_0 =0.33eV is depicted by the dotted line which corresponds to the classical transmission.

the case when $\sin k_2 l = 0$ and a whole number of half wavelengths are accommodated in the barrier.

3.3 The transfer Hamiltonian method

The tunneling matrix method briefly outlined in the previous section can be applied to describe the double barrier system of a resonant tunneling diode (RTD). The transfer matrix method, though analytically simple, can become difficult to use as the systems considered become more complicated. Instead, a transfer Hamiltonian description of resonant tunneling will be considered. This method is relatively simple to use and gives the correct magnitude for the resonant tunnel current in the case of a simple double barrier system. The transfer Hamiltonian description of tunneling was first proposed by Bardeen [42], applied to double barrier systems by Payne [45] and is a sequential method as follows

$$e_{emitter} + D^{+}_{QW} \rightarrow D^{0}_{QW} \rightarrow D^{+}_{QW} + e_{collector}, \tag{3.4}$$

where e corresponds to an electron and D the donor state.

Firstly, the one-dimensional case is considered. The method requires, as with the tunneling matrix method, that the system be broken down into smaller subsections of the total system. For the case of the double barrier system, these subsections are the emitter (E), the quantum well (w) and the collector (c). These three subsections relate to the quantum well as shown in figure 3-4. Each subsection is described by a separate and individual Hamiltonian H_E, H_w, H_c, respectively. The eigenstates of the different subsystems Ψ_E, Ψ_w, Ψ_c, and their energies E_E, E_w and E_c are described by

$$H_E\Psi_E = E_E\Psi_E, \tag{3.5}$$

$$H_w\Psi_w = E_w\Psi_w, \tag{3.6}$$

$$H_c\Psi_c = E_c\Psi_c. \tag{3.7}$$

As the states overlap, there is a small probability that an electron in one of the subsystems could tunnel into another subsystem. The rate of probability transfer W, from a initial state Ψ_i to a final state Ψ_f is given by Fermi's Golden Rule

$$W_{if} = \frac{2\pi}{\hbar}|T_{fi}|^2\delta(\varepsilon_f - \varepsilon_i), \tag{3.8}$$

where T_{fi} is the Bardeen transfer matrix element giving the interaction between the initial state i and the final state f. It can be written [42]

$$T_{if} = (\frac{\hbar^2}{2m})\int_S(\Psi_i\nabla\Psi_f^* - \Psi_f^*\nabla\Psi_i)\cdot dS, \tag{3.9}$$

where the integral is taken over any surface in the barrier common to both subsystems. The term $\delta(\varepsilon_f - \varepsilon_i)$ in equation 3.8 gives the conservation of energy condition. To take account of level broadening due to scattering processes in the contacts, the delta function is replaced by a line shape function $A(\varepsilon_f - \varepsilon_i)$,which has a finite width $\hbar/\tau$, where τ is a characteristic scattering time.

The application of the transfer Hamiltonian description of resonant tunneling to the double barrier system is straight-forward. The electron is said to tunnel from the emitter to the quantum well state. Then the electron tunnels from the quantum well state into the collector. This is a sequential process [43], [44]. The electrons can also tunnel straight from the emitter to the collector giving rise to a non-resonant current. The current density $j(f,i)$ between the initial and final state at resonance can be written as

$$j(f,i) = W_{if} n_r = \left(\frac{2\pi}{\hbar}\right) |T_{if}|^2 \rho_i(\varepsilon_r)(f_i(\varepsilon_r) - f_r), \tag{3.10}$$

where n_r is the density of states in energy of electrons available at the resonance energy ε_r. This in turn is given by $\rho_i(\varepsilon_r)$, the density of eigenstates in energy at the resonant energy in the initial state, multiplied by $(f_i(\varepsilon_r) - f_r)$, the occupancy of the transfer states. $f_i(\varepsilon_r)$ is the Fermi function for the initial state at the resonance energy and f_r the occupancy of the final state.

Applying 3.10 to the specific case of the symmetric double barrier, in the steady state regime, the occupancy of the resonant level will adjust until the currents flowing in and out of the level are equal. Therefore, sufficient time has elapsed so that the current $j(E \rightarrow w)$ is the equivalent to the current $j(w \rightarrow c)$, where E signifies the emitter states, w applies to the well states and c corresponds to the collector states. Payne [45] found the wave functions for each of the three subsystems of the double barrier and then applied the above transfer Hamiltonian process to them. He found that the transfer matrix was the same for both the tunneling into and out of the quantum well, due to the symmetry of the problem. Also, due to the fact that the energies of the states in all three subsystems are equal, the in-plane momentum values k are identical for all subsystems if scattering is neglected. Thus

$$j(E \rightarrow w) = j_0(f_E(\varepsilon_r) - f_r), \tag{3.11}$$

$$j(w \rightarrow c) = j_0(f_r - f_c(\varepsilon_r)), \tag{3.12}$$

where $j_0 = (2\pi/\hbar)|T_{E\to w}|^2\rho_E(\varepsilon_r)$. Applying the steady state condition and the further condition that at bias $f_E(\varepsilon_r) \to 1$ and $f_c(\varepsilon_r) \to 0$, then

$$j_{res} = j_0/2. \tag{3.13}$$

This is equivalent to assigning an occupancy $f_r = 1/2$ to the resonant state in the well. The transfer Hamiltonian method thus provides a simple means of calculating the magnitude of the resonant current. Payne shows that the transfer Hamiltonian is able to describe resonant tunneling as the incident electron energy range is much larger than the energy range of the resonant peak of the transmission coefficient. Furthermore previous magneto tunneling studies and experiments have found it to be a valid method for modelling the resonant current [46], [8], [1], [12].

3.3.1 Applying the transfer Hamilton method

The tunneling Hamiltonian method described above can be summarised for a double barrier system as follows. For each subsystem E,w,c, the corresponding Hamiltonian is determined and the wavefunction can be found. Using the Bardeen transfer matrix equation 3.9 and equation 3.13, we can calculate the resonant current. The method outlined is for the 1-dimensional case where, by considering the overlap of adjacent eigenfunctions, Fermi's Golden Rule is applied to determine the resonant current.

To expand the model to the three-dimensional case, we define the plane of the QW to contain the xy plane, the z direction is parallel to the tunnel current and perpendicular to the QW plane (see figure 3-4). For the case of a QW, there is no confinement in the xy plane or in the xy emitter plane. In the z direction, however, the QW confines any electrons within it. The Hamiltonians are separable, the wavefunctions for each subsystem can be written as $\Psi(x,y)\chi(z)$. Note, a key assumption in our model is that the donor state Hamiltonian is separable. We are able to separate the donor state Hamiltonian as we assume it has the form of a simple harmonic oscillator. The donor state confining potential is considered hydrogen-like

and not parabolic. However, the good fit to the data confirms that the parabolic potential assumption is reasonable. From equations 3.11 and 3.13, it can be seen that $I \propto |M_{if}|^2$, which means the current is proportional to the modulus squared of the overlap between the wavefunctions. Because of the separability, it is possible to write

$$I \propto |MT|^2, \tag{3.14}$$

where T is the Bardeen transfer matrix element for the z direction overlap, given in equation 3.9, and M is the transverse overlap integral of the xy plane, given by

$$M = \int\int \Psi^{D*}(x,y)\Psi^{E}(x,y)dxdy, \tag{3.15}$$

where $\Psi^D(x,y)$ is the wavefunction of a confined state in the QW and $\Psi^E(x,y)$ the emitter state wavefunction. As this research focuses on Si-donors lying in the central plane of the QW, $\Psi^D(x,y)$ will from now on refer to the wavefunction of a Si-donor state lying in the central plane of a QW. The separation of the variables is vital to the MTS technique. We can envisage this as follows, the wavefunction is the product of several different wavefunctions, such an idea is analogous to that used in standard Fourier analysis. The emitter states are plane waves in the x, y direction and have the form of the Fang-Howard wavefunction in the z direction. For the donor states we construct a Gaussian wavefunction in the x, y plane and assume a Gaussian shape, for the lowest state of a simple harmonic oscillator, in the z direction. We choose the condition that parts of the wavefunction dependent on z, are unaffected by the applied magnetic field and are considered separately. We believe a magnetic field perpendicular to the z-axis, has little effect on the Bardeen transfer matrix T. Patane et al. [8] showed that the effect of the perpendicular magnetic field could be shown to have the effect of slightly increasing the barrier height. We neglect this effect and the Bardeen transfer matrix is thus considered unaffected by the applied magnetic fields and remains constant. Thus, for the zero magnetic field case of a QW, the resonant current is equal to a constant related to the overlap integrals of

the wavefunctions $\Psi^E(x,y)\chi^E(z)$ and $\Psi^D(x,y)\chi^D(z)$.

The incorporation of donor states in the central plane of the QW provides confinement in the xy plane of the QW. Electrons will be only able to tunnel from states in the emitter with the same wavenumber k as those in the empty donor states (conservation of momentum). Equation 3.14 can be written

$$I \propto |M|^2 \tag{3.16}$$

and is dependent on the xy parts of the wavefunctions. The emitter states are unconfined plane waves in the xy plane; the donor states are strongly confined in real space and therefore have an extended wavefunction in k space. A graphical representation of the overlap of the emitter and donor state wavefunctions due to a magnetic field is shown in figure 3-3. We calculate the donor state as having a width in k space, $k_D = \pi/l = 3.14 \times 10^8 m^{-1}$, where l is the real space extent of the donor state, and the plane wave emitter states have $k_f = (2\pi n_{2D})^{1/2} = 7.9 \times 10^7 m^{-1}$. The width of the emitter states remains constant with changing magnetic field. Therefore, any variation in the overlap integral is due to variation in the donor state wavefunction with Δk, see figure 3-3. At low temperatures we take the emitter state electrons to have momentum $\pm k_f$ with an average of $k = 0$. The Fourier transform of the donor wavefunction has a maximum at $k = 0$ and we envisage tunneling from the emitter state, to the peak of the donor state, to be a ballistic process, i.e. no scattering occurs and k is conserved. The density of ionised impurities is very low in the barrier, $< 10^{15} cm^{-3}$, indicating that scattering is unlikely [8]. As expected classically by the Lorentz force, a magnetic field applied perpendicular to the tunneling electrons will alter their momentum $\Delta k_y = eB_\perp \Delta s/\hbar$, where Δs is the tunneling distance and $B_\perp$ is the magnetic field applied in the x direction. The change in the momentum means that the electrons now tunnel into states with wavevector Δk_y. The wavefunction overlap at a point Δk_y, from the peak in the donor state wavefunction in k-space, will be different from the zero field value and according to equation 3.16, the current should change. Due to the assumption that the emitter

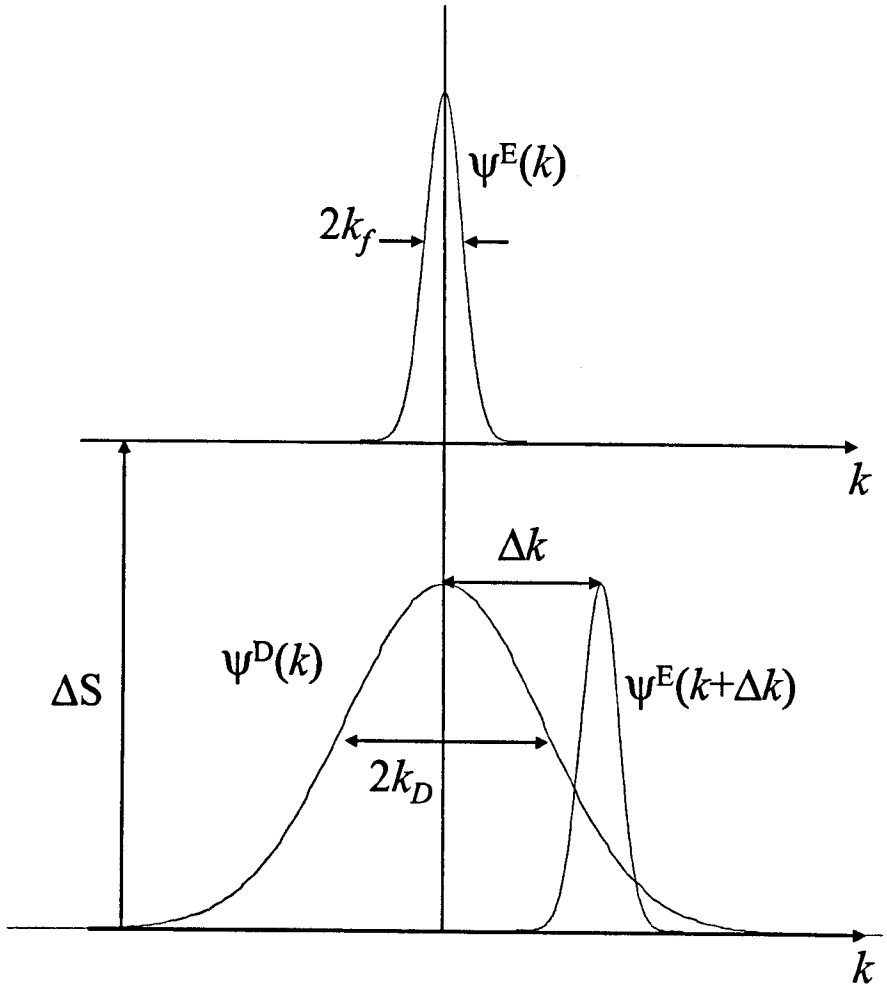

Figure 3-3: The figure represents the expected overlap between the emitter and donor state wavefunctions in an a magnetic field. The emiter wavefunction $\psi^E(k)$ can be seen to gain additional in plane mometum Δk, due to the magnetic field over a distance Δs. As the emitter state wavefunction remains unchanged the change in the overlap intergral can be seen to be due to the variation in the donor wavefunction $\psi^D(k)$ with k.

state wavefunction is unchanged, the change in current will be proportional to the variation of the probability density of the donor state wavefunction with k,

$$I \propto |M|^2 \propto |\psi^D(k_x, \Delta k_y)|^2. \tag{3.17}$$

By plotting the normalised resonant peak height against $B_\perp$ or equivalently Δk_y, we are therefore plotting the qualitative variation of probability density dependence of the donor state wavefunction.

3.4 Magneto tunneling spectroscopy and Si-donors in GaAs -background and comparison with the model of Sakai et al.

Previous work by Sakai et al. [1] used MTS to map the probability density of Si-donor states in the centre of a GaAs quantum well for the case of a magnetic field perpendicular to the current direction only. The following is an overview of the MTS technique applied to our sample; note the sample is very similar to that used by Sakai et al. The sample is a double barrier structure with conduction band profile under bias as shown in figure 3-4. For the purposes of repeating and checking the previous work by Sakai et al, we will first consider a magnetic field perpendicular to the current direction only. We define the axes as before, so that z is perpendicular to the QW plane and parallel to the current direction. The xy plane is parallel to the QW plane. As shown in the previous section we can use a magnetic field applied perpendicular to the tunnel current to tune a specific value of Δk. As the tunnel current is proportional to the overlap between the emitter and the donor state wavefunctions, at Δk, we can map the probability density of the donor state wavefunction in k.

The magnetic field is $\mathbf{B} = (B_\perp, 0, 0)$. A vector potential $\mathbf{A} = (0, -zB_\perp, 0)$ can be

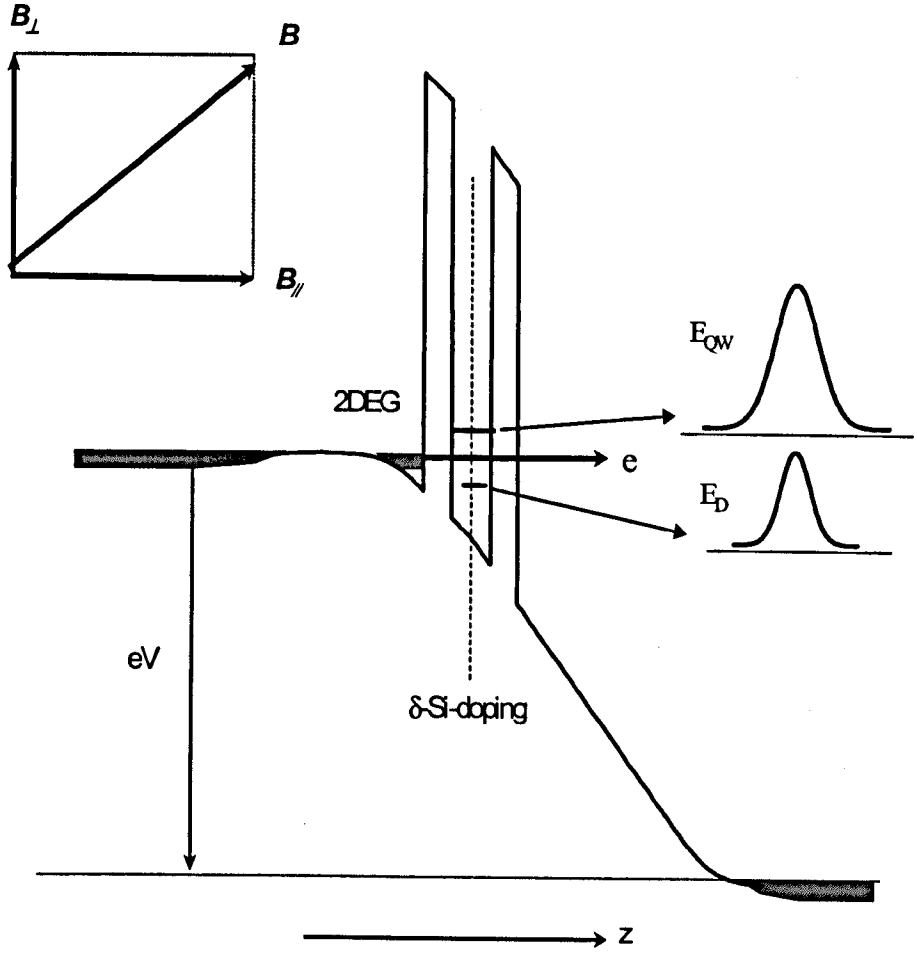

Figure 3-4: The expected conduction band profile of the samples under bias voltage V. A representation of the from of the donor and first QW states along z is also shown. The magnetic field B applied can be seen in the upper left inset with its components of B parallel and perpendiculer to the current direction. The right hand inset shows the form of the QW and donor wavefunction along z.

used to represent the magnetic field. The perpendicular magnetic field is applied in the x-direction i.e. $B_\perp \equiv B_x$. For the emitter states we have

$$H^E = \frac{1}{2m}(\mathbf{p} + e\mathbf{A})^2 + V^E(z) \tag{3.18}$$

and

$$= \frac{\mathbf{p}_x^2}{2m} + \frac{\mathbf{p}_z^2}{2m} + \frac{(\mathbf{p}_y - eB_\perp z)^2}{2m} + V^E(z), \tag{3.19}$$

where $V^E(z)$ is the confining potential in the z direction. The Shrödinger equation is separable into the form $\Psi^E(x,y,z) = X^E(x)\phi^E(y,z)$,however, the emitter states are confined in the z direction due to the large vertical energy splitting between the sub-bands. We can therefore write the approximate form as $\Psi^E(x,y,z) = X^E(x)\varphi^E(y)\chi^E(z)$. As $\mathbf{p}_x$ commutes with H^E, we can choose a wave function of the form

$$\Psi^E(x,y,z) = e^{ik_x x}\varphi^E(y)\chi^E(z). \tag{3.20}$$

Inserting equation 3.20 into 3.19 and averaging over the unperturbed emitter bound state $\chi^E(z)$ we arrive at

$$H^E_{av} = \frac{1}{2m}\left[\mathbf{p}_x^2 + (\mathbf{p}_y - eB_\perp < z >_E)^2\right] + \Delta E_z + E_z, \tag{3.21}$$

where $E_z = \mathbf{p}_z^2/2m + V^E(z)$ and the diamagnetic energy shift is given by $\Delta E_z = \frac{e^2B_\perp^2}{2m}(< z^2 >_E - < z >_E^2)$. Setting the momentum change in y so that $eB_\perp < z >_E = \hbar\Delta k_y^E$ and defining $\Psi^E(y) = \exp(-i\Delta k_y^E y)\varphi^E(y)$ we need only deal with the effective Hamiltonian, $H^E_{eff}\Psi^E(y) = E^E_{eff}\Psi^E(y)$ given by

$$H^E_{eff} = \frac{1}{2m}[\mathbf{p}_x^2 + \mathbf{p}_y^2], \tag{3.22}$$

which corresponds to a plane wave state. The emitter state wave function is therefore

$$\Psi^E(x,y,z) = e^{ik_x^E x} e^{i(k_y^E - \Delta k_y^E)y} \chi^E(z). \tag{3.23}$$

Considering the donor states for a magnetic field of $\mathbf{B} = (B_\perp, 0, 0)$ and assuming the donor confinement potential is separable, the Hamiltonian is

$$H^D = \frac{1}{2m}(\mathbf{p} + e\mathbf{A})^2 + V^D(x,y) + V^D(z), \tag{3.24}$$

where $V^D(x,y)$ is the confinement in the xy plane of the donor state and $V^D(z)$ the z direction confinement. If we assume a parabolic potential for the donor state confinement $V^D(x,y) = m\omega_0^2(x^2+y^2)/2$, the donor state Hamiltonian becomes

$$H^D = \frac{1}{2m}(\mathbf{p}_x^2 + \mathbf{p}_z^2 + (\mathbf{p}_y - ezB_\perp)^2) + \frac{1}{2}m\omega_0^2(x^2+y^2) + V^D(z). \tag{3.25}$$

Assuming the wavefunction is separable we try $\Psi^D(x,y,z) = \varphi^D(x,y)\chi^D(z)$ as a solution to the wavefunction and average over the unperturbed donor state $\chi^D(z)$. This gives

$$H_{av}^D = \frac{1}{2m}[\mathbf{p}_x^2 + (\mathbf{p}_y - e < z >_D B_\perp)^2] + \frac{1}{2}m\omega_0^2(x^2+y^2) + \Delta E_z + E_z, \tag{3.26}$$

where $E_z = \frac{\mathbf{p}_z^2}{2m} + V^D(z)$, $\Delta E_z = e^2 B_\perp^2(< z^2 >_D - < z >_D^2)/2m$ and the momentum shift $\hbar\Delta k_y^D = eB_\perp < z >_D$. The averaged Hamiltonian has the form of a simple harmonic oscillator with diamagnetic energy shift ΔE_z and momentum shift $\hbar\Delta k_y^D$. Defining $\Psi^D(x,y) = \exp(-i\Delta k_y^D y)\varphi^D(x,y)$ allows us to deal with the effective Schrödinger equation $H_{eff}^D \Psi^D(x,y) = E_{eff}^D \Psi^D(x,y)$ and Hamiltonian

$$H_{eff}^D = \frac{1}{2m}[\mathbf{p}_x^2 + \mathbf{p}_y^2] + \frac{1}{2}m\omega_0^2(x^2+y^2). \tag{3.27}$$

Recognising that equation 3.27 has the form of a simple harmonic oscillator we can

now write the unnormalised wave function as

$$\Psi^D(x,y,z) = e^{\left(-\frac{m\omega_0}{2\hbar}(x^2+y^2)\right)} e^{(i\Delta k_y^D y)} \chi^D(z). \tag{3.28}$$

Substituting equation 3.28 and 3.23 into equation 3.14 and performing a Fourier transform gives

$$I \propto e^{(-l_0^2 \Delta k_y^2)}, \tag{3.29}$$

where $\Delta k_y = eB_\perp(< z >_E - < z >_D)/\hbar = eB_\perp \Delta s/\hbar$, where Δs is the tunneling distance and $l_0^2 = (\hbar/m\omega_0)$ is the real space extent of the donor wavefunction. The only variables in the current dependence are the tunneling distance Δs and the real space extent of the donor wavefunction l_0. The data is fitted using the product $S = \Delta s l_0$, as the fitting parameter i.e.

$$I \propto \exp\left(-\frac{S^2 e^2}{\hbar^2} B_\perp^2\right). \tag{3.30}$$

3.4.1 Discussion of the result of Sakai et al.

Sakai et al. [1] first found the peak in the I(V) measurements of a QW with Si doping in the central plane of the QW [1]. They showed that the peak lay below the first QW resonance and it was created by tunneling through donor states, feature D, figure 3-5. As the magnetic field perpendicular to the current direction is increased, the current amplitude of feature D decreases. Differentiating the curves of figure 3-5 leads to a plot of the differential conductance with a clear peak in the differential conductance due to tunneling into the donor states. Measuring the differential conductance height of this peak it was found to vary in the same way with $B_\perp$ as the amplitude of the current peak after the background current had been deducted. We believe the background current is the threshold of tunneling into the 2-D sub-band of the QW. Extracting the conductance peak height from the data proved easier than

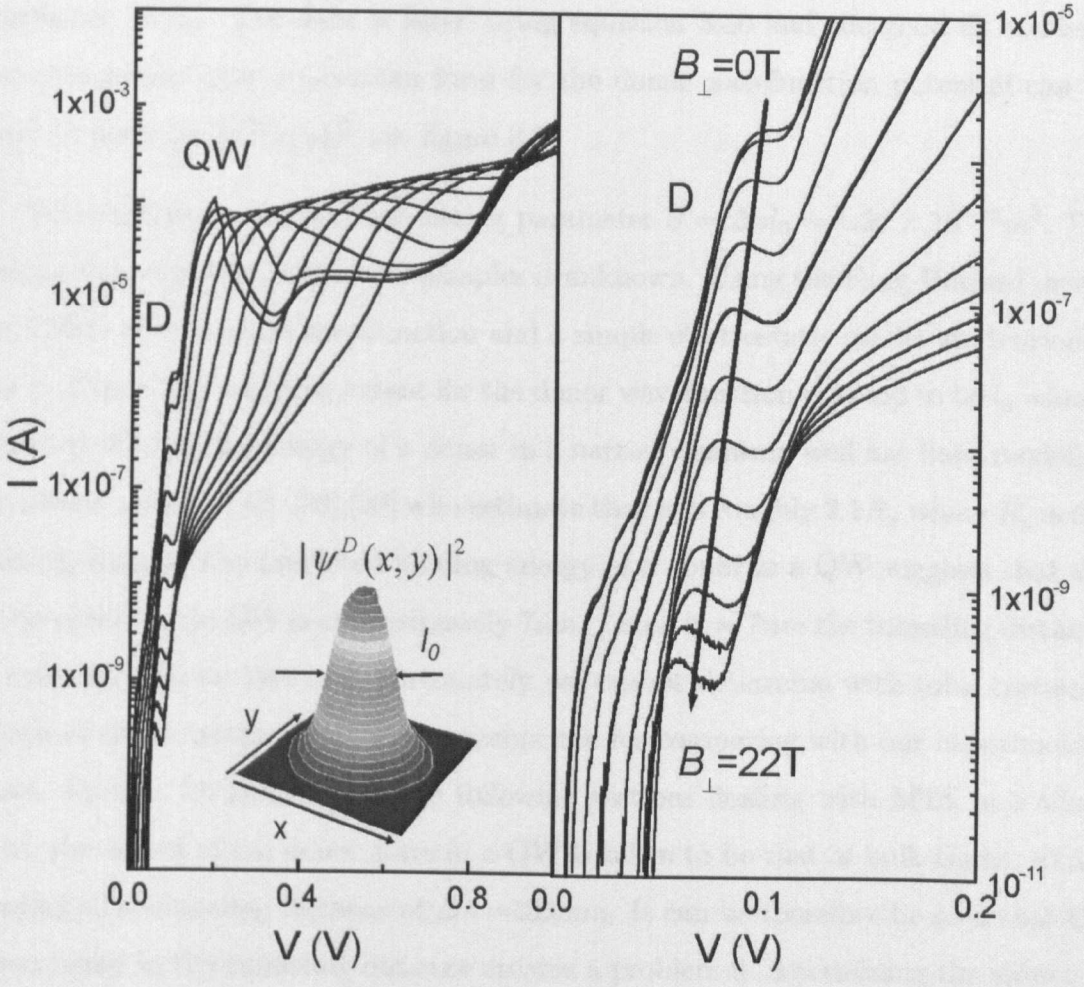

Figure 3-5: Left: Low temperature I(V) characteristics of the device, under applied perpendicular magnetic fields ranging from 0 T to 22 T, increasing in steps of 2 T, $B_{||} = 0T$. The small feature below threshold for tunnelling into the first QW subband arises from tunnelling into the 1s impurity state. Right: Enlargement of the donor-resonance region, showing the evolution of the peak position and intensity as the applied field increases. Inset: The donor probability density in momentum space, as obtained from the dependence of the donor peak current, exhibiting the circular symmetry in the QW plane of the 1s state.

obtaining the magnitude of the current peak, which requires fitting procedures and the subtraction of the background current. Therefore, the conductivity peak was a more convenient measure of the resonant peak height dependence with the magnetic field. Figure 3-6 shows the normalised conductivity peak height plotted against the amplitude of B_x. The data is fitted using equation 3.30 and the good fit confirms the assumption that a Gaussian form for the donor wavefunction potential can be used to describe $|\psi^D(x,y)|^2$, see figure 3-6.

We determine a value of the fitting parameter $S = \Delta s l_0 = 1.36 \times 10^{-16} m^2$. The precise tunneling distance in our samples is unknown. Using the Fang-Howard model for 2DEG emitter state wavefunction and a simple electrostatic model we determine $\Delta s = 27$nm. The resulting extent for the donor wavefunction is found to be l_0 =5nm. However the binding energy of a donor in a narrow quantum well has been modelled by several authors [40], [38],[39] who estimate that it is roughly $2.1R_y$ where R_y is the Ryberg energy. The predicted binding energy of a donor in a QW suggests that the Bohr radius in the QW is approximately 7nm. Using $l_0 = 7nm$ the tunneling distance is calculated to be 19nm. Unfortunately we cannot determine with total certainty which of these results is the most appropriate for comparing with our experimental data. Finally, for reference in the following sections dealing with MTS in a tilted field, the extent of the donor state in a QW is taken to be that of bulk GaAs, 10nm, leading to a tunneling distance of Δs =13.5nm. It can be therefore be seen that the uncertainty in the tunneling distance creates a problem in determining the extent of the wavefunction.

We now consider the validity of each of the three cases of $l_0 = 5, 7, 10$nm. From electrostatic considerations of the resonant voltage, the electron density around resonance is estimated to be $n_{2D} = 1 \times 10^{-15} m^{-2}$. A tunneling distance of 27nm is indicated by the using the Fang-Howard form of a 2DEG wavefunction with this electron density, leading to standoff distance of $< z_{FH} >$=17nm. The corresponding wavefunction extent of, l_0 =5nm, although showing that the donor state wavefunction is compressed by the QW, is significantly smaller than predicted by theory. We cannot provide an explanation why this may be the case. The theoretically predicted

wavefunction extent $l_0 = 7nm$ has a corresponding emitter state wavefunction standoff distance of $< z_{FH} >$=8.3nm. Both these values seem reasonable and agree with the expected values. The case of the donor state wavefunction remaining unchanged by the QW with $l_0 = 10nm$ yields a tunneling distance of Δs =13.5nm and an unlikely standoff distance of only $< z_{FH} >$=3nm. As the donor state wavefunction is expected to be compressed from the bulk value within the QW, this value appears unlikely. The standoff distance of 3nm is far smaller than can be expected using the Fang-Howard model with the electrostatically estimated electron density. The wavefunction extent of 10nm does however, agree reasonably with that of previous work by Sakai et al. of 9.4nm. However, in the following section dealing MTS in tilted magnetic fields we argue that an effective tunneling distance of 13.5nm provides the best fit to the data.

The fit in figure 3-6 can be seen to be poor when viewed in the logarithmic scale for high values of $B_\perp$. Such a deviation may be due to the following reasons. Firstly, we expect there to be some leakage in the device and there to be a background current present in the I(V) curves. At low currents $\backsim 1 \times 10^{-9} A$, like those found when $B_\perp > 12T$, the effect of this small current becomes proportionally greater and the data deviates from the model. For the data points at low magnetic field the currents are sufficiently large, $\backsim 1 \times 10^{-6} A$, that any background current effects are small when compared to the signal, allowing the data to be fitted over two decades of I. At high magnetic fields it may be possible that the assumption that the Bardeen transfer matrix is independent of magnetic field is invalid and the deviation is due to a change in the transfer matrix element at high fields. Finally, the model may be too simplistic. It is believed that due to the success of the previous work using MTS that the model is reasonable and that it is most likely the background leakage current that creates this deviation between fit and data. We believe the data points taken at low magnetic fields are more accurate than those taken at high magnetic fields and the deviation between the model and data, at large values of probing magnetic field, is not considered significant.

The previous magneto-tunnelling measurement by Sakai et al. [1] of donor states

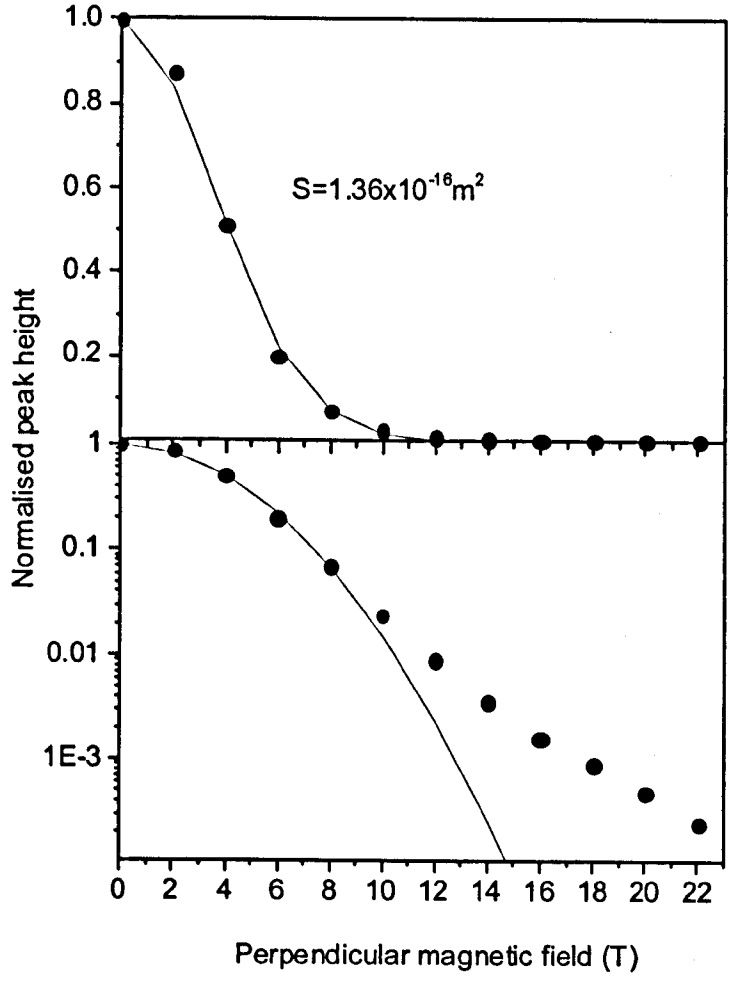

Figure 3-6: The normalised conductance peak height dependence on the probing perpendicular magnetic field. The circles represent the measured peak hieghts and the solid line is the fit using equation 28. The value of the fitting parameter S is shown. The lower figure is the same plot as above but on a logarithmic scale.

did not determine the wavefunction from consideration of the Hamiltonian. Instead they assumed a wavefunction of the form

$$f(y) = A\exp[-y^2(\lambda^{-2} + ql_b^{-2})], \tag{3.31}$$

where λ is the decay length of the wavefunction related to our l_0 as $\lambda = \sqrt{2}l_0$, $l_b = (\hbar/eB_\perp)^{1/2}$ and q a phenomenological (i.e. adjustable) dimensionless parameter. The equation is very similar to that we propose here except for the ql_b^{-2} term. Such a term allows their model to cope with the idea that at high magnetic fields the confinement is more due to the magnetic field than the donor state potential. A two parameter fitting of the natural log of the normalised current peak height and tunneling distance $\Delta s = 29nm$ gave Sakai et al. a wavefunction extent of $\lambda = 9.4nm$ ($l_0 = 6.7nm$) and $q = 0.8$. The analysis as used by Sakai et al. was applied to our data as shown in figure 3-7. Using a tunneling distance of 27nm (compared to their 29nm) we found the wavefunction extent to be $\lambda = 10.4$nm ($l_0 = 7.4nm$) and $q = 1.4$. Figure 3-7 shows that despite fitting the data seemingly well for a large range of $B_\perp$, for the low magnetic field values the fit is not indicative of the trend displayed by the data. The low magnetic field data points, which we feel are more accurate than the high magnetic field values, are not fitted well using the model of Sakai et al.

Again the uncertainty in the tunneling distance affects the result found using the model of Sakai et al. However, to achieve a decrease in the donor state wavefunction extent, the tunneling distance will need to be increased and any decrease in tunneling distance will create an increase in the wavefunction extent. We feel that as the model proposed by Sakai et al. does not describe the low magnetic field data points well, the model proposed in this thesis, is a more accurate method for understanding MTS through Si-donor states in a QW.

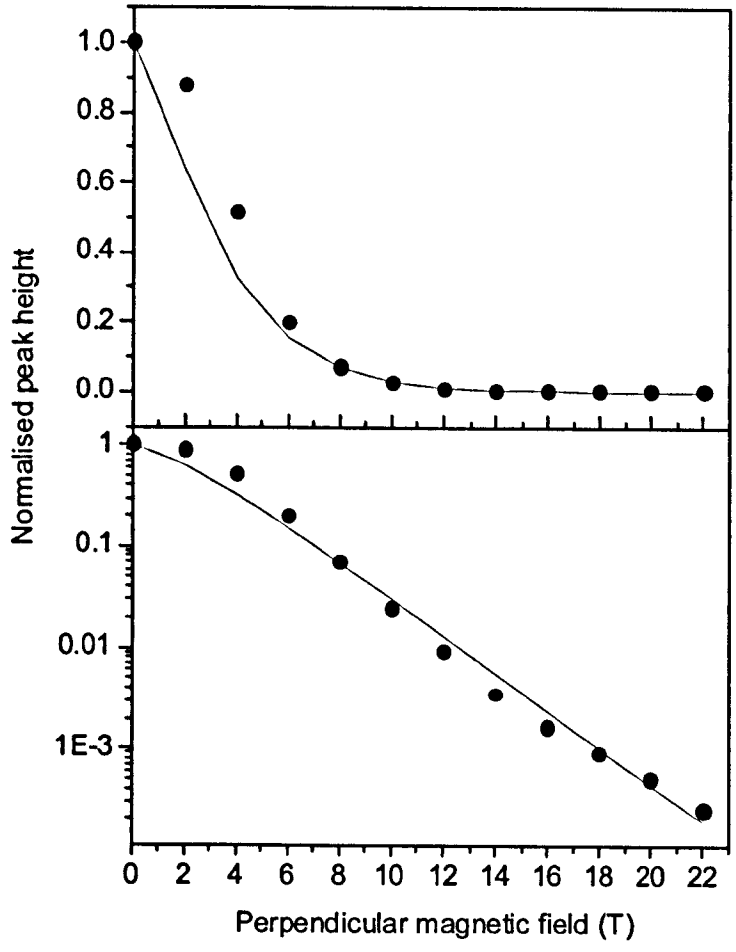

Figure 3-7: The normalised conductance peak height with applied magnetic field is shown. The circles represent the data and the solid line is the fit according to the formula of Sakai et al. [1].

3.5 Modelling magneto-tunneling spectroscopy in a tilted magnetic field for a Si-donor state.

We now consider the effect of compressing the donor wavefunction with a magnetic field applied in parallel with the tunneling electrons. The effect of a tilted magnetic field on the tunneling current through a donor state is modelled by F.W. Sheard and J. C. Arce [47] by using a tunnelling Hamiltonian approximation. A resonant tunneling structure of the type shown in figure 3-4 is considered. In the experiment, the tunneling current along the growth direction (which is defined as the z-direction) is measured in the presence of a magnetic field, B, tilted with respect to the z-axis.

As before, the system is divided into three subsystems: emitter (E), donor state (D) and collector (C). Each subsystem can then be described by an appropriate Hamiltonian, H^s, where s =E, D or C. Due to the lowering of the collector barrier under bias, which leads to a stronger coupling between the donor and collector states, the tunneling current I is limited mainly by tunneling through the emitter barrier [45]. Thus the current is proportional to the modulus squared of the product of the lateral tunneling matrix element, M, and the Bardeen transfer matrix element, T, between the emitter and the donor states, i.e. $I \backsim |MT|^2$ where

$$M = \int\int \varphi^{D^*}(x,y)\varphi^{E}(x,y)dxdy \tag{3.32}$$

and

$$T = \frac{\hbar^2}{2m}\left[\chi^E(z)\frac{d\chi^D(z)}{dz} - \chi^D(z)\frac{d\chi^E(z)}{dz}\right]. \tag{3.33}$$

Here we assume separability between the xy and the z-motion of the electrons. In these equations $\Psi^s(x,y,z) = \varphi^s(x,y)\chi^s(z)$, is the eigenstate of H^s and T is evaluated at a point in the barrier between the emitter and the δ-doped donor layer. A perturbation approach is used in which the squeezing effect of $B_\perp$ on the emitter bound state is neglected. The electronic states in the two-dimensional accumulation

emitter layer are given by

$$H^E = \frac{1}{2m}\left[(\mathbf{p}_x - eyB_{||})^2 + (\mathbf{p}_y + ezB_{\perp})^2 + \mathbf{p}_z^2\right] + V_c^E(z) + V_z^E(z), \tag{3.34}$$

where we have used the asymmetric gauge for the potential vector $\mathbf{A} = (-yB_{||}, -zB_{\perp}, 0)$, $V_c^E(z)$ is the conduction band potential and $V_z^E(z)$ is the confining triangular potential of the emitter layer. Since $\mathbf{p}_x$ commutes with the Hamiltonian, the emitter wave function can be written as the following form

$$\Psi^E(x,y,z) = \psi^E(x,y)\chi^E(z) = \frac{e^{ik_x x}}{L_x^{\frac{1}{2}}}\varphi^E(y)\chi^E(z), \tag{3.35}$$

where $\chi^E(z)$ is the unperturbed bound state in the emitter layer and L_x is a normalisation length. Averaging H^E over z, we obtain an effective Hamiltonian of motion in the xy plane,

$$H_{av}^E = \int \chi^{*E}(z)H^E\chi^E(z)dz = E_z^E + \Delta E_z^E + \frac{1}{2m}\left(\mathbf{p}_y + \Delta p_y^E\right)^2 + \frac{1}{2}m\omega_c^2(y - y_0)^2, \tag{3.36}$$

which has the form of an in-plane simple harmonic oscillator with a diamagnetic energy shift $\Delta E_z^E \equiv e^2B_{\perp}^2(< z^2 >_E - < z >_E^2)/2m$ and momentum shift $\Delta p_y^E = \hbar\Delta k_y^E \equiv e < z >_E B_{\perp}$, where $< z >_E = < \chi^{*E}(z)|z|\chi^E(z) >$ and $< z^2 >_E = < \chi^{*E}(z)|z^2|\chi^E(z) >$. Then by defining $\psi^E(y) = \exp(-i\Delta k_y^E y)\varphi^E(y)$, we find that

$$H_{eff}^E\psi^E(y) = E_{eff}^E\psi^E(y) \tag{3.37}$$

where H_{eff}^E is given by

$$H_{eff}^E = \frac{\mathbf{p}_y^2}{2m} + \frac{1}{2}m\omega_c^2(y - y_0)^2, \tag{3.38}$$

$\omega_c = eB_{||}/m$ the in-plane cyclotron frequency, $y_0 = l_b^2 k_x$ is the orbit centre position and $l_b = (\hbar/eB_{||})^{1/2}$ is the magnetic length. The solution for the y dependent part

of the emitter ground state wave function is therefore

$$\varphi_0^E(y) = \left(\frac{m\omega_c}{\pi\hbar}\right)^{1/4} \exp\left(-\frac{m\omega_c}{2\hbar}(y-y_0)^2 + i\Delta k_y^E y\right). \tag{3.39}$$

The Hamiltonian for an electron in a donor state is

$$H^D = \frac{1}{2m}\left[(\mathbf{p}_x - eyB_{||})^2 + (\mathbf{p}_y + ezB_\perp)^2 + \mathbf{p}_z^2\right] + \frac{1}{2}m\omega_0^2(x^2+y^2) + V_c^D(z) + V_z^D(z), \tag{3.40}$$

where we have assumed a parabolic confinement potential for the donor and ω_0 is the confinement frequency. Taking the effect of $B_\perp$ on the squeezing of the donor wavefunction in the z direction to be small [1],[8], we try a separable wavefunction of the form $\Psi^D(x,y,z) \cong \varphi^D(x,y)\chi^D(z)$, where $\chi^D(z)$ is identical to the unperturbed state. Averaging the Hamiltonian over z gives an average Hamiltonian for motion in the (x,y) plane

$$H_{av}^D = E_z^D + \Delta E_z^D + \frac{1}{2m}\left[(\mathbf{p}_x - eyB_{||})^2 + (\mathbf{p}_y + \Delta p_y^D)^2\right] + \frac{1}{2}m\omega_0^2(x^2+y^2). \tag{3.41}$$

This describes a simple harmonic oscillator with diamagnetic energy shift $\Delta E_z^D \equiv e^2B_\perp^2(< z^2 >_D - < z >_D^2)/2m$ and momentum shift $\Delta p_y^D = \hbar\Delta k_y^D \equiv e < z >_D B_\perp$. By making the transformation $\psi^D(x,y) \equiv \exp(-i\Delta k_y^D y)\varphi^D(x,y)$, we derive the effective Hamiltonian for the state $\varphi^D(x,y)$

$$H_{eff}^D = \frac{1}{2m}\left[(\mathbf{p}_x - eyB_{||})^2 + \mathbf{p}_y^2\right] + \frac{1}{2}m\omega_0^2(x^2+y^2). \tag{3.42}$$

In view of the symmetry of the donor potential, a more suitable gauge for this problem is the symmetric gauge with $\mathbf{A} = (-yB_z/2, xB_z/2, 0)$ which leads to the Hamiltonian

$$H_{eff}^{'D} = \frac{1}{2m}(\mathbf{p}_x^2 + \mathbf{p}_y^2) + \frac{1}{2}m\omega_{eff}^2(x^2+y^2) + \frac{1}{2}\omega_c\hat{L}_z, \tag{3.43}$$

where $\omega_{eff}^{'D} = \omega_0^2 + \omega_c^2/4$. For the ground state we may take $L_z = 0$ and the wave

function in the symmetric gauge is therefore

$$\psi'^{D}_{0,0}(x,y) = \left[\frac{m(\omega_0^2+\omega_c^2/4)^{1/2}}{\pi\hbar}\right]^{1/2} \exp\left[-\frac{m(\omega_0^2+\omega_c^2/4)^{1/2}}{2\hbar}(x^2+y^2)\right] \tag{3.44}$$

Examination of equation 3.44 reveals that it is Gaussian in form and therefore has a characteristic width $l_D = \sqrt{\hbar/m(\omega_0^2+\omega_c^2/4)^{1/2}}$. Performing a gauge transformation, we recover the ground state wavefunction for the asymmetric gauge and we find the wave function is now given by

$$\varphi^{D}_{0,0}(x,y) = \exp\left(\frac{im\omega_c xy}{2\hbar}\right)\psi'^{D}_{0,0}(x,y). \tag{3.45}$$

Equation 3.44 shows that as $B_{||}$ is increased there is a corresponding compression of the wave function in the xy plane. We are then able to model the extent of the donor wavefunction with changing $B_{||}$ using the parameter

$$l_D = l_0\left(1+\frac{l_0^4}{4l_b^4}\right)^{-1/4} \tag{3.46}$$

where $l_0 = (\hbar/m\omega_0)^{1/2}$ is the real space zero field extent of the donor wavefunction and $l_b = (\hbar/eB_{||})^{1/2}$.

The current is determined using equations 3.32 and 3.33 with the derived expressions for the wave functions. In particular, since we assumed that $\chi^D(z)$ and $\chi^E(z)$ are unperturbed by $B_{||}$ and $B_\perp$, the B-dependence of current can be approximated by

$$I \propto |M_{xy}|^2 \sim \exp\left[-\frac{\hbar}{m(\Omega+\omega_c)}\Delta k_y^2\right], \tag{3.47}$$

which corresponds to a Gaussian of width $\left[\frac{\hbar}{m(\Omega+\omega_c)}\right]^{1/2}$ and $\Omega = (\omega_0^2+\omega_c^2/2)/(\omega_0^2+\omega_c^2/4)^{1/2}$. Equation 3.47 is used to model the conductivity peak height dependence. For $B_{||} = 0T$, the confinement due to the parallel field is zero and $(\Omega+\omega_c) = \omega_0$. This is the same result as the non-tilted field case described earlier. The conductivity peak height dependence on the probing perpendicular field $B_\perp$ for $B_{||} = 0T$ is then

fitted with

$$I \propto \exp(-l_0^2 k^2) = \exp\left(\frac{l_0^2 \Delta s^2 e^2}{\hbar^2} B_\perp^2\right) \tag{3.48}$$

where Δs is the tunneling distance and l_0 is the fitting parameter and corresponds to the real space extent of the tunneling matrix Gaussian. Note that l_0 also corresponds to the $B_{||} = 0$T extent of the donor state. Using the zero field value for l_0, as found in the non-tilted field case, the value of ω_0 is deduced and then placed in equation 3.47 to model the parallel field dependence of the conductivity peak height. Having obtained l_0 from the data for $B_{||}$=0, no further fitting parameters are used to generate the curves for non-zero $B_{||}$, which follow directly from equation 3.47

Unlike previous MTS experiments the probability density of the confined states wavefunction examined i.e. donor states, is not measured directly when $B_{||} \neq 0T$. Instead we measure the transfer matrix between the donor state and the emitter state. If the model describes the data satisfactorily we assume the model is correct and that the form of the donor wavefunction calculated is correct. Using equation 3.46 we can then show what we believe the extent of the magneto-compression experienced by the donor state.

3.6 Experimental results for MTS in tilted magnetic fields

As seen for the non-tilted case, the tunneling of electrons from the emitter accumulation layer into the 1s ground state of the QW-confined donors generates a resonant peak (feature D in Figure 3-5) in the current-voltage, I(V), characteristics [1]. This peak occurs at a bias close to the threshold for tunneling into the lowest energy sub-band of the QW (feature E1 in Figure 3-5). In the presence of a magnetic field, $B_\perp$, applied in the plane of the QW, the intensity of the current feature D decreases monotonously with increasing $B_\perp$. We can understand this magnetic field dependence in terms of the effect of $B_\perp$ on a tunneling electron, where an electron that

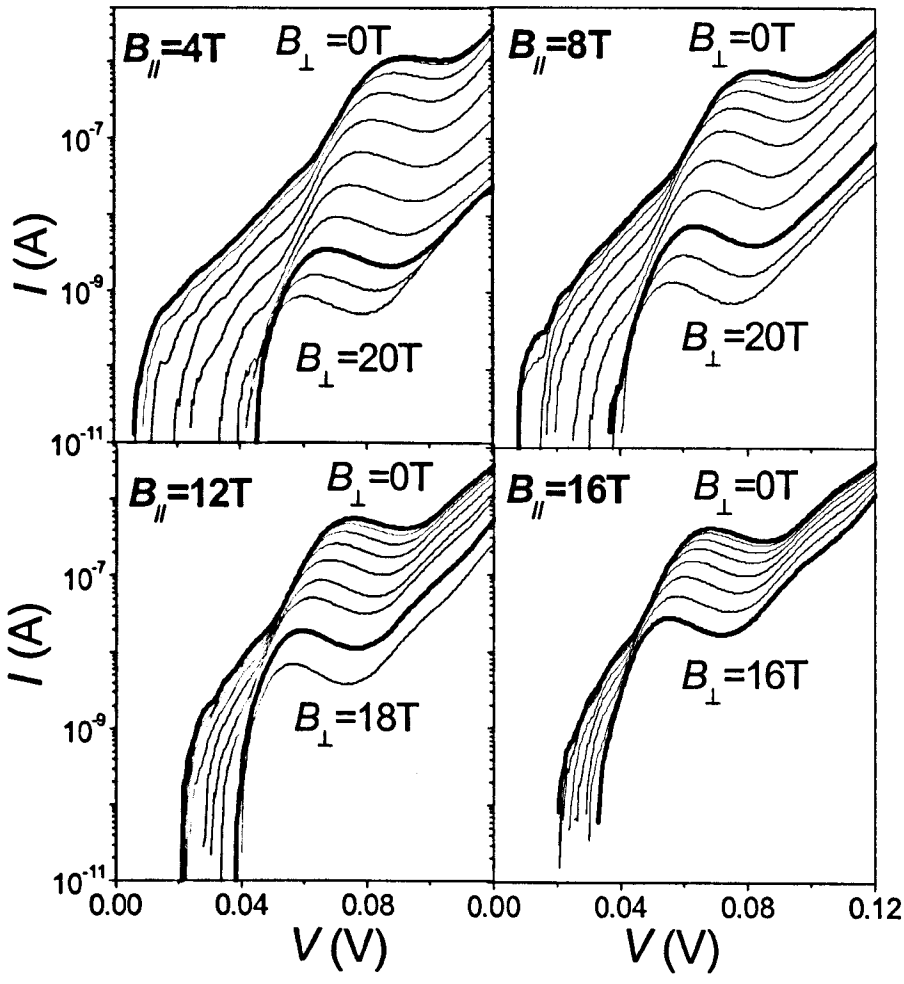

Figure 3-8: Low temperature I(V) characteristics of the device, under applied tilted magnetic fields, in the donor peak region. Each section shows data for a particular value of $B_{||}$ and for a range of $B_{\perp}$ values increasing in steps of 2 T. As a visual guide, the curves for $B_{\perp}$=0 T and 16 T have been drawn with thick lines.

resonantly tunnels from the emitter into the 1s donor impurity ground state acquires a momentum component in the plane of the QW given by $\hbar\Delta k = eB_{\perp}\Delta s$. By measuring the tunnel current $I(B_{\perp})$ as a function of $B_{\perp}$ for the $B_{||} = 0$ case, we find $\psi^{D}(k_x, k_y) \propto \exp(l_0^2 k^2)$ and determine l_0 (10nm). Using l_0 we calculate a value for ω_0 ($1.72 \times 10^{13}\text{rads}^{-1}$) and using equation 3.47 predict the magneto-compression of $B_{||}$ on the donor state.

Figures 3-8(a), (b), (c) and (d) show the dependence on **B** of the I-V curves for different intensities of magnetic field $B_{||}$, parallel to the current direction. The I-V data clearly indicates that feature D displays a weaker dependence on $B_{\perp}$ with increasing $B_{||}$. This effect is consistent with the magneto-compression effect of the donor wavefunction expected in tilted magnetic fields. The magneto-compression of the real-space wave function leads to a more extended probability density in Fourier space $|\varphi_{1s}^{D}(k)|^2$ and hence a weaker dependence of $I \propto |\varphi_{1s}^{D}(k)|^2$ on $B_{\perp} \backsim k$ for large values of $B_{||}$. The data shows that the component of magnetic field parallel to the current direction, $B_{||}$, provides a means of compressing the wave function in real space.

The value for the extent of the wavefunction for $B_{||} = 0T$, is $l_0 = 10nm$, assuming $\Delta s = 13.5$nm, see figure 3-6 with a corresponding $\omega_0 = 1.72 \times 10^{13}\text{rads}^{-1}$. Placing the deduced value of ω_0 in equation 3.47 models the parallel field dependence of the conductivity peak height. Figure 3-9 shows the comparison between the model and experimental values for the conductivity peak height dependence on $B_{\perp}$. The data and theory show an excellent match for all values of the compressing magnetic field $B_{||}$. A logarithmic replot of the data in figure 3-10 shows the difference between the data and theory for high values of $B_{\perp}$. The difference is only found when $B_{||} = 0$ and 4T. For higher values of $B_{||} = 8 - 20$T the correlation improves and the data and the predicted dependence on $B_{||}$ match.

Examining equation 3.48 shows that it is a Gaussian of the form $\exp(-C^2B^2)$, where C is the characteristic width of the Gaussian. Using our model for the transfer matrix variation we are able to predict the variation of C with $B_{||}$. Figure 3-11 shows

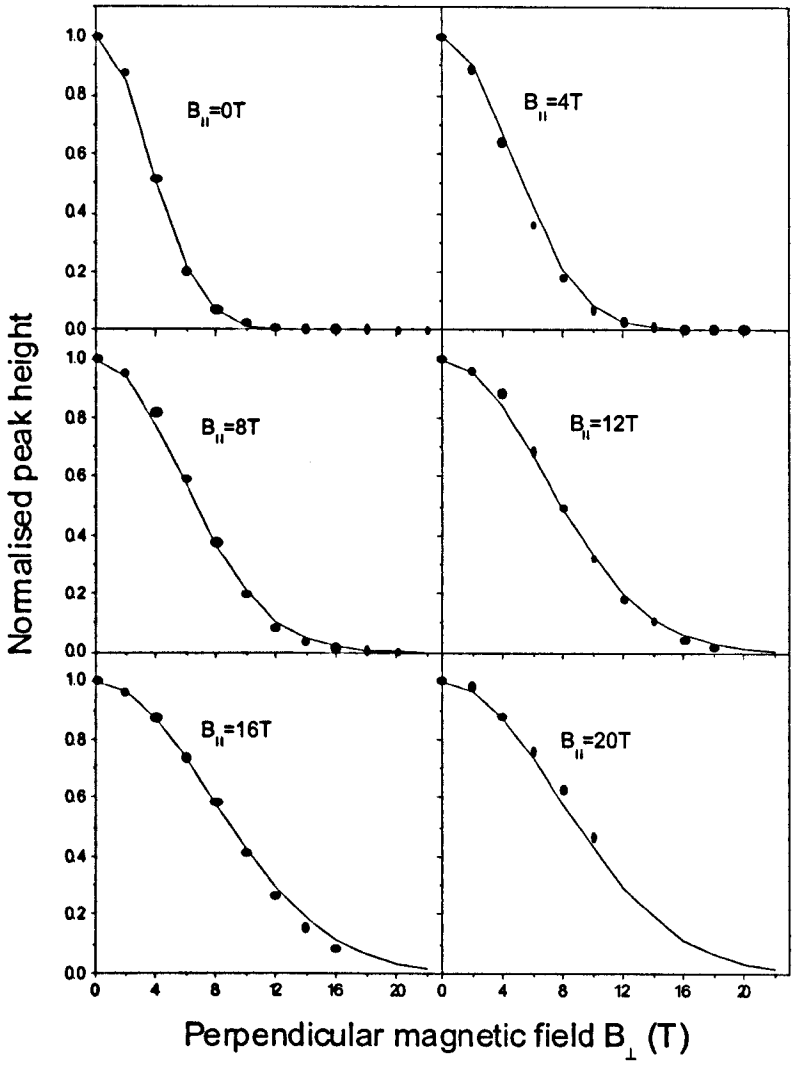

Figure 3-9: The normalised conductivity peak height dependence on perpendicular magnetic field is shown for different values of the parallel magnetic field. The circles correspond to the data points and the solid lines are those predicted by the model.

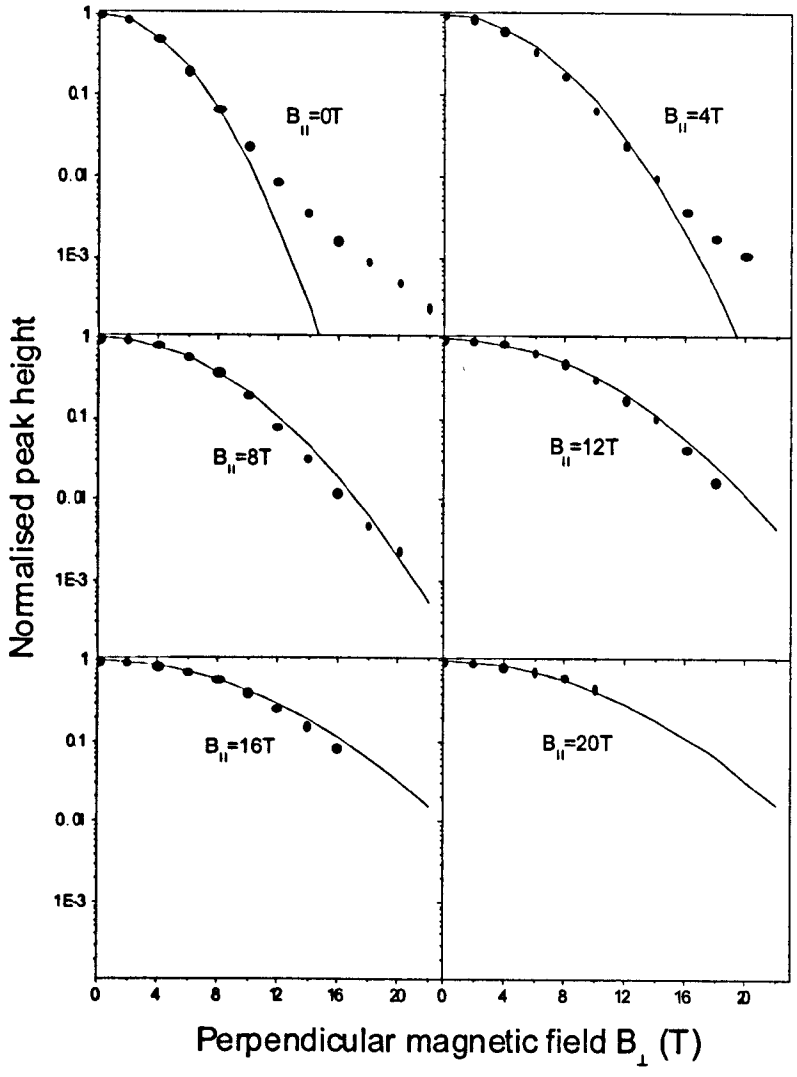

Figure 3-10: The normalised conductivity peak height dependence on perpendicular magnetic field is shown for different values of the parallel magnetic field. The circles correspond to the data points and the solid lines are those predicted by the model.

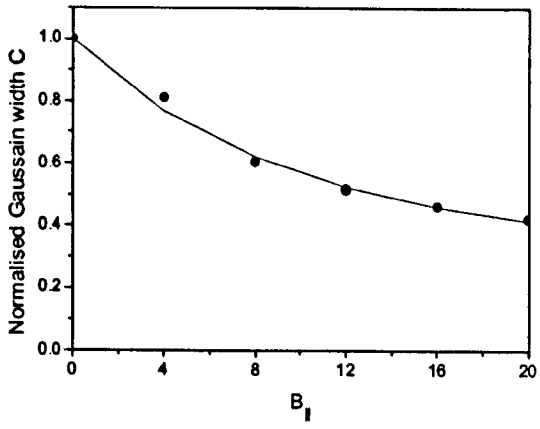

Figure 3-11: For each value of $B_{||}$ a Gaussian of width C is fitted to the data points. The figure shows how C varies with $B_{||}$. The circles show the values of C and the solid line is how we predict C varies with $B_{||}$.

how C varies with $B_{||}$ and how using only one fit, at $B_{||} = 0$T, the model predicts the magneto-compression of the transfer matrix. This result is essentially that seen already in figure 3-9. However, figure 3-11 shows clearly that the real-space extent of the transfer matrix gaussian is compressed with increasing magnetic field.

The effect of $B_{||}$ on the donor state width is predicted by the model in equation 3.46. Assuming that our model is correct then figure 3-12 shows the magneto-compression of the donor state due to $B_{||}$. The donor state is compressed from 10nm at $B_{||} = 0$T to 7.43nm at $B_{||} = 20$T.

3.7 Discussion

The results of the non-tilted magnetic field case showed that there was some uncertainty in the tunneling distance. By choosing different tunneling distances it is possible to drastically change the extent of the donor state wavefunction at $B_{||} = 0$T. The model presented in this chapter relies solely on the value of l_0 calculated from the fit of the data at $B_{||} = 0$T. If larger tunneling distances are chosen then l_0 becomes smaller in value and the model can no longer correctly predict the extent of

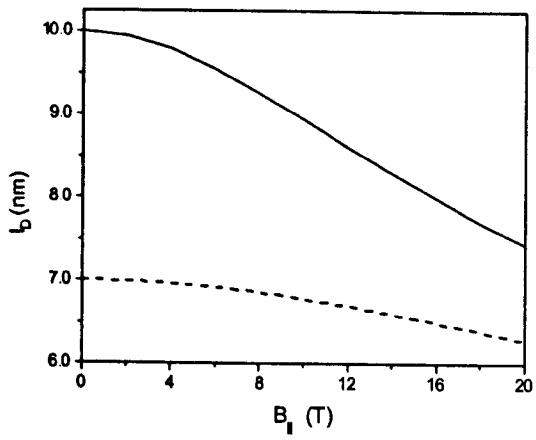

Figure 3-12: The real space extent of the donor wavefunction calculated using equation 45 is plotted against $B_{||}$. The solid line is calculated assuming $l_0 = 10nm$ the dotted line using $l_0 = 7nm$. The magneto-compression can be seen to be greater for the solid line.

the magneto-compression due to $B_{||}$. The following discussion therefore concerns what value should we choose for Δs.

The combination of the QW half width and barrier thickness provides a physical limit for the tunneling distance of $\Delta s \geq 10.2$nm. If the total tunnel distance was 13.5nm as used in the analysis the stand-off distance of the emitter state accumulation layer from the tunnel barrier would be $\backsim$ 3.3nm. Using the Fang Howard approximation, the sheet density needed to obtain a stand-off distance of 3nm is $\backsim 2 \times 10^{13}\text{cm}^{-2}$, such a sheet density is considered physically unreasonable for this system. The sheet density in the accumulation layer was estimated by electrostatics and a sheet density of $\backsim 1 \times 10^{11}\text{cm}^{-2}$ was found. The Fang-Howard approximation for the mean electron position then leads to a stand-off distance of $\approx$ 17nm. This value for the stand-off distance of the emitter states equates well with that of previous work on similar samples $\approx$ 19nm [1]. Since the stand-off distance is determined by the sheet density in the accumulation layer and since it is not unreasonable to assume a sheet density anywhere between $1 \times 10^{11}\text{cm}^{-2}$ and $10 \times 10^{11}\text{cm}^{-2}$ we can therefore expect a possible variation in the stand-off distance to be between $8-17$nm.

The trend shown by the data is described very well using a tunneling distance of 13.5nm. Whilst initially such a distance seems physically unreasonable we believe that 13.5nm is correct for the tunneling distance. We justify this unlikely conclusion with the following reasons: The emitter state wavefunction may be squeezed against the barrier by the applied magnetic field. However, we expect this effect will be small and unlikely to shrink the tunneling distance a large amount. Unlike previous MTS experiments (except for Sakai et al. [1]) the structures we are mapping using MTS are charged donor states. Although the average position of a donor is the centre of the QW; it is possible that donors may diffuse away from the centre of the QW during the growth process. Electrons tunneling into the QW may be scattered by these displaced donors. The scattering could lead to an average ballistic tunnel length that is shorter than expected. We envisage this process as randomising the momentum gain of a tunneling electron by scattering. An electron gains an in-plane momentum due to the magnetic field $\Delta k = e\Delta z B_\perp/\hbar$ where Δz is the distance tunneled before the electron is scattered. The scattering should be a random process and the electrons finish the process on average with a new value of momentum of $k = 0$. The electron therefore starts gaining momentum again before reaching the average donor state position in the centre of the well. The electron, for the purposes of the experiment, would travel an effective tunneling distance of $\Delta s_{eff} = \Delta s - \Delta z$ which represents the distance covered by the last scattering event and the arrival of the electron on the donor state in the QW. Here Δs is the distance between the emitter state wavefunction peak to the centre of the well.

It is possible that $\Delta s \neq$13.5nm, which would indicate that our model is too simplistic. Unfortunately, there is no obvious and simple way to improve the model. One possible reason is that there may be a limit to the MTS technique when applied to donor states. Throughout we have assumed that $B_\perp$ does not affect the tunneling matrix. However, in the course of the experiment we apply very high magnetic fields to the samples. The size of the donor state confinement has been estimated as between 5-10nm compared to that of previous work on quantum dots of 2nm in the z direction. The magnetic length at B =10T is $l_b = 8.1nm$ which is comparable to the

donor state confinement. It is therefore possible that for magnetic fields B > 10T the magnetic field will create extra confinement of the donor state resulting in an increased binding energy and greater confinement. The data taken at $B_{||} = 0$T does show a deviation from that predicted by the model at 10T. If the total applied magnetic field is greater than ten tesla we would expect to see greater confinement in the data, as observed in figure 3-10. Experimentally such a dependence can be tested by repeating the experiment but not applying a magnetic field greater than 10T and taking more low field measurements. Using a physically reasonable tunneling distance of $\Delta s = 18 - 30nm$ it is possible that the magneto-compression would be described by the model. We effectively impose a high field limit on the experiment that $l_b > l_D$ where l_b is the magnetic length due to the total applied field and l_D is the extent of the state being probed. Such an experiment could be criticised however, as ignoring the data that does not fit the model. It may be that we need to consider using the total applied magnetic field as the compressing field. Whether or not the technique would remain a valid approach would be in question if we consider the total applied field as the assumption of separability of the magnetic field may be violated.

In choosing $\Delta s = 13.5nm$ the extent of the donor state when $B_{||} = 0$T is found to be 10nm. Theoretical studies suggest that the donor state should have an extent of 7nm. A simple explanation of why we measure the larger extent of 10nm is not obvious. One possibility is the spread of the donor state due to diffusion in the QW. The diffusion will smear out the donor states and create the effect of broadening the measured probability density. Another possibility is that many donor states are at the edge of the QW. If we say that the barrier is quasi-infinite, the ground state of the electron bound to an impurity at the GaAs/(AlGa)As interface will be much more extended than one bound to a donor at the centre of the QW. The wavefunction of an electron bound in the ground state of an interface donor will resemble one of the 2 lobes of a 2p-like orbital

Chapter 4

Breakdown of the quantum Hall effect

4.1 Introduction

We begin by giving a brief description of the quantum Hall effect (QHE) [48], [49], [51]. To explain the fundamental properties of the QHE we employ an edge state model. We then move on to examine the literature on the experimental observations of the breakdown of the quantum Hall effect. We note that throughout the literature there appear two commonly used models to explain the properties of QHE breakdown (QHBD). The first model is the bootstrap electron heating model proposed by Komiyama et al. [2]. In this work, which is outlined in more detail in section 4.4.1, they propose a macroscopic breakdown throughout the sample inducing a "large" increase (several orders of magnitude) in the longitudinal conductivity. This model explains most of the published experimental observations of the QHBD. However, there are a significant number of experiments where QHBD appears to occur microscopically. In such experiments, including those performed on the samples used to maintain the U.S. resistance standard at the National Institute of Standards and Technology (NIST) [50], breakdown occurs as a series of well defined steps in the longitudinal voltage V_{xx}. Such steps can be explained by quasi elastic inter-Landau level scattering (QUILLS), as proposed by Eaves et al. [18]. In section 4.4.3 we

outline this model and present an extension proposed by Martin et al. [3], which is based on impurity driven inter-Landau level scattering (IDILLS). Both the QUILLS and IDILLS models are compared to various experiments where steps are observed in QHBD. For each of the models (BSEH and QUILLS/IDILLS) we examine their strengths and weaknesses from an experimental perspective.

4.2 The quantum Hall Effect

One of the key features of the QHE is the appearance of plateaux in the Hall resistance of value

$$R_{xy} = \frac{1}{\nu}\frac{h}{e^2}, \tag{4.1}$$

where ν is an integer and the accompanying absence of the longitudinal resistance, R_{xx}. The principle features of the QHE can be described by two differing models. One considers current to flow throughout the sample wherever $R_{xx} = 0$ [51]. The other, the edge state model, considers current flow in the magnetic field region where $R_{xx} = 0$ to occur only in states close to the sample edges [52],[53]. To describe the QHBD in terms of a microscopic process we have to use the idea of edge states. Consequently, an edge state description of the QHE will be outlined in the following section.

Charged particles in a 2DEG subjected to a magnetic field, perpendicular to the plane of the 2DEG, have discrete energy levels called Landau levels. In the absence of disorder and electric field, the energies of the Landau levels are given by

$$E_{nk} = (n + \frac{1}{2})\hbar\omega_c, \tag{4.2}$$

where $\omega_c = \mid eB/m \mid$ is the cyclotron frequency, n a non-negative integer and m the effective mass of the electron. In the absence of disorder and an electric field Landau levels are degenerate. The number of states per Landau level, per unit area,

is given by $n_B = |eB/h|$ excluding spin degeneracy. In the ideal case, the Landau levels have discrete energies. However, in the case of a real sample broadening of the Landau levels occurs. Scattering due to electrons and phonons means that the electron can only survive a finite time τ_i between scattering events. Therefore, the energy can only be defined within a precision of $P = \hbar/\tau_i$, and this gives rise to broadening of the Landau level states. In addition, due to the random potential variation of impurities, the degeneracy of the Landau levels is lifted. This creates a Landau level broadening with extended states around the ideal Landau level energy and localised states between consecutive Landau level extended states, see figure 1-9. The width of the broadening due to impurities is given by Γ and is thought to be larger than P. At low fields, the Landau levels overlap, $\hbar\omega_c < \Gamma$, so the density of states is little different to that of the continuum case at $B = 0T$. At high fields, $\hbar\omega_c > \Gamma$, the Landau levels do not overlap and quantum effects can be observed. As the magnetic field is increased, the separation between Landau levels grows and so does the number of states that each level can hold. As the density of electrons stays the same in the sample, the number of filled Landau levels must change. The filling factor, ν, or number of filled Landau levels is given by $\nu = |hn_{2D}/eB|$, n_{2D} being the electron density of the 2DEG. Note that this equation does not take spin into account, so filling factor 2 corresponds to the filling of both spin states of the lowest Landau level. When the Fermi energy is between Landau levels and in the absence of disorder, there are completely full states below the Fermi energy and totally unoccupied states above.

When the Landau gauge is used, the wave function of an electron in a 2DEG subjected to a strong magnetic field B takes the form

$$\Psi = \phi_n(y - y_{k_x})e^{ik_x x}, \tag{4.3}$$

where ϕ_n is the solution of the harmonic oscillator equation and y_{k_x} the centre of the parabolic potential due to the magnetic field. Different values of the wavevector k_x, displace the centre of the parabolic potential, as discussed in chapter 1, a distance

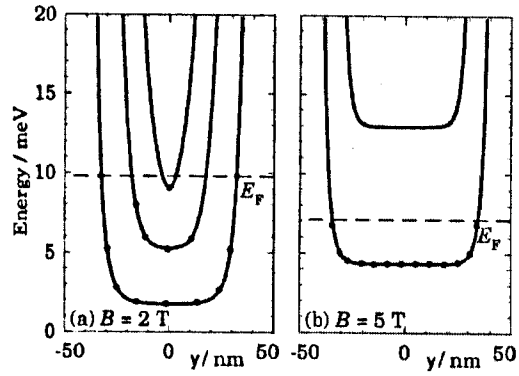

Figure 4-1: The energy distribution for a narrow sample at a) B= 2T b) B=5T to highlight the effect of the hard walled sample edge. The Fermi level is shown by the dashed line and the dots are the guiding centres x_k. [24]

$y_{k_x} = -k_x l_b^2$ from the centre of the sample where $l_b = (\hbar/eB)^{1/2}$ is the magnetic length [24]. Because energy is not dependent on k_x i.e. $d\varepsilon/dk_x = 0$, the group velocity of the electron is zero [24]. In the absence of an electric field, Equation 4.3, corresponds to a plane wave in the x direction with the electron behaving like a simple harmonic oscillator in the y direction. The magnetic field therefore confines the electrons in the y direction. However, due to the sample's finite width, electrons near the sample edge will be additionally confined by the hard wall potential of the sample edge. Increasing the magnetic field strengthens the parabolic magnetic potential and confines the electrons more tightly. For a narrow sample as shown in figure 4-1, at the sample edges the energies of the Landau levels become strongly modified due to the hard wall potential of the edges. For the cases where the orbit centre is lying outside the sample boundary, an electron at the edge finds itself trapped in a roughly triangular potential well, created by the cut-off of the parabolic potential from the magnetic field by the sample edge potential step. The energy of the state rises and its degeneracy is lost. The energy bands now have the form of figure 4-1. In the edge state model $d\varepsilon/dk \neq 0$ at the edges see figure 4-1; therefore, at the edge the electrons have a drift velocity. This corresponds to the classical idea of skipping states down the sample's edge. A consequence of the potential slopes having opposite signs on opposite sides of the sample is that the drift velocities are

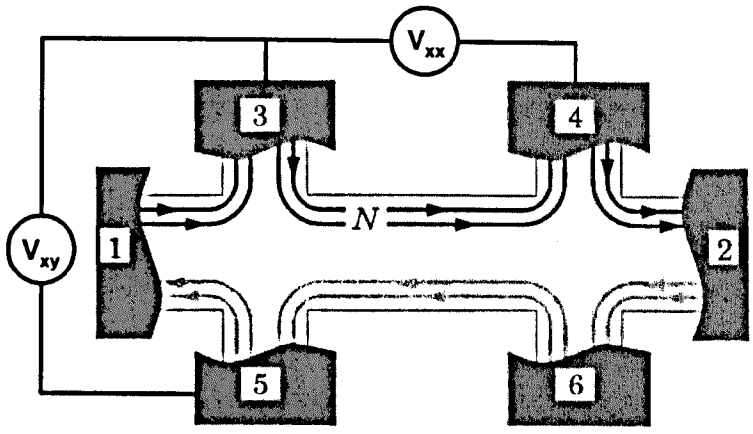

Figure 4-2: A view of the edge states and their direction taken from Davies [24] with adjustments. Current is passed between contacts 1 and 2. The Hall voltage V_{xy} is measured across the sample i.e. between contacts 3,5 and the longitidinal voltage V_{xx} is measured between contacts 3,4.

opposite in direction; the electrons on opposite edges travel in the opposite direction. Furthermore current injected at contact 1, see figure 4-2, will travel along the edge containing contacts 3 and 4 toward contact 2. Conversely, the current along the sample edge with contacts 5 and 6 travels from contact 2 to 1.

For the same geometry as figure 4-2, consider a value of the magnetic field at which the Fermi level lies in localised states, between Landau levels. This means that only the edge states lie at the Fermi level. There are N of these channels of conduction, corresponding to the number of occupied Landau levels in the centre of the sample. The states between each side of the sample are well separated and travel in opposite directions. The application of a negative bias V_1 to contact 1 creates a current flowing from contact 2 to contact 1. This raises the energy of the electrons in contact 1 by $-eV_1$ therefore injecting extra electrons into the edge states that leave the contact as shown in figure 4-2. Assuming no scattering, the edge states run across to contact 3. If contact 3 is connected to a high impedance voltmeter it can take no net current so $V_3 = V_1$. The same argument applies to contact 4 giving $V_4 = V_1$. Therefore the top edge all lies at the same potential. For the bottom edge, as there is no extra current carried by its edge states and using the argument above,

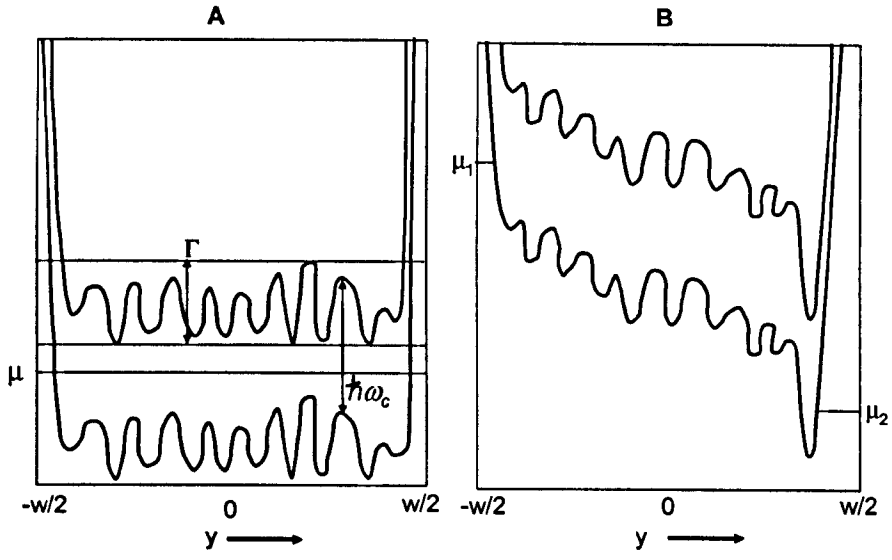

Figure 4-3: The energy variations of the n=0 and n=1 Landau levels are shown at filling factor ν=2, spin splitting is ignored. Figure A is the zero bias case. The level broadening due to impurities is given by Γ, the Landau level separation, $\hbar\omega_c$, and the chemical potential μ. Figure B shows the potential drop across the sample when a current is flowing. The chemical potentials are labelled $\mu_1$and μ_2 at the two edges. The potential variation due to impurities is included, as is the effect of the Hall electric field.

its potential is of that of contact 2, so V_2=V_5=V_6=0.

A current $-(e^2/h)V_1$ is injected into each of the top edge states. The usual factor of 2 is omitted from the normal Landauer-Büttiker formalism to treat the up and down spin split states separately. Thus the total current flowing is $I = -\nu(e^2/h)V_1$ and the Hall resistance is $(V_5 - V_3)/I = -V_1/I = (1/\nu)(e^2/h)$, a quantised value [24]. Also the longitudinal resistance $(V_4 - V_3)/I = 0$. These are the essential features of the QHE [51] in the edge state picture.

The assumption of no back-scattering turns out to be a valid one. The large separation between the edge states on different sides means that an electron scattering between them is unlikely. Scattering can occur when an skipping orbit is deviated from a straight propagation by an impurity. The electron may contour round the impurity along the equipotential or be scattered into a neighboring state. These nearby states however, propagate in the same direction the initial state. The total

current is therefore unaffected as the electron continues in the same direction. For scattering into an edge state propagating in the other direction, an electron would need to cross from one edge to the other via the bulk states and this will destroy the quantization of R_{xy}. Provided the Fermi level lies between Landau levels, the cross-sample scattering is extremely weak. Thus the quantization is quite robust.

Classically, the Hall effect for a n-type sample, is envisaged as many electrons being forced to one side of the sample due to the effect of the Lorentz force. The induced charge redistribution leads to a negative charge build up on one side of the sample. Conversely the loss of electrons effectively creates a positive charge build up on the other edge creating the Hall voltage. In a quantum description of a 2DEG, one viewpoint is to start by considering the case of a magnetic field but no current. As discussed previously, the degenerate Landau levels are created and the electrons are envisaged as having plane wave form along the sample length and have an equal spacing of states across the sample width. In the case of an integer filling factor there is an incompressible completely filled Landau level below the Fermi level and an empty Landau level above. If a current is now passed through the sample the electrons start to move along the length of the sample. Classically the Lorentz force would push electrons to one of the sample edges. However, in the quantum description of QHBD, there are no available states within the 2DEG for the electrons to move into and their spacing also remains constant. Electrons are thus forced up into the steep, dense edge states, seen in figure 4-1, on one side of the sample and down the steep edge states on the other side of the sample. On one side there is an increase in the electron density and therefore negative charge, in a very small region of the sample close to the edge. On the opposite side of the sample the movement of the electrons across the sample leads to situation where the remote positive donor charges are no longer balanced by the adjacent electrons of the 2DEG. A narrow strip of positive charge then occurs on this sample edge. We envisage this process as the magnetic field shifting the 2DEG into the depletion region of the sample. The result is thought of as two lines of opposite charge on opposing edges of the sample. These create the Hall voltage.

Figure 4-3 illustrates the effect of the disordered impurity potential on the Landau levels. The depicted variation in energy is not drawn to scale or intended to be an accurate representation. The actual broadening size Γ will depend on the sample and the exact form of the impurity induced disorder

At present there remains some doubt as to how the Hall voltage is distributed across the sample width, at least in the regime of quantum Hall effect breakdown [16], [3], [54], [55], [58]. The two main arguments are for a linear variation in potential across the sample and a logarithmic variation. For the edge state model we would expect a logarithmic variation as seen in figure 4-4. Beenakker and van Houten [52] have modified a model proposed by McDonald [53] for the variation of potential across a sample. Macdonald's model of the effect of the two equal and opposite line charges at the edges becomes divergent at the sample edges. However, by assuming a linear extrapolation to the expected Hall voltage, Beenakker and van Houten express the voltage variation with sample width as

$$V_H(y) = \frac{1}{2} I R_H \left(1 + \ln \frac{w}{\xi}\right)^{-1} \ln \left[\frac{y - w/2}{y + w/2}\right], \quad \text{if } |y| \leq \frac{w}{2} - \xi, \tag{4.4}$$

where $\xi = \nu l_b^2/\pi a^*$, $R_H = h/\nu e^2$, a^* is the Bohr radius, $a^* = 4\pi\varepsilon\hbar^2/me^2$ (ε is the dielectric constant). Note, the modulus of the logarithmic terms needs to be taken to ensure the formula gives correct results. For the region close to the sample edge $|y|=(w/2)-\xi$ the voltage V_H variation is approximated as linear to the edge value of $\pm I R_H/2$. The potential variation close to the sample edges can be considered as consisting of steps of compressible and incompressible strips [56], [57]. In the following we do not consider these steps and follow the linear assumption presented above for simplicity. The equation is therefore forced to fit to the Hall voltage measured $\pm V_H/2 = \pm I R_H/2$. The result of equation 4.4 is plotted in figure 4-4 and compared with the electro-optically determined experimental data of Fontein et al. [59]. The data of Fontein et al. shows a good correlation with the model indicating the validity of a logarithmic variation of the voltage across the sample.

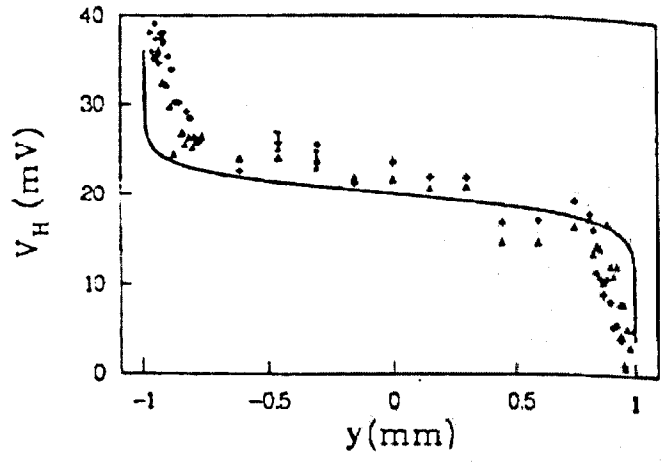

Figure 4-4: Hall potential profile measured electro-optically across a 2mm wide Hall bar, at a current of $5\mu A$. The data was taken at two points within the $\nu = 4$ plateau region. Taken from [59] with modifications.

4.3 Breakdown of the quantum Hall effect

The breakdown of the dissipationless state of the integer quantum Hall effect [51] is observed as a sharp increase in the longitudinal voltage drop V_{xx}, when the current I, flowing down the length of the Hall bar exceeds a critical value I_c. In this thesis it is the breakdown of the dissipationless region of V_{xx} that is considered as QHBD not the change in plateau height in V_{xy}. The importance of the QHBD has led to extensive research into its properties, a review of which was recently published by Nachtwei [15]. Often the QHBD dependence will be described in relation to some property such as temperature. In general, the term 'dependence' refers to the critical current I_c, and how this varies with the named property. There is still some uncertainty as to the best way to demonstrate the dependence on the critical current I_c. Some authors use J_c, the average critical current density, related to the critical current by $I_c/w = J_c$. Others prefer the average breakdown electric field E_b, as the most suitable form, $E_b = V_H/w = I_c R_{xy}(\nu)/w$, where w is the width of the sample and $R_{xy}(\nu)$ is the Hall resistance for the plateau in question. Note that when using the breakdown field the assumption is that $R_{xy}(\nu)$ is constant. Kawaji et al. [60] show that the quantum Hall resistance shows deviation from the quantised value

before the dissipation is observed in V_{xx}. However, Komiyama et al. [2] measured a difference in R_h for fields twice that of breakdown to be 1.6%. Iizuka et al. [61] also measured small deviation in R_h with $\Delta R_h/R_h = -8ppm$ so the assumption is reasonably valid. The advantage of J_c and E_b is that they make comparing between devices easier as the device width is taken into account. Finally some authors use the conductivity σ_{xx} to describe the QHBD. The conductivity $\sigma_{xx} = \rho_{xx}/(\rho_{xx}^2 + \rho_{xy}^2)$ with $\rho_{xx} = (V_{xx}/L)/(I/w)$ and $\rho_{xy} = -V_{xy}/I$, where L is the distance between probes measuring V_{xx} along the length of the sample.

4.3.1 Temperature dependence

The QHE is dependant on temperature. As the temperature is raised the critical current, I_c, or current value where the dissipationless region in V_{xx} breaks down, becomes smaller and smaller until around 30K no dissipationless region is observed [2]. The bootstrap electron heating (BSEH) model proposed Komiyama et al. [16] [2] describes the σ_{xx} dependence on temperature very well for a series of samples of mobilities in excess of $20m^2V^{-1}s^{-1}$. It is found that at low temperatures (T<4K) σ_{xx} increases in a sharp step by three orders of magnitude, see figure 4-5. The successive shrinking of the step is observed as the lattice temperature increases due to the low Hall field value of σ_{xx}, increasing in size. Eventually, σ_{xx} is almost Hall field-independent for $T > 10K$. These features were explained by the thermal activation of electrons at the Fermi level to delocalized states near the upper Landau level centre for T<4K. The rapid increase in σ_{xx} in the regime of $4K < T < 10K$ was considered to be likely due to thermal delocalisation of electron states. The electric field independence of σ_{xx}, for $T > 10K$ was due to all the states reaching a state of delocalisation. Komiyama also predicted a critical Hall field at which breakdown would occur which is said to be independent of lattice temperature [16] if $T < 5K$. The BSEH model thus provides a quantitative model for the temperature dependence these samples.

Matthews et al. looked at how the critical current varied for temperatures less than $1mK$ in samples with very high mobilities, 250 and $100m^2V^{-1}s^{-1}$, and lower

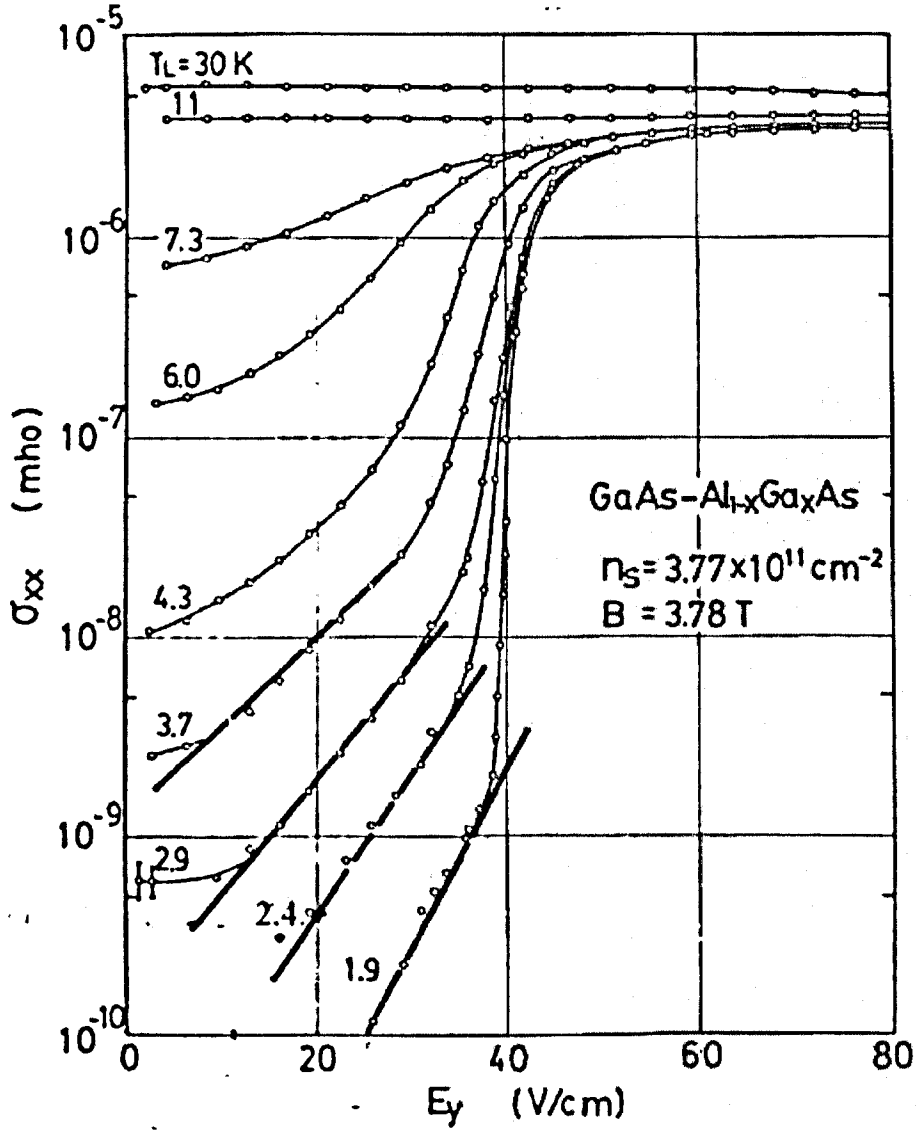

Figure 4-5: The longitudinal conductivity σ_{xx} vs the Hall field E_y taken at different temperatures by Komiyama et al. [2] at filling factor $\nu = 4$. the solid lines represent the expected σ_{xx} given by the BSEH model.

mobilities $25m^2V^{-1}s^{-1}$ using torque magnetometry [62]. Torque magnetometry is a contactless method that uses a time varying magnetic field to induce a current flow around the 2DEG. The induced current becomes large for values of the magnetic field that correspond to the plateau regions. They found that for the high mobility samples the critical current displayed an exponential reduction over the temperature range of $\sim 25-750mK$. The samples with lower mobility showed a temperature independent behavior below $300mK$ and a temperature dependence above 300mK. They explained their findings using the QUILLS model [18]. In the QUILLS model momentum is conserved during a tunneling process by either impurity or phonon scattering. Very high mobility samples will have a very low probability of impurity scattering and due to the low temperatures the scattering due to phonons will be small as well. Any increase in temperature will increase the phonon density and consequently increase the probability of inter-Landau level tunneling by phonon scattering. Lower mobility samples have a higher probability of impurity scattering. Hence, at lower temperatures the role of phonons will not be significant. For temperatures above $300mK$ the role of phonon scattering becomes dominant over impurity scattering and a temperature dependence becomes evident. This analysis in terms of QUILLS by Matthews [62] is qualitative only.

A careful study of the characteristics of QHBD in samples of mobility between $3-22m^2V^{-1}s^{-1}$ was carried out by Rigal et al. [63]. They found that below a certain temperature ($T < 1K$) the critical current I_c, remained almost constant at a value dependant on filling factor. For temperatures $T > 1K$ the critical current dropped rapidly with temperature for all filling factors. They obtained a good correlation between their data and the Gorter-Casimer two fluid superconductivity model. The variation of plateau width with temperature was also investigated. Again the superconductivity model could be applied to the data, except this time there was what was termed a low temperature and high temperature phase. It was found necessary that the plateau width dependence for T<1.3K be termed the low T phase with the critical temperature (point where the plateau width goes to zero) being identical for all filling factors. In the high temperature phase only the high index filling factors

achieved the phenomenological match between the two-fluid model and data, with filling factor two showing a large difference in shape and value from the theory. The difference was explained by looking at the melting points of 2D superconducting phase behavior.

The almost constant I_c in torque magnetometry for $T < 1K$ could be explained in terms of QUILLS as described by Matthews et al. [62]. However, the phenomenological superconductivity relation shows an impressive correlation with the data. The drop in I_c from $68\mu A$ at a few mK to $45\mu A$ at $T = 4K$ would correspond to a change in the mean breakdown field from 34 to $22.5 Vcm^{-1}$ assuming that the Hall voltage remains at or at least close to its plateau value. Such a change is unexplained by the BSEH model. However, the constant breakdown current for T<1K could be explained by BSEH in terms of the independence of the critical field on lattice temperature. The different behavior found in the various experiments on QHBD, may also be due to different criteria for the breakdown employed by the different research groups. For example, Rigal et al. used the point where the measured dissipative voltage between the probes reached $50\mu V$, Komiyama et al. defined a critical field where the steep onset of dissipation occurred.

A change in sample behavior was noticed by Sanuki et al. [64] between 0.5K and 4.2K. At 0.5K, step-like features were observed with hysteresis. These were, however, not present at higher temperatures [64] or after illumination. The samples also showed a sublinear dependence of I_c on the sample width for temperatures in the region of 4.2K and yet a linear I_c dependence on width for T=0.5K. Strangely, the opposite dependence on width was observed after illumination for each temperature. The disappearance of features above T=0.9K or with illumination was also noted by Eaves et al. [65] for a hole gas sample. Sanuki et al. explained the difference by saying that at higher temperatures the thermal broadening was larger than the fluctuations due to the random impurity potentials in the Landau level. Therefore, the effects of the random impurity potentials are negated in the high temperature region.

4.3.2 Magnetic field dependence

The general result of increasing the magnetic field or decreasing the filling factor, is that the critical current will increase as the filling factor decreases. Several authors report that the critical current varies with the magnetic field according to the relation $I_c \propto B^{\frac{3}{2}}$ [66], [67], [16], [68], [69]. Note should be made that the dependence refers to the critical current maximum for each plateau region. Also the samples used in these studies are of the butterfly design. In this design large areas of sample are used for the current injection which are linearly narrowed to the specified width. The specified width is a rectangular region where the voltage probes are situated. These samples are designed to ensure that the hot spots due to the current injection do not drive the breakdown of the QHE. Generally, the explanation of the I$\propto B^{3/2}$, dependence is that there is an inter Landau level tunneling process present in QHBD, though the precise mechanism remains unexplained so far. Komiyama and Kawaguchi, can also explain the $I_c \propto B^{\frac{3}{2}}$ dependence, by using a linear relation where the scattering time of excited electrons is also dependent on the magnetic field. Rigal et al. [63] interpreted their results in terms of a phenomenological similarity to the Gorter-Casimir model for superconductivity. Bliek et al. [70] investigated the critical current dependence close to integer filling factors. They found that as the integer filling factor was approached I_c increased linearly to a peak value. Approaching the integer filling factor from both sides depicted a triangular behavior with the peak on the integer filling factor. Similar dependences of the critical current close to integer filling factors were observed by Iizuka [61] and Boella [71]. Although the relations could be found easily from the data, a model for the triangular behavior was not proposed. Komiyama and Kawaguchi have proposed a explanation for this dependence in terms of BSEH.

4.3.3 Width dependence

The dependence of the QHBD on device width has attracted interest as it gives clues to the nature of the potential profile across the Hall bar and so the nature of the breakdown process. If the sample has a linear potential drop across the sample

width, a linear width dependence would be expected. If the potential drop across the sample is non-linear, then a sub-linear dependence would be expected. Both linear and sub-linear dependencies on I_c with sample width are observed. The linear dependence is observed by Kawaji et al. [66], [72], Boisen et al. [73] and Kawaguchi et al. [74] for low mobility samples. Song and Omling observed linear behaviour for samples with high and low mobilities [75]. Balaban et al. [78] and Haug et al. [79] found a sub-linear dependence for high mobility samples which Balaban explained in terms of QUILLS. Both sub-linear and linear behavior with width were found depending on temperature and illumination by Sanuki et al. [64].

4.3.4 Length dependence

The breakdown of the QHE shows a surprising dependence on the length of the sample. That the QHE effect should depend on length is not obvious from the basic understanding of the QHE outlined in section 4.2. However, a phenomenological length dependence is observed by several authors [87], [77], [86]. Although experiments by Morita et al. [80] found that the effect was small in samples of width $20\mu m$ and $100\mu m$. Kawaguchi et al [87] found that short samples inhibited the development of QHBD and suggested that a length of $100\mu m$ would be needed for BSEH to be observed. For samples of length less than $100\mu m$ current densities for breakdown were recorded as high as $10Am^{-1}$ for the $20\mu m$ wide sample [74] (from our simple analysis of their results). Komiyama et al. found that for samples with contacts very near the start of the rectangular region for butterfly samples, the I(V) characteristics were asymmetric with respect to current direction. If the electrons had travelled the length of the Hall bar upon reaching the contact, then breakdown occurred at roughly $3\mu A$. However, for the case where the electrons entered the rectangular region near the contacts there was still no breakdown for current up to $8\mu A$. The result of Kawaguchi et al. was independent of sample width and magnetic field direction. The length then needed for breakdown was $130\mu m$ with some values suggested for $\nu = 4$ and 6 being $20\mu m$ and $10\mu m$ respectively. Lower mobility devices showed smaller lengths needed for breakdown. These results are very easily explained by the

avalanche mechanism of BSEH and very hard to explain by some local field model such as QUILLS. A different approach was used by Sagol et al. [77] by using pulses of differing voltage and length into different samples. They found some critical pulse width needed for breakdown that varied with magnetic field and pulse amplitude. Applying a simple drift velocity model they calculated some critical lengths of the order of $1-25\mu m$. Sagol explained the magnetic field dependence and amplitude dependence using an impurity-driven inter-Landau level tunneling model. Kaya et al. [88] measured the relaxation length of electrons excited into the upper Landau level and found that a significant length was needed to achieve relaxation that depended on the sample mobility.

4.3.5 Step-like breakdown

Features have been reported in V_{xx} when sweeping the magnetic field at constant current. As many as 35 different dissipative states have been found in one plateau region [29]. In measurements using the U.S. QHE resistance standard sample, Cage et al. found steps in the low field side of the $\nu = 2$ plateau [81],[50],[29]. The steps were found when sweeping the magnetic field from low to high. The step size was approximately $5mV$, but varied slightly with the magnetic field see figure 4-6. It was found that the presence of steps was reproducible but the position in magnetic field and current were not reproducible for different B-field sweeps. The current direction caused the step-like breakdown trace in $V_{xx}(B)$ to take a different path, dependent on polarity, the positive current direction having lower amounts of dissipation. Time resolved measurements showed switching behavior between as many as 35 different states with a separation in voltage of $5mV$. The sample showed hysteresis on sweeping magnetic field when sweeping from high to low in the $\nu = 2$ plateau region with no step-like behavior and a sharp jump into dissipation at the left hand end of the plateau region.

Eaves et al. also observed the presence of steps in V_{xx} in a hole gas sample in the $\nu = 1, 2$ plateaus [65]. The steps were reproducibly of height $1mV$, though the positions in magnetic field and current for different B-field sweeps varied. The steps

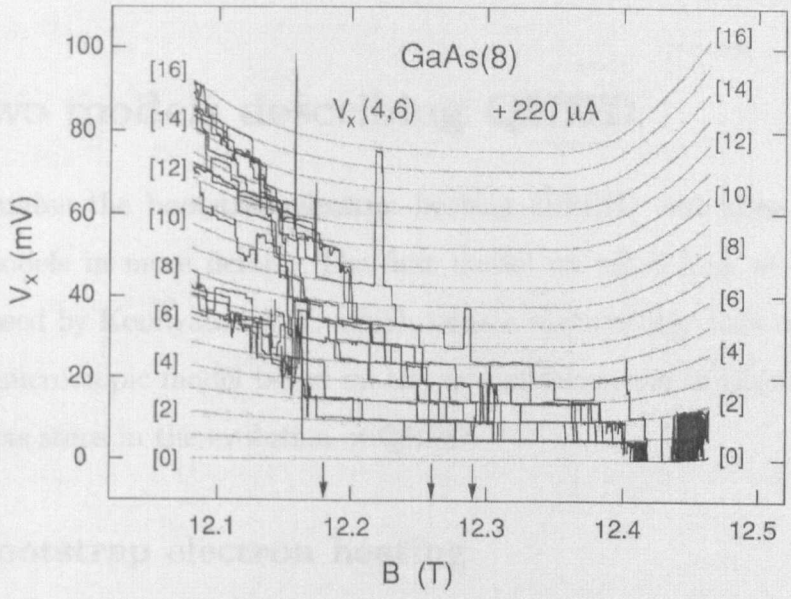

Figure 4-6: Fourteen sweeps of V_{xx} versus B for one of Cage's samples. The step like nature of the breakdown is clearly visible. [82]

observed in the $\nu = 1$ plateau showed the same kind of hysteresis in magnetic field observed by Cage et al., steps occurred in the low field side of the plateau with B going from low to high. On the sweep of B from high to low no features were seen.

A poorly resolved series of steps was observed by Bliek et al. [70] along with high critical current density $J_c = 30Am^{-1}$ for a sample where the current flowed through a $1\mu m$ constriction. Mokerov et al. found 3 steps of height 5, 10 and 20mV in the I(V) characteristics of a standard Hall bar sample [83]. Large multiple steps $V_{xx} = 10 - 50mV$ were observed in the high field side of $\nu = 2$ for a standard GaAs/(AlGa)As heterostructure by Boella et al. [71]. In addition, many authors observed a switching behavior of V_{xx}, at a constant current, in time resolved measurements. Cage et al. observed the most states (35) with most other authors finding two states [83] [84]. Boella et al. [71] found three states that the electron system switched between; the third state was only visited when the system was relaxing from a higher dissipation level of V_{xx}. It was observed that the higher the current the more time was spent by the system in a higher dissipative state until the system no longer returned to the

non dissipative state.

4.4 Two models describing QHBD

We now examine the bootstrap electron heating (BSEH) and inter-Landau level tunneling models in more detail. The first model we sHall look at is the BSEH model proposed by Komiyama et al. which takes a macroscopic view on QHBD, the second is a microscopic model based on the rate of formation of electron-hole pairs which predicts steps in the evolution of QHBD.

4.4.1 Bootstrap electron heating

First the BSEH model is considered. In a strong magnetic field the longitudinal electric field E_x is much smaller than the transverse or Hall field E_y. This in turn leads to an expression for the gain of an electron due to the electric field given by

$$G = \mathbf{j}.\mathbf{E} \text{ and} \tag{4.5}$$

$$G \simeq \sigma_{xx} E_y^2, \tag{4.6}$$

where σ_{xx} is the longitudinal conductivity. For the case of the QHE, σ_{xx} is vanishingly small in the limit of low temperature. However, at breakdown σ_{xx} increases by several orders of magnitude showing dissipation which indicates the presence of electron heating [16], see figure 4-5. Normally σ_{xx} is a function of the electric field. However, it also depends on the electron energy distribution which can be characterized by an effective electron temperature $T_e(x, y)$, as the electron temperature is dependant on how the electrons arrive at a position (x, y) and not just the value of $E_y(x, y)$. Thus σ_{xx} can be said to be influenced by two independent variables and it follows that

$$\sigma_{xx}(x, y) = \sigma_{xx}[E_y(x, y), T_e(x, y)]. \tag{4.7}$$

To illustrate BSEH in the most simple case, we will choose the lattice temperature to be $T_L = 0K$. The existence of the QHE means that for small T_e we find $\sigma_{xx}(T_e, E_y)$

is vanishingly small for low values of E_y. As T_e is raised the electrons will be excited into the higher unoccupied Landau level, this means that $\sigma_{xx}(T_e, E_y)$ will increase. The exact relationship between σ_{xx} and T_e is not important in this model, only the idea that the greater the value of T_e then the greater the number of electrons that are excited into the higher unoccupied Landau level.

Now we consider the rate L, at which the electron system loses energy to the lattice. The loss rate will be a function of E_y and T_e. It is obvious that for $T_e = 0K$ the loss rate $L(E_y, T_e) = 0$ and that an increase in T_e, for a fixed E_y, will cause L to increase. The precise evolution of this dependence is again considered unimportant in this model, only the general trend needs to be considered. For a given E_y the electron system adjusts so that the gain rate equals the loss rate,

$$G(E_y, T_e) = L(E_y, T_e). \tag{4.8}$$

In BSEH it is assumed that E_y does not locally affect σ_{xx} or L which leads to the following,

$$\sigma_{xx}(E_y, T_e) = \sigma_{xx}(0, T_e) = \sigma_{xx}(T_e) \tag{4.9}$$

and

$$L(E_y, T_e) = L(0, T_e) = L(T_e). \tag{4.10}$$

It follows from equations 4.6, 4.9 and 4.10 that for any value of E_y if $T_e = 0$, then the balance in equation 4.8 will always be true, which is the case of the integer QHE. To achieve a physically obtainable stable state, a real system will need to have some restoring force to balance out any small fluctuations in the electron system. The stability condition is

$$\delta G/\delta T_e < \delta L/\delta T_e. \tag{4.11}$$

We now have a case in which a few electrons can be excited into the upper Landau level. As long as the induced change in gain ΔG of these non-equilibrium carriers is less than the induced loss ΔL then the system will remain stable against fluctuation. If, however, $\Delta G > \Delta L$ then the system will runaway from the dissipationless state and will continue doing so until a state can be found where equations 4.8 and 4.11 are satisfied again.

Considering these expressions for G and L it is apparent that while L is independent of the applied field E_y, G on the other hand varies with a E_y^2 dependence as shown in equation 4.6. If we take the low temperature limit $T_e = 0K$ for some small temperature variation δT_e with increasing field there will be a point where the gain due to the E_y^2 dependence will be equal in size to the loss rate which remains static in value with increasing E_y. This critical condition

$$(\delta G/\delta T_e)_{T_e=0} = (\delta L/\delta T_e)_{T_e=0} \tag{4.12}$$

will be reached when $E_y = E_b$, where E_b is the critical breakdown field. When E_y becomes larger than E_b the system undergoes a transition to a dissipative state and the longitudinal conductivity σ_{xx} will increase discontinuously to a finite value. The electron heating arising from this process is called bootstrap electron heating. The only parameter assumed in this model of breakdown is the smooth vanishing of $\sigma_{xx}(T_e)$ and $L(T_e)$ in the limit of low temperature $T_e = 0K$. Consequently, BSEH has the possibility of being a reasonable and general prediction of QHBD.

Using BSEH it is possible to predict the field, E_b, at which breakdown occurs. By identifying the predicted breakdown field, any experimental system undergoing QHBD can be compared with its calculated E_b and we can therefore judge the validity of the BSEH model.

In the following, it is implicitly assumed that E_y is constant over macroscopic length scales across the Hall conductor. This statement can be understood by simple argument. It is well known that in the low current regime E_y is concentrated in the

edges of the sample [53]. Any increase in the current will therefore significantly affect these edges first and dissipation will occur at these points. The current will then redistribute itself to avoid these dissipative areas and move into the more central regions of the sample until the field will be uniformly spread across the full width of the sample. Thus breakdown will occur when there are no more dissipationless current paths available and the field is evenly distributed across the sample.

To illustrate the derivation of E_b we will consider a simple case which is shown to be indicative of more realistic conditions [16]. For the case of even filling factors for the integer QHE it has been shown that $\sigma_{xx}(T)$ can be reasonably approximated for a range of T by the thermal activation energy

$$\sigma_{xx}^{ac}(T) = \sigma_{xx}^{c} \exp(-\frac{\hbar\omega_c}{2k_B T}), \tag{4.13}$$

where $\sigma_{xx}^{c} = e^2/h$, $\hbar\omega_c$ is the Landau level spacing and k_B is the Boltzman constant. Equation 4.13 can be placed into the gain rate equation 4.6 with T replaced by T_e. The energy loss rate is given by

$$L = \frac{z(T_e) - z(T_L)}{\tau_e}, \tag{4.14}$$

where τ_e is the energy relaxation time over which the electron's energy is released back to the lattice, which is estimated to be around $1\text{ns}/B(T)$ [16] and $z(T)$ is the internal energy of the system which is given by

$$z(T) = 2\int_{\varepsilon_f}^{\infty} (\varepsilon - \varepsilon_f) D(\varepsilon) F(\varepsilon) d\varepsilon, \tag{4.15}$$

where $D(\varepsilon)$ is the density of states function and $F(\varepsilon)$ is the fermi distribution. We consider the case of the integer QHE for even values v and for simplicity set $T_L = 0$ with the Landau levels being infinitely high delta function density of states. Then from equations 4.6, 4.12, 4.13 and 4.15 we can derive an expression for the critical

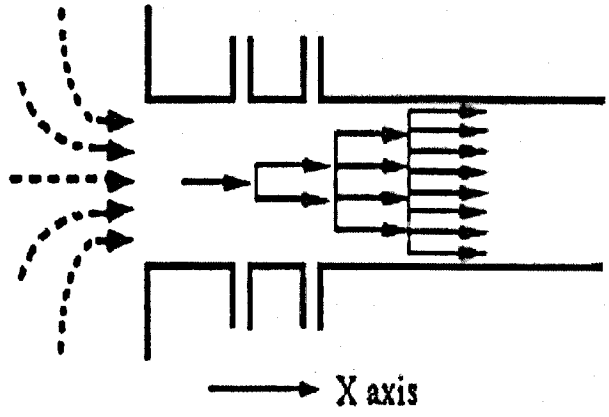

Figure 4-7: The cold electron injection into a 2DEG channel is shown. The arrows indicate the expected avalanche type multiplication of electrons and holes. [16]

field

$$E_b = \sqrt{\frac{2\hbar}{m\tau_e}}B, \tag{4.16}$$

which is independent of filling factor and electron mobility. Factors such as a finite lattice temperature and broadened Landau levels have been shown to have only a small effect on the prediction of the breakdown field E_b [16]. Consequently, equation 4.16 can be compared with experimental data without too strong a concern about over-simplification affecting its validity.

The model of BSEH is therefore as follows: small random fluctuations cause a small number of non-equilibrium carriers to be excited into the upper Landau level. The Hall current and the excited electrons move in the x direction. The Hall field accelerates these carriers and the gain in energy, for small values of E_y, is compensated by acoustic phonon emission and the hot electrons cool and drop back into the lower Landau level. These fluctuations are small when considered on the global sample scale and so the QHE shows a dissipationless state in the limit of low temperature and E_y. When $E_y \geq E_b$ the small number of non-equilibrium carriers gain more energy than they can transfer back to the lattice through acoustic

phonon emission. In this case the excited electrons keep increasing their kinetic energy indefinitely. However, the excited electrons will eventually reach the higher energy edge of the Landau level where the energy gap prevents entry into a higher Landau level. In a real system before the excited electron reaches the upper energy boundary of the Landau level it is thought to collide with a cold electron in the lower Landau level, thereby exciting the cold electron into the $(n+1)$ Landau level through electron interaction. This process is termed impact ionization and is analogous to an Auger process. The newly excited electron then begins the process of energy gain followed by impact ionization again and an avalanche type effect occurs, see figure 4-7. Thus the energy gained by the small number of initial excited carriers is distributed back into the sea of cold electrons in the nth Landau level contributing to a heating of the electron system as a whole.

4.4.2 Comparing BSEH with experiment

The following section explains some of the observed experimental results of the QHBD in terms of the BSEH model. The linear dependence of the breakdown current with the sample width [85],[74], [73] is an expected result of BSEH as the field is said to scale linearly across the sample width. It is considered that the breakdown field, $E_y = V_H/w$ where $V_H = Ih/\nu e^2$, w the sample width and ν the filling factor, that is the important factor in BSEH and not the current. As $E_y = V_H/w$ for a fixed value of E_y any increase in w must be matched by an identical increase in V_H. An increase in sample width would therefore necessitate a larger current to achieve E_b at a constant magnetic field.

Low breakdown fields with respect to those of a tunneling model are expected with the BSEH model. Typically for BSEH a breakdown field of $E_b = 4000Vm^{-1}$ for $\nu = 4$ is measured for the plateau centre, see figure 4-5. Many authors [2], [73],[63],[64],[71],[78] and [50] report critical current densities of equal to or less than $\backsim 1Am^{-1}$. Using a critical current density of $1\mathrm{Am}^{-1}$ and assuming that the electric field is uniform across the sample, we can estimate a common critical electric

field. We use the following simple calculation $E_b = V_H/w = I/w \times (h/\nu e^2)$, giving a breakdown Hall field for $\nu = 4$ of 6480Vm^{-1}. The BSEH model is often used to describe the results that show critical current densities of 1Am^{-1} or less. The predicted breakdown field of the data in figure 4-5 using equation 4.16 is 7048Vm^{-1}. Almost double the value measured. However, the microscopic models predict even higher breakdown fields and we therefore use these low breakdown field values to support BSEH.

The avalanche model requires a considerable length, $> 100\mu m$, for breakdown to occur as observed by Komiyama et al. [86] Sagol et al. [77] and Kawaguchi et al. [87]. This is one of the key features of the BSEH model. A length dependence is inexplicable using a microscopic model and indicates that a macroscopic viewpoint is needed to understand QHBD.

Using some approximations and assumptions, the BSEH model can also explain some of the observed features of QHBD. These include the triangular dependence of I_c [70],[61] and [71] for magnetic fields close to integer filling factors provided a constant background states is assumed [16]. Further, if the scattering relaxation time τ_e is said to depend on the magnetic field then the BSEH can be used to explain the $E_b \propto B^{3/2}$ dependence [66],[67],[16] and [68].

The BSEH model can also explain small hysteresis and switching. In the region of E_b there is the possibility of three points of intersection between the function due to the loss of the electrons energy back to the lattice and the changing function $\sigma_{xx}E_y^2$, which is the gain of energy of the electron in the Hall field. Consequently, there is a narrow region of electric field where there exists three possible states for the electrons which it can switch between. These three regions are 1) The dissipationless state, 2) a temporary intermediate state and 3) the final state of dissipation observed in real samples. This three-valued relation is described by an s-like dependence of σ_{xx} with E_y. Therefore the presence of bi-stable switching has a limited explanation in the framework of BSEH. The step-like behavior observed by Cage [50], Eaves [65], Bliek [70] and Boella [71] are unexplainable by the BSEH model.

4.4.3 A microscopic model for the breakdown of the quantum Hall effect

Whilst a single large step is a commonly observed mode of QHBD, there have been several reports of step-like structure in V_{xx} whilst sweeping the magnetic field [65], [70],[71] and [50]. The results obtained by Cage et al. at NIST show steps of the order 5mV with as many as 20 individual steps. These small steps are clearly different to the step predicted by the BSEH model which suggests just one step corresponding to roughly three orders of magnitude change in σ_{xx}. It seems reasonable to suppose the observed step-like breakdown has a quantum and local nature.

A quasi-elastic inter-Landau level tunneling (QUILLS) process was proposed by Eaves et al. [18] to describe the results of Balaban et al. [78]. Recently this model has been superceded by an impurity scattering model of Martin et al. [3] which looks at the dispersion of an electron hole pair [90], [91], [92]. We include the QUILLS model as a background to the model of Martin et al. and also because it can be used to predict a critical electric field for inter-Landau level scattering. The QUILLS process requires spatial overlap between the highest filled Landau level $\varphi_n(y - y_0)$ and the empty state of the next Landau level $\varphi_{n+1}(y - y_0')$ where φ_n corresponds to the simple harmonic oscillator part of the electron in a magnetic field see equation 4.3. The spatial extent of the oscillator wave function is chosen to be given by the classical amplitude $A_n = (2n+1)^{1/2} l_b$. At critical electric field E_c, overlap of the wavefunctions in the nth and n+1 Landau levels occurs $A_n + A_{n+1} = y_0 - y_0'$ see figure 4-8. Applying the condition for the states to have the same energy $eE_c(y_0 - y_0') = \hbar\omega_c$ gives the following expression for the critical electric field:

$$E_b = \frac{\hbar\omega_c}{el_b[(2n+1)^{1/2} + (2n+3)^{1/2}]}, \tag{4.17}$$

where n=0 for the $\nu = 2$ plateau. The inter-Landau level scattering in QUILLS is said to occur by emission of acoustic phonons. The energy of the emitted phonon $\varepsilon_p = \hbar v_s q_y = \hbar v_s / l_b \ll \hbar\omega_c$ where v_s is the sound velocity, q_y the momentum change given by the overlap condition to be $q_y = (y_0' - y_0)/l_b^2 = 1/l_b$ is much less than that

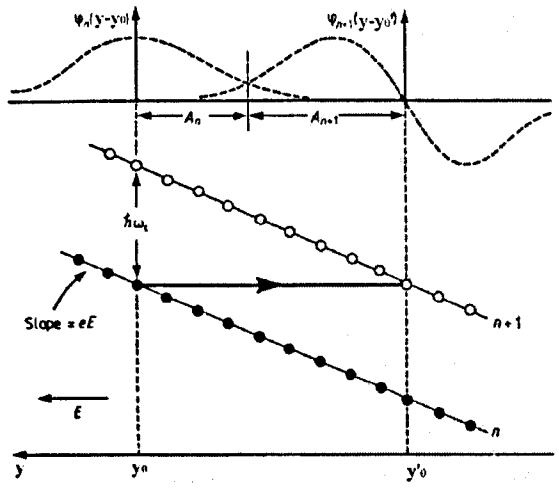

Figure 4-8: The condition for quasi-elastic scattering from filled Landau level n to empty level n+1 and spatial overlap between the oscillator eigenfunctions. The wavefunctions shown correspond to the two lowest Landau levels. Taken with adjustments from Eaves and Sheard [18].

of the Landau level separation and hence the process is considered quasi-elastic.

Recently Martin et al. [3] refined the above model further by considering the dispersion curve of an electron-hole pair and taking into account the rate of electron-hole pair generation by an impurity whose locally high electric field excites them. The starting point for the calculation of Martin et al. is Fermi's golden rule which is used to evaluate the generation rate of electron-hole pairs, in the Landau gauge, due to a single charged impurity in a uniform electric field. This gives

$$\begin{aligned} W &= 2\sum_{k_z k_X} W_{n,(n+1)} \\ &= 2\sum_{k_z k_X} \frac{2\pi}{\hbar}\delta(\varepsilon_n - \varepsilon_{(n+1)}) \\ &\quad \times \Big| \int_r d^3r |\Xi(z)|^2 \phi_n(r_\perp, k_z)\phi_{(n+1)}(r_\perp, k_X)V(r)\Big|^2, \end{aligned} \tag{4.18}$$

where $V(r)$ is the impurity Coulomb potential, $\phi_{(n+1)}(r_\perp, k_X)$ is the electronic eigenfunction in the xy plane and $\Xi_0(z)$ is the envelope function of the first electronic sub-band. The model assumes that the lower Landau levels are filled and the upper

Landau levels are empty. Such a case is in effect when the system is at an integer filling factor. A filled Landau level is incompressible and thus it is stated that there is no static screening of the impurity charge. To calculate the transition rate out of the (n, k_x) state we sum over k_X which gives the following condition

$$\Delta\varepsilon = \hbar\omega_c + \frac{e^2}{4\pi\kappa l_b}\Delta_{n,(n+1)}[k_X - k_x] - eE_y l_b^2(k_X - k_x) = 0, \qquad (4.19)$$

where ω_c is the cyclotron frequency, l_b is the magnetic length, κ is the dielectric constant, $\hbar(k_X - k_x)$ is the momentum change and $\Delta_{n,(n+1)}(k_X - k_x)$ includes the local and exchange field corrections for an exciton from (n,k_x) to $(n+1, k_X)$. The condition in equation 4.19 applies to the case where the electrostatic energy $eE_y l_b^2(k_X - k_x)$ is equivalent to the interaction energy $\hbar\omega_c + \frac{e^2}{4\pi\kappa l_b}\Delta_{n,(n+1)}(k_X - k_x)$, see figure 4-9. At the crossing point where the electrostatic energy cancels with the interaction energy, energy is conserved in moving an electron from the lower filled Landau level to the empty upper Landau level i.e. creating a magneto-exciton. This condition is an improvement upon the QUILLS model for breakdown where exchange and Coulomb interactions were neglected. For a given electric field, it is therefore possible to calculate, using equations 4.18 and 4.19, the rate of electron-hole pair generation from a single charged impurity.

The problem of defining the electric field throughout the sample is complicated because of a number of factors. These include the positioning of the impurities perpendicular to the plane of the 2DEG, how well the impurity is screened by the 2DEG and the local density of states. Suffice it to say that for the purpose of this model we only need consider that at some point within the sample the local electric field E_y is strong enough to create electron-hole pairs at a given rate, due to scattering from a charged impurity. Consider an electron-hole pair created close to an impurity, it will drift down the Hall bar at a velocity E_y/B, and for a constant generation rate a stream of electron-hole pairs will move along the sample. The electron is in the empty upper Landau level (n+1) and the hole lies in the lower full Landau level n. The further the electron-hole pair moves away from the charged impurity the greater

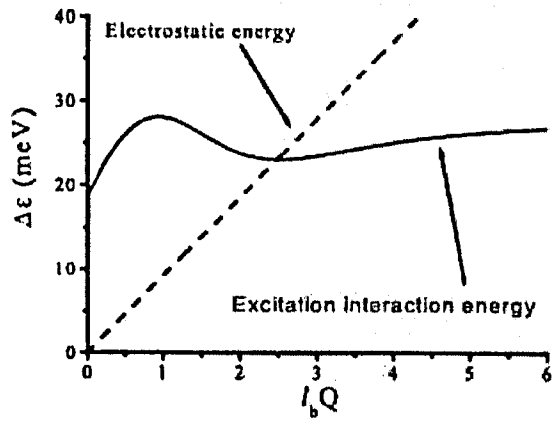

Figure 4-9: The magneto-exciton mode energy (solid line) for excitions from n=0 to n=1 with the Hall electric field at zero. The dashed line is the electrostatic energy $eE_y l_b^2 Q$ where Q is the momentum change, B=12.3T and $E_y = 1.5\text{x}10^6 Vm^{-1}$. Taken from Martin et al. [3]

the spacing between the electron and the hole becomes. This increase in separation is due to the electron relaxing its energy, via acoustic phonon emission. This effect is shown schematically in figure 4-11. Assuming that eventually, all the pairs will ionise through acoustic phonon emission, due to the fact that there are no empty states into which the excited electron can relax. The dissipative current is $i = eW$, where W is the generation rate of electron-hole pairs from the charged impurity. The dissipative current then flows across the Hall voltage equipotentials. At filling factor 2 this gives rise to a dissipative voltage

$$V_{xx} = \left(\frac{\hbar W}{2e}\right). \tag{4.20}$$

Hence, from calculating W for a fixed electric field, we can calculate the dissipative voltage along the sample V_{xx} due to scattering from a single charged impurity. This is done by evaluating equation 4.18 with the condition given by equation 4.18. Doing this for the experimental results of Cage et al. [50] Martin et al. found the results given in figure 4-10. The rate W and consequently V_{xx} reaches a maximum of $V_{xx} = 5.6mV$, when the electron-hole pairs are formed close to the roton minimum of

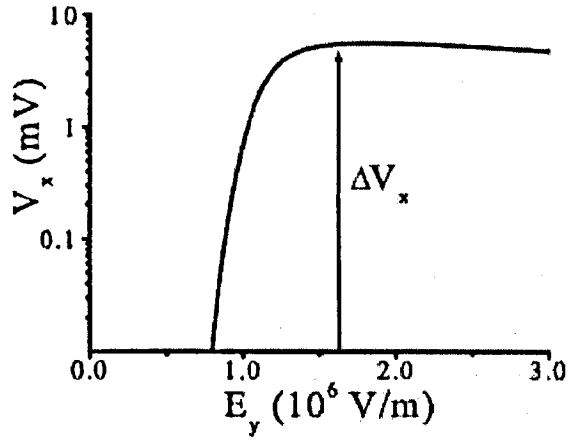

Figure 4-10: The dissipative voltage, for an elecron gas sample, as a functon of E_y. The parameters used are those found in the experiments of Cage [29]. Taken from Martin et al. [3]

the magneto-exciton dispersion curve. Equation 4.18 shows that the rate of electron-hole pair generation via a charged impurity is strongly related to the overlap between the states in the lower Landau level and those in the upper Landau level. An increase of the Hall field will cause the overlap between the states in the upper and lower Landau levels to increase. At a critical field, the generation rate significantly increases and V_{xx} will increase from a very small value given by σ_{xx} to its maximum value. For a given E_y for which the rate of production of electron-hole pairs is finite, the pairs formed at breakdown point will relax, i.e. electrons in the upper Landau level relax their energy by moving to one side of the Hall bar, whilst holes move in the opposite direction. This process tends to screen the Hall field in the central region of the Hall bar. Since the Hall voltage in experiments remains constant at its quantised value over the magnetic field range over which the dissipative steps occur, this screening effect tends to enhance the electric field at the breakdown point. Thus, as the critical electric field is reached, the generation rate of the electron-hole pairs increases rapidly, inducing a further increase in E_y, due to screening of the Hall field in other regions of the Hall bar. Thus one would expect for breakdown at a single charged impurity the system to switch between two stable states corresponding to

$V_{xx} \simeq 0$ and $V_{xx} = 5.6mV$, which corresponds to the maximum value of V_{xx} in figure 4-10.

4.4.4 Comparing the inter-Landau level scattering model with experiment

The NIST group observed a series of steps of up to 20 in number. These steps can be explained by many impurities, each providing a single electron-hole pair stream. Each step thus corresponds to individual impurities reaching their own individual critical electric field. Comparing the predicted step height with experiment provides a good quantitative agreement. The NIST group observed step heights of $V_{xx} \approx 5mV$ for $\nu = 2$ at $12.3T$ Cage [50], [29] comparing well to the predicted height of $V_{xx} = 5.6mV$. Eaves et al [65] observed step like features in the breakdown of a hole gas sample of $V_{xx} \approx 1mV$ in height and the predicted step height for the experimental conditions is $V_{xx} = 1.6mV$. The model for step like breakdown does therefore explain the origin of the observed steps and can qualitatively predict the height of these steps.

The QUILLS model can be used to roughly estimate the size of the field needed for inter-Landau level transitions. For $\nu = 2$ the Hall field needed for states in adjacent Landau levels to fulfill the QUILLS condition is

$$E_c \approx \frac{\hbar\omega_c}{fel_b} \approx \frac{1}{f}\left(\frac{\hbar\omega_c}{m_e}\right)^{1/2} B, \tag{4.21}$$

where $f \approx 3$ is a numerical factor and $l_b^2 = \hbar/eB$. The size of the electric field induced by the impurity is unknown so an exact prediction of the Hall field needed for breakdown is unrealisable. However, comparing equation 4.21 with equation 4.16 shows that the QUILLS model equates to a higher local breakdown field compared to that of predicted by BSEH for a global breakdown field. It is worth mentioning that both equations display a dependence like $a(\hbar f/m_e)^{1/2}B$ where a is a numerical constant and f is a frequency. Komiyama has a constant $a = 2^{1/2}$ whereas Eaves estimates this to be around $a = 1/3$. The large difference in the predictions of

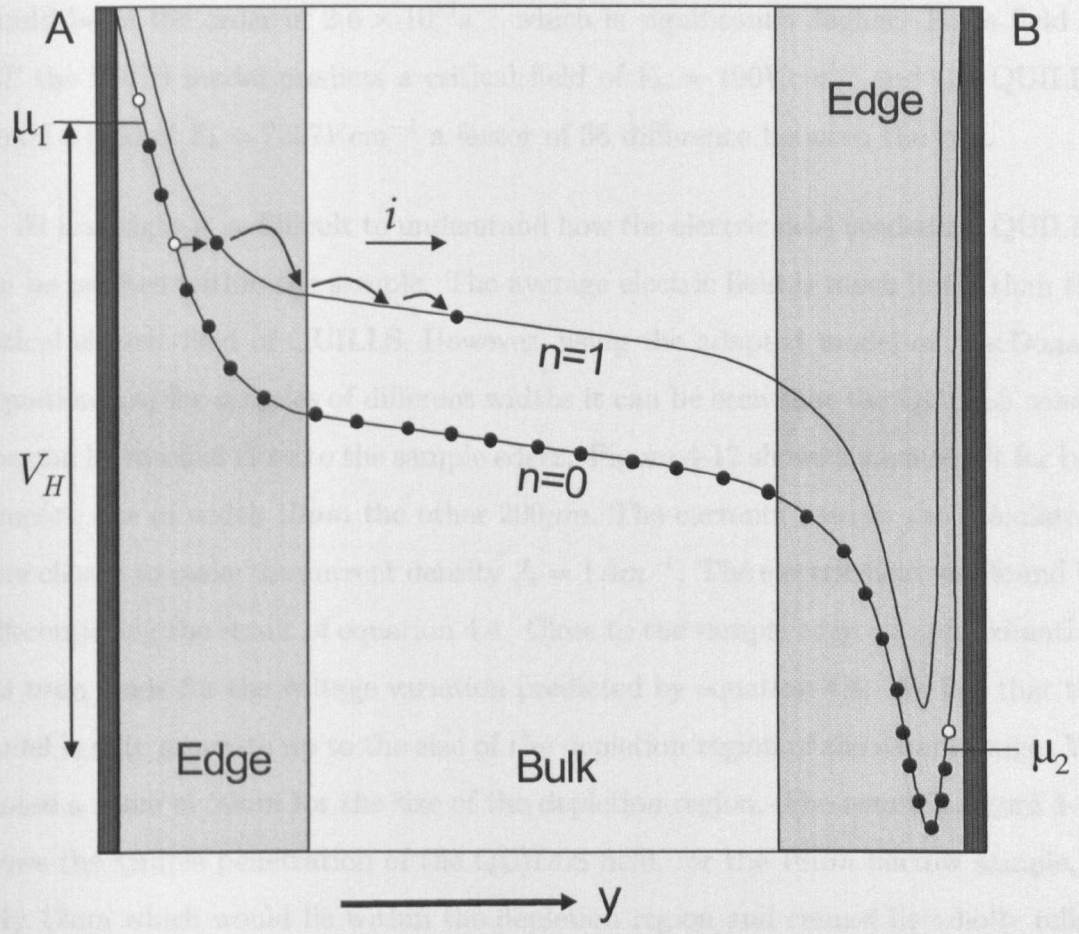

Figure 4-11: The Hall potential (V(y)) variation across the width of a Hall bar is shown. The Landau levels are indicated by the solid lines, the electrons by solid black circles and holes by white circles. The Hall current, I, in the sample is perpendicular to and and directed towards the page. The shaded areas correspond to regions of high electric field at the sample edges and the white central region the bulk, an area of low electric field. The black areas are the depletion regions. The chemical potentials on each side of the sample are indicated by μ_1 and μ_2 respectively. An electron is shown to be excited from n=0 to n=1 where it scatters from L-R due to the potential drop across the sample. The cross sample current generated is labelled i.

either model is due to the value of the frequency used in each. The QUILLS model uses the cyclotron frequency and BSEH the scattering time. Both models predict a proportional dependence on the frequency with magnetic field for a field of 1T Komiyama has a frequency of $1 \times 10^9 s^{-1}$ whereas Eaves suggests the frequency should be of the order of $2.6 \times 10^{13} s^{-1}$ which is significantly higher. For a field of $10T$ the BSEH model predicts a critical field of $E_b = 190 V cm^{-1}$ and the QUILLS model a field of $E_b = 7257 V cm^{-1}$ a factor of 38 difference between the two.

At first sight it is difficult to understand how the electric field needed for QUILLS can be reached within the sample. The average electric field is much lower than the critical electric field of QUILLS. However, using the adapted model of MacDonald (equation 4.4) for samples of different widths it can be seen that the QUILLS condition can be reached close to the sample edges. Figure 4-12 shows such a result for two samples, one of width $10\mu m$ the other $200\mu m$. The currents used in the calculation were chosen to make the current density $J_c = 1 A m^{-1}$. The electric field was found by differentiating the result of equation 4.4. Close to the sample edge an approximation has been made for the voltage variation predicted by equation 4.4. We feel that the model is only accurate up to the size of the depletion region of the sample edge. We choose a value of $50nm$ for the size of the depletion region. The result in figure 4-12 shows the sample penetration of the QUILLS field, for the $10\mu m$ narrow sample, is only 12nm which would lie within the depletion region and cannot be wholly relied upon. Whereas the wide sample, w=$200\mu m$, shows that a region of width 170nm from the sample edge is at or above the QUILLS condition. At such a distance, we feel the MacDonald model is valid and that this result proves that there are regions within the sample that have an electric field large enough for QUILLS to occur, at an average critical current density of $1 \mathrm{Am}^{-1}$. The result of the narrow $10\mu m$ wide sample is included because it highlights that for narrow samples a critical current density of $1 \mathrm{Am}^{-1}$ will not provide a significant region of electric field at or above the QUILLS condition. In fact the narrower the sample the smaller the region close to the sample edge that can achieve the QUILLS condition for $J_c = 1 A m^{-1}$. For samples of width $1\mu m$ the QUILLS condition cannot be reached for $J_c = 1 A m^{-1}$.

The QUILLS model combined with the MacDonald model for the potential variation within a sample, suggests the impurity producing electron-hole pairs lies close to the sample edge. The electric field needed to produce step-like breakdown is a combination of the Hall field and the impurity potential. In the edge state formalism the Hall voltage is found predominately near the edges. Therefore, the point in the sample that will reach the breakdown condition first, will be at the edges in the region of an impurity. Increasing the sample width would not consequently have a large effect on the Hall field in the regions close to the sample edge. The increase in sample width would just provide a larger sample interior whose potential drop is significantly less than that of the sample edges. The excited electrons would therefore spend longer in traversing the sample which implies the screening of the Hall potential will be larger. In such a case the excited electrons will continue to move along the equipotentials of the electric field. Therefore, the model of Martin et al. suggests a sub linear width dependence will be observed due to the edge states as reported in references [78],[79].

The generation rate of the electron-hole pairs dictates the voltage measured in the breakdown model for the steps. There is no expected length dependence as the impurity and Hall field create a critical field which produces an electron-hole pair. The electron then crosses the sample and backscatters, the hole scatters to the opposite edge and thermalises and QHBD occurs. The scale of the sample means that if the impurity lies between two different contacts then we would observe breakdown between these contacts. The changing of current direction would have a different breakdown current if the impurities on one side of the sample are significantly different to those of the other sample edge. In most sample cases the impurity potentials would be considered to be similar across the sample and similar breakdown currents would be observable between edges.

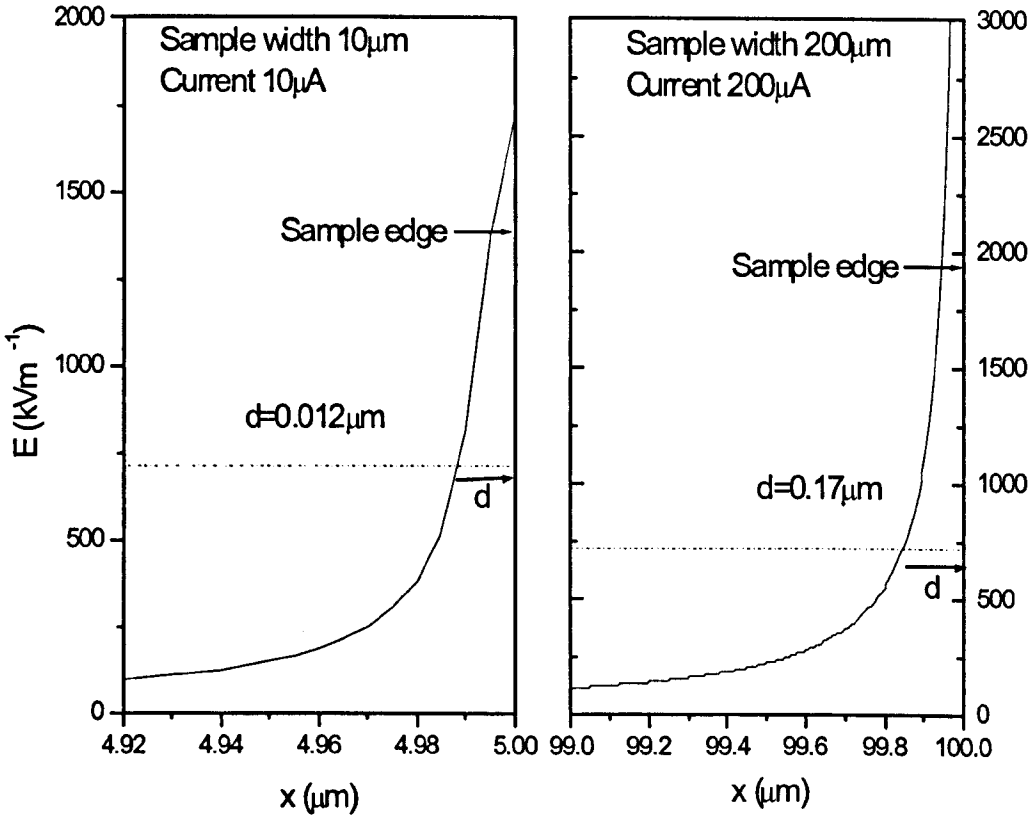

Figure 4-12: The electric field is plotted against the distance from the sample centre, x. The edges of the samples lie at x=5μm and x=100μm respectively. The dotted line is the value of the QUILLS field for a field of B=10T.

Chapter 5

Quantum Hall effect breakdown, the experimental results

5.1 Introduction

This chapter describes an experimental study of the quantum Hall effect breakdown (QHBD). These results are divided into two categories. The first category relates to results that show a step-like increase of the dissipative voltage, V_{xx}, in QHBD. Two Hall bar samples showed clear step-like features in V_{xx}. The sample's properties and dimensions are presented followed by a description and discussion of the nature, size and reproducibility of the steps in V_{xx}. Such behavior can only be explained using a microscopic model and is therefore termed 'microscopic breakdown of the quantum Hall effect'. Finally, the step-like nature of the breakdown voltage is discussed in terms of the microscopic model that has been developed by Martin et al. [3].

Section 5.3 presents the results for Hall bar samples containing constrictions. The section starts by explaining the sample design and explaining why we believe bootstrap electron heating (BSEH) [2] will be suppressed in samples containing a short constriction region. A description of precisely how the critical current is measured follows. Next the experimental results are shown. These include: measurements where V_{xx} is measured on exactly opposite sections of the sample being identical for narrow constrictions. For wide constriction samples, the negative edge exhibited dis-

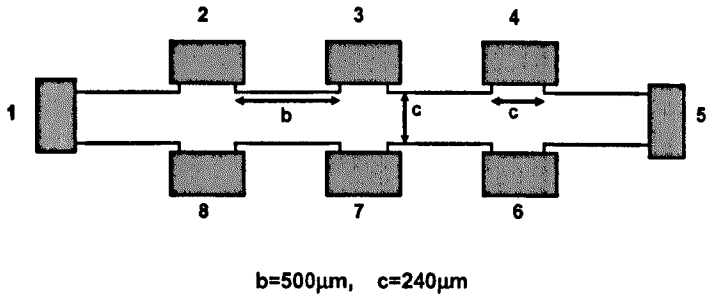

Figure 5-1: The standard Hall bar geometry for sample P. The current probes were attached to contacts 1 and 5. The voltage difference between different pairs of the other contacts were measured.

sipation in V_{xx}, before the exactly opposite section of the positive edge. A complex width dependence was also observed. For the narrow samples w<50μm, the width dependence was logarithmic. Then in the wider samples, the width dependence was more linear as predicted by BSEH. Finally, the results are discussed in terms of the inter-Landau level model of Martin et al. and the BSEH model. By considering the motion of the excited electrons and holes within the sample we propose that the inter-Landau level model of Martin et al. can be used to describe our experimental results.

5.2 Microscopic breakdown of the quantum Hall effect

The two types of GaAs/(AlGa)As heterostructures that we considered in this study displayed breakdown characteristics that are considered to be microscopic in nature. The first type, "sample N", is an n-type sample with electron density n_{2D} = $2.8 \times 10^{15}\mathrm{m}^{-2}$, mobility $\mu = 100\mathrm{m}^2\mathrm{V}^{-1}\mathrm{s}^{-1}$. It is used by NIST as the US resistance standard [81]. The second type, "sample P" (NU1156), is a p-type sample with hole density $p_{2D} = 10^{15}\mathrm{m}^{-2}$, and mobility $\mu = 13.4\mathrm{m}^2\mathrm{V}^{-1}\mathrm{s}^{-1}$, which was grown at Nottingham with our MBE reactor [65]. Both samples have a standard Hall bar geometry, sample N having width w =400μm and length l =4.6mm. For sample P,

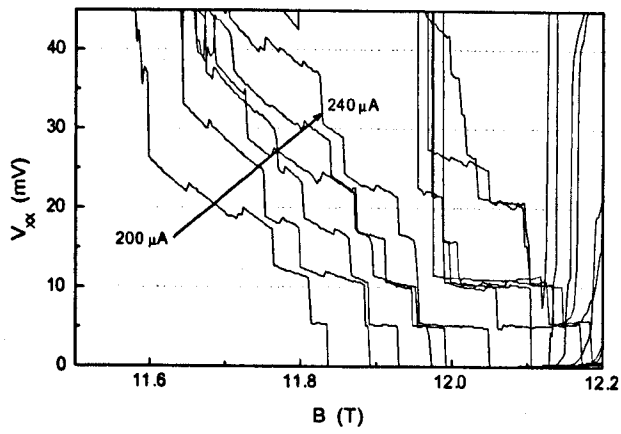

Figure 5-2: $V_{xx}(B)$ is plotted for sample N at different values of I ($200 < I < 240mA$). The magnetic field region is close to $\nu = 2$ and $T = 1.5K$. Several steps of height 5mV can clearly be seen. Data taken by J. M. Matthews at NIST.

$w = 240\mu$m, $l = 3$mm, see figure 5-1. The measurements of the QHBD for sample N were taken by J. M. Matthews of the National Institute of Standards and Technology (NIST) group and the data analysed in Nottingham.

Steps of constant amplitude in the longitudinal voltage, V_{xx}, at currents close to I_c can be seen for both samples. Sample N shows steps of height $\sim 5mV$ at a temperature of 1.3K in the vicinity of $\nu = 2$, as shown in figures 5-2, 5-3. Sample P shows steps of $\sim 1mV$ at T=0.3K in the region of $\nu = 1$, see figure 5-4. Sample P also showed some steps on the high magnetic field side of the $\nu = 2$ dissipationless region.

The transition between the quasi-dissipationless state and the first few voltage steps to the onset of fully developed breakdown is measured over a wide range of V_{xx} for sample N. Figure 5-3 shows a logarithmic plot of V_{xx} against magnetic field around $\nu = 2$ (11.4T) for a range of current values at a sample temperature of 1.5K. At $\nu = 2$ the sample shows a dependence on the direction we sweep the magnetic field. We start by observing the point where $\nu = 2$ and the sample is in the quasi-dissipationless region, $V_{xx} < 1\mu V$. Sweeping B downwards away from the plateau centre, initially V_{xx} remains dissipationless. As B decreases, a sudden discontinuous

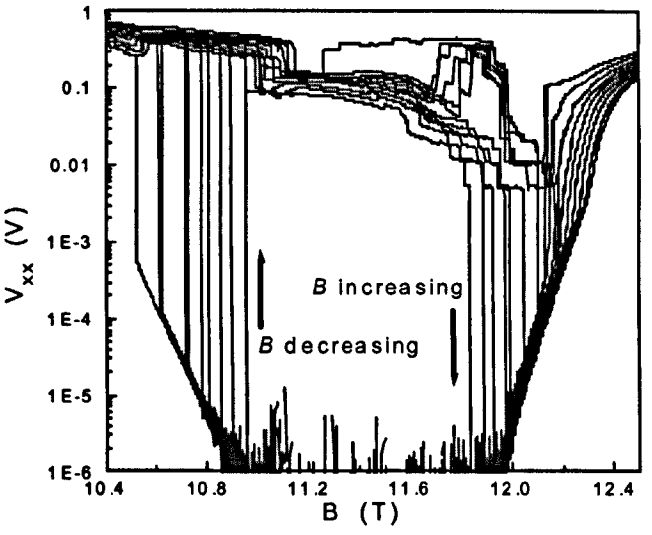

Figure 5-3: $V_{xx}(B)$ is plotted for sample N on a logarithmic scale at different values for the current I ($100mA < I < 240mA$). The magnetic field region is close to $\nu = 2$ and $T = 1.5K$. The steps can be seen for B=11.6-12T. A hysterisis is apparent from the arrows showing the direction of the magnetic field sweep. Data taken by J. M. Matthews at NIST.

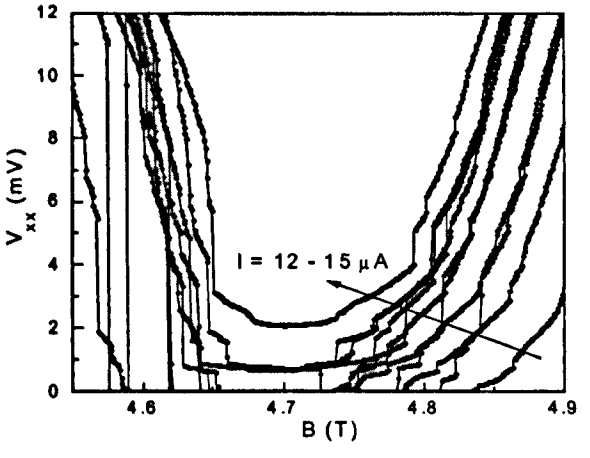

Figure 5-4: $V_{xx}(B)$ is plotted for sample P at different values of the current I ($12 < I < 15\mu A$). The magnetic field region correponds to that of around $\nu = 1$ and $T = 0.3K$. Steps of 1mV can be seen in the traces especially around B=4.75T.

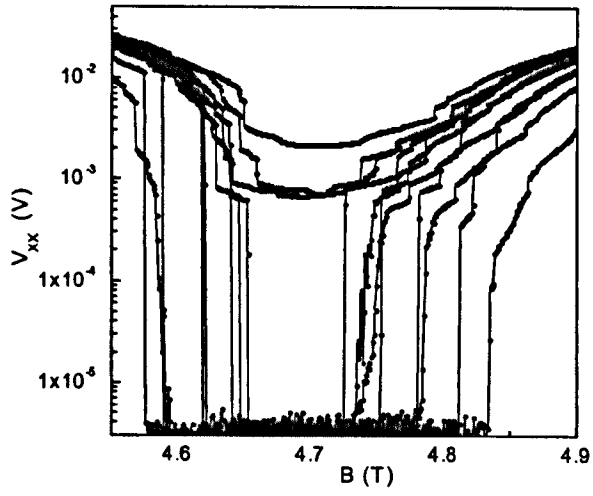

Figure 5-5: $V_{xx}(B)$ plotted on a logarithmic scale for sample P at different values of current I ($12 < I < 15\mu A$). The magnetic field region corresponded to filling factors around $\nu = 1$ and $T = 0.3K$. Steps can be clearly seen in the dissipation around the mV level. Although not marked a hysterisis is present, the curves displaying dissipation at B=4.7T are those sweeping B from low (4.6T) to high (4.9T). When B is swept from high to low the system is dissipationless at B=4.7T.

jump in V_{xx} over 5 decades occurs to a value of $V_{xx} \approx 100mV$ corresponding to fully developed breakdown. Increasing B from the low magnetic field value (10.4T), the dissipation is seen to decrease in a series of steps as shown in figures 5-2 and 5-3. Eventually, upon reaching the 5mV step height, the dissipation decreases discontinuously to the sub μV level. As the field is increased further B>11.9T, V_{xx} is seen to increase smoothly with the field up to the mV range. Thus a clear hysteresis is observed. Sample P showed similar behavior though the trend is not as clear. The steps in V_{xx} for sample P are observable on both sides of the $\nu = 1$ dissipationless region.

The steps are reproducible for each sample, but the position of each step in magnetic field and current varies from sweep to sweep. Sweeping the magnetic field up and down clearly shows steps in V_{xx} with generally random transition points inside a fairly narrow range of B around filling factor, $\nu = 2$ (sample N). Steps were observed on all pairs of voltage probes for both samples. The step position

on voltage probes on the same side of the sample was different i.e. the potential between contacts 2-3 and 3-4 on figure 5-1 showed steps but in different positions. Conversely, in the field region where steps were found the samples showed identical V_{xx} signals for measurement using opposite pairs of potential contacts (e.g. 3-7 and 4-6). Sample N also displayed similar behavior. For magnetic fields away from the integer filling factor this identity is broken and a difference is observed between the edges.

The following is a summary of the temperature dependence of the steps in V_{xx}. The steps for sample P disappear quickly when the temperature is increased above 0.7K, where the steps merge to become one large step before disappearing altogether. At lower temperatures, the step height shows little deviation from 0.9mV. Hysteresis is strongest for lower temperatures (0.3K the lowest obtained) and decreases with increasing temperature. The steps for sample N showed stability at temperatures T=0.33-4.2K [29],[50],[81].

Figures 5-2-5-4 show the presence of steps for several fields and currents. The step size appears to be independent of both the current and field at $V_{xx} \sim 5mV$ and $1mV$ for samples N and P respectively. A strong in-plane magnetic field was applied to sample P by tilting the sample. Due to the in-plane field dependence of the spin splitting, the $\nu = 1$ plateau became wider and I_c increased until it reached a saturation point of $25\mu A$ at an in-plane field of 12T. Thus using tilted fields the range of currents at which the steps could be observed was 12-$25\mu A$. No current or magnetic field dependance was observed and the step height remained 1mV. The constant step height with in-plane field indicates that spin-flip transitions are not relevant to the origin of the breakdown steps.

As reported in [65] a short period of illumination was found to destroy the steps in dark V_{xx} measurements, for sample P.

Step-like structure was also observed on two other samples. Both samples were fabricated from an heterostructure labelled NU439 with $n_{2D} = 5.6 \times 10^{11} cm^{-2}$ and $\mu = 20 m^2 V^{-1} s^{-1}$. The first sample, A, was fabricated into a standard Hall bar.

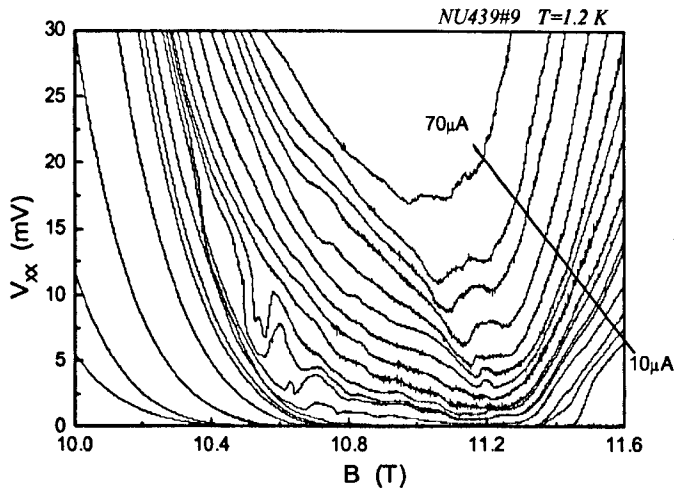

Figure 5-6: The voltage versus current for sample A. The currents applied are 10-40μA in 5μA steps, 42-66μA in 2μA steps and 70μA. Unusual peak-like features can be seen for a range of currents at B=10.6T and 11.2T. Wide step like features may be observed for low currents in the magnetic field range 10.8-11.2T.

The second sample, B, was fabricated into a constriction-type sample as described in chapter 2. The longitudinal voltage V_{xx} measured when sweeping the magnetic field in the region of $\nu = 2$ and temperature T=1.2K can be seen in figure 5-6 and figure 5-7 for sample A and B respectively.

Sample A shows clear peak-like features in V_{xx} in the field region of 10.6T for several currents . There is also an indication of step-like features in the I(V) at a magnetic field 10.9T. A second set of less distinct features in V_{xx} can be seen starting at 11.2T for the low current values and moving up in voltage and down in magnetic field as the current is raised.

Sample B shows a smooth breakdown dependance in the left hand side of the plateau and a step like breakdown in the for magnetic fields above $\nu = 2$, see figure 5-7. The corresponding step features have an approximate height of $5mV$ for the low current values, $14 - 16\mu A$, and step height of approximately $10mV$ for the middle range breakdown currents, 17-25μA.

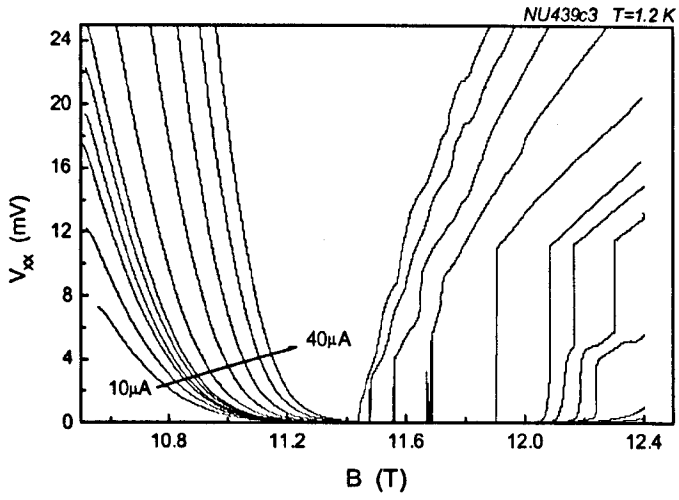

Figure 5-7: $V_{xx}(B)$ for a constricition sample, w=50μm, made from wafer NU439. Step-like structure can be seen in the high field side of the $\nu = 2$ plateau (B>11.4T).

5.3 Discussion of the step-like QHBD

The presence of voltage steps in the QHBD for constant current with magnetic field sweeps is well explained quantitatively by the microscopic model of Martin et al. [3]. The step heights predicted by the model match those found experimentally for both Cage's N type sample and our P type sample, two very different systems. The BSEH model [16] cannot easily explain these results.

Let us now consider how we can explain the large hysteresis observed in V_{xx}, at high current values. This is shown in figure 5-3 for sample N. At $\nu = 2$ the n=0 Landau level is fully occupied, n=1 is empty and V_{xx}, is in the dissipationless regime. Decreasing the magnetic field lowers the degeneracy of the n=0 Landau level and electrons are forced into the n=1 Landau level localised states. Eventually all the localised states lying between the n=0 and n=1 Landau levels will be filled. As the magnetic field is decreased further, greater numbers of electrons need to be accommodated in the n=1 Landau level. These electrons start to fill the n=1 extended states and a large smooth increase in dissipation is observed, see figure

5-3. Now if the magnetic field is increased once again, from low field to high field, the degeneracy of the n=0 Landau level increases and electrons can relax back into these states of lower energy. Thus the n=1 Landau level extended states become unoccupied. We believe that before the extended states become empty, the few electrons that are still residing in the extended states screen the Hall field in the sample. Regions near the samples edge and in the presence of an impurity then have a large enough electric field to produce electron-hole pairs, as described in the model of Martin et al. With multiple impurities producing electron-hole pairs, large amounts of dissipation is observed in V_{xx}. The production of electron-hole pairs provides electrons in the n=1 Landau level extended states which continue the screening. Further increasing the magnetic field increases the Landau level separation and more electrons in the n=1 Landau level relax back into the n=0 Landau level. A larger electric field is now needed to produce electron-hole pairs. Some impurities will no longer be able to produce electron-hole pairs and fewer electron-hole pairs will be produced. With fewer electrons to screen the Hall field in the central sample region the electric field at the sample edges decreases. One by one the impurities stop producing electron hole pairs as the electric field falls below their individual critical value. A step down in V_{xx} of 5mV, is observed as each impurity stops producing electron-hole pairs. Finally the last impurity stops producing electron hole pairs and V_{xx} drops from 5mV to the baseline value of the dissipationless regime. Therefore using the model of Martin et al. we can explain the observed hysteresis and the step size. The hysteresis was also observed by Eaves et al. [65] and to a lesser extent here with sample P.

A crucial point within the model of Martin et al. is that electrons scattering across the sample will slow due to the lower electric field within the central region of the sample. Nevertheless, V_{xx} measurements taken by pairs of contacts exactly opposite each other across a sample are identical within the resolution of the experiments. The fact that the two exactly opposite edges measure exactly the same dissipation indicates that every electron-hole pair created by the impurities thermalises on the opposite edge. Such a result indicates that due to the lower n=0 Landau level being

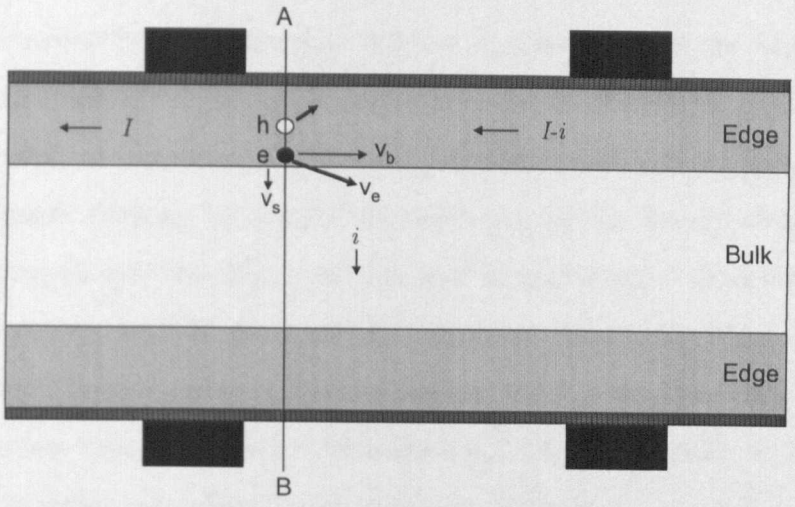

Figure 5-8: The formation of an electron-hole pair is shown for a standard Hall bar. The full circle, e, is the electron and the empty circle, h, the hole. The black areas are the sample probes and the dark shaded areas the depletion zones. The light shading shows the regions of high electric field and the area of lower electric field is shown by the white area. The scattering velocity of the electron is labelled v_s, the velocity due to the electric and magnetic fields v_b and the resultant velocity v_e. The line AB corresponds to the AB labelling in figure 4.11. The current I is shown to change with the creation of an electron-hole pair due to the cross-sample current i.

fully occupied there are no available states for the electron to relax into. This idea is in contradiction to that of the BSEH model where electrons are expected to be able to relax into the lower Landau level. We believe that the electrons are slowed in their cross sample scattering by the lower electric field in the sample interior, the bulk region of figure 5-8. However, the large distances, 1mm, between voltage probes ensures that all the excited electrons scatter across the sample within the interval between voltage probes.

The observed steps in V_{xx} are always present for the samples at the critical currents. However, the steps' position in magnetic field and their dependence on current, are different for each sweep of the magnetic field. We believe the inreproducibiltiy of the step position with current and magnetic field may be associated with the disorder in the sample. For each sweep of magnetic field the Landau levels are populated and depopulated. We consider the localised electrons to be those trapped on the poten-

tial fluctuations within the sample. It is likely that populating the localised states within a Landau level is a process that is never repeated exactly the same each time. We believe that the localised electrons will reorder themselves in a slightly different manner with each magnetic field sweep. Therefore, as the electron distribution within the sample changes we expect the screening by the filled localised states to change. Consequently, the critical current and magnetic field needed to produce a local critical electric field for an impurity will vary. Hence, the steps positions are irreproducible. This reasoning is further supported by the following results. Pairs of voltage probes exactly opposite each other on the edges show an identical V_{xx} dependence, including step height and position. This is due to an impurity present in-between the 4 voltages probes (two on each side) producing electron-hole pairs which scatter to the sample edges and thermalise. Two different pairs of voltage probes on the same side of the sample as each other show steps that have different positions in the magnetic field and current. We understand this as each pair of contacts measuring the dissipation due to different impurities each with their signature of magnetic field and current dependence.

The presence of steps is found to be temperature-dependant for the P type sample and temperature independent, T$\leq 4K$, for the N type sample. For the P type sample the steps were observed in the spin split Landau level n=0 and $\nu = 1$, where the Landau level separation was approximately $\hbar\omega_c \approx 1.6$meV. At a temperature of 0.3K, the thermal population of the higher energy Landau level is very small. However, at a temperature of 1K the probability of thermal excitement increases by 6 orders of magnitude. The increased thermal population of the upper Landau level could smooth the step profile. The N type sample does not show this behavior because the Landau level separation is large (17.4meV), due to the larger magnetic fields used and the smaller effective mass of the electrons. Therefore, even at 4K the thermal population of the higher energy Landau level is very small and the steps are unlikely to be smoothed by thermal excitation processes.

Using an in-plane magnetic field it is possible to modify the spin splitting without changing the filling factor ν. However, the height of the voltage steps in the spin split

$\nu = 1$ region remained insensitive to the application of an in-plane magnetic field. In our model we believe that during breakdown the electrons scatter in-between Landau levels and not between spin states. For scattering between spin states the impurity would have some magnetic component. We believe that this is not the case and scattering occurs from a charged impurity. Therefore the step-like breakdown is independent of spin effects.

We also briefly investigated the effects of illuminating sample P with light and then measuring the dark magneto-resistance when the light is switched off. An increase of carriers was observed and the steps disappeared. It is thought that illumination can improve the homogeneity and increase the mobility for the samples. If the critical field for all the impurities becomes similar then the individual steps would be blurred by a sudden onset of dissipation due to a great number of impurities.

5.4 Reconciling bootstrap electron heating and quasi-elastic inter-Landau level tunneling

5.4.1 Sample design

The samples described in the following section were designed to provide short local regions of QHBD. The sample geometry is shown in figure 5-9. The design comprises: two wide standard Hall bars w_h=200μm, connected via two progressively constricted regions of length 200μm, and totalling 600μm between contacts. The centre of the constriction region is the narrowest, consisting of a rectangular section of length, 10μm or 2μm and physical width 2, 10, 20, 50, 100μm. The narrow central rectangular part of the constriction region probably defines the behavior of the constriction region. Consequently, when the constriction length and width are discussed it refers to the narrow central section of the constriction region.

The current source is connected across contacts 1, 6 (see figure 5-9) and the potential difference is measured using the contacts along the edges of the sample, for

example V_{xx} across the constriction is measured between contacts 3 and 4. There is a distance of $200\mu m$ between the first set of potential contacts and the current contacts 1 and 6 to ensure that the quasi-dissipationless region in V_{xx} common to the QHE Hall effect is established in the current flow approaching the contact. For the currents needed to create QHBD in the constrictions, the potential contacts are well separated from the regions of high dissipation around the 3D contact 2D system boundary [94], [95]. It is thought that the long wide Hall bar regions either side of the constriction will remain in the QHE regime whilst the constriction region undergoes QHBD. The Hall voltage across the sample is independent of sample width and only depends on the current. Shrinking the sample width at constant current will therefore provide an increase in the electric field in that region. The constriction region thus experiences a higher electric field than that of the wide part of the sample, indicating that breakdown will occur in the constriction region before any other part of the sample. The gradual narrowing of the sample width in the central constriction region is an attempt to ensure the system undergoes a smooth transition into the high field region. Upon leaving the constriction the hot electrons quickly enter an area of lower electric field and any QHBD processes will be stopped. The constriction length is short $2\mu m$ and $10\mu m$. According to the model of Komiyama et al. [86] BSEH needs a length of approximately $100\mu m$ to develop [88],[89] which is not possible in the constricted regions of our samples. The constriction sample geometry is designed to be one that promotes a QHBD in a local region of the sample that is too short for the breakdown described by BSEH to occur.

5.4.2 Defining the critical current

The critical current I_c, is important when comparing different samples as it can be used to identify a width dependence or the effect of changing the mobility of the sample. Therefore, in comparing values of I_c, it is important that the same method is used to define I_c. There are two possible methods in measuring I_c. In one the magnetic field is swept across the dissipationless region for individual values of current. The current then can be increased gradually each time until there is no

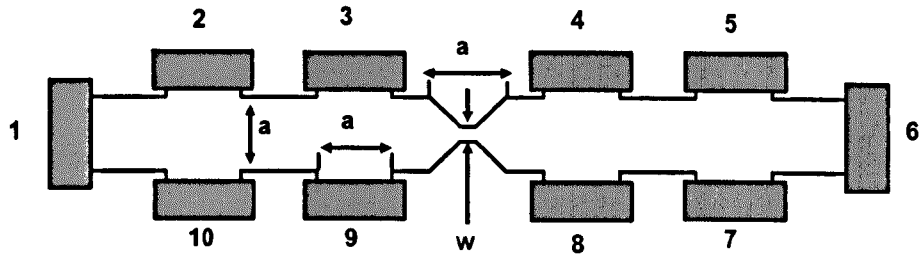

Figure 5-9: The constriction sample schematic. The length of the constricted region was either 10 or $2\mu m$. The grey regions correspond to the electrical contacts. the current was passed between contacts 1,6, V_{xy} was measured across the sample i.e V(3,9) and V_{xx} across the constriction i.e. V(3,4).

region showing dissipation. The point at which dissipation occurs, can be arbitrarily set for example at 10^{-4}V. Once the whole curve is at or above this value then the system is said to be fully broken down and the appropriate value of current is noted. The advantage of this method is that the critical current can be determined with an accuracy of the size of a current step. The disadvantage is that it is time-consuming and the dissipation value is chosen somewhat arbitrarily. The other method and the one used to define the critical current of the samples measured for this research is to measure the I(V) characteristics of the sample at different magnetic fields within the plateau region. The sharp sudden onset of dissipation seen when V_{xx} is plotted on a logarithmic scale against the current I (linear scale), is then extrapolated back to the level of the noise ($\sim 0.5\mu V$) on the current axis giving the breakdown current, see figure 5-10. The magnetic field at which the highest breakdown current occurs is taken as the plateau centre and its breakdown current is chosen to be I_c. The advantage of this method is that the breakdown current is derived free from arbitrary parameters. It is also a comparatively quick set of measurements in relation to the first method. The disadvantage is the magnetic field step needs to be small enough to ensure the curve from which I_c is derived is actually taken at the field which would yield the highest value for I_c.

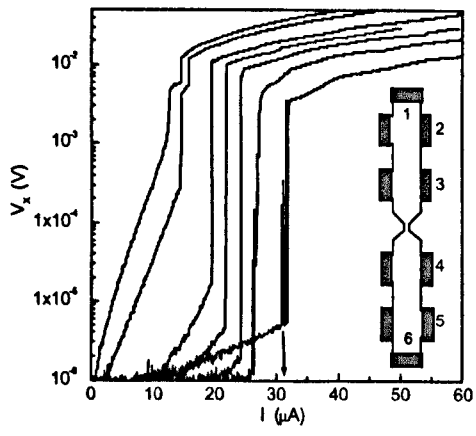

Figure 5-10: Voltage current dependence at magnetic fields close to the filling factor $\nu = 2$, these curves are used to determine I_c. B varies from 11.4T (right) to 12.4T (left) in 0.2T steps. The inset shows the sample geometry used.

5.5 Experimental results for QHBD in constriction samples

Two GaAs/(AlGa)As heterostructures were fabricated into constriction samples: NU439 with mobility $\mu = 20m^2V^{-1}s^{-1}$ and electron sheet density $n_{2D} = 5.6 \times 10^{11}cm^{-2}$; NU1624 with $\mu = 70m^2V^{-1}s^{-1}$ and $n_{2D} = 4 \times 10^{11}cm^{-2}$. Using figure 5-9 to identify the sample geometry, the current was passed between probes 1 and 6 and the onset of dissipation in the region of the constriction was detected by measuring the potential difference V_{xx} between probes 3 and 4. The critical current is obtained as mentioned in the previous section.

Dissipation was observed in the constriction region, whereas measurements taken simultaneously on the wide-parts of the sample showed no measurable dissipation. Such behavior is expected for our constriction samples showing that breakdown does indeed occur in the region of the constriction. After the constriction the carriers relax back into the normal QHE regime and dissipation was no longer observed.

For samples made from wafer NU439 with constrictions of $w \leqslant 10\mu m$, the voltage

V_{xx} was found to be identical on exactly opposite pairs of contacts, i.e. $V_{xx}(3,4)$ and $V_{xx}(9,8)$ in figure 5-9. This identity was found to an accuracy of <0.1%. This 'opposite edge identity' occurred only in the region where V_{xx} was dissipationless region and was accurate to $<\pm 0.1\%$. All the samples, whether they displayed this 'opposite edge identity' or not, showed difference in V_{xx}, measured with exactly opposite contact pairs, at magnetic fields out of the dissipationless region. The wider samples w$\geq 20\mu m$ showed a difference in V_{xx} when measured on exactly opposite contact pairs. These results can be seen in figure 5-11. The difference between V_{xx}, as measured using opposite contact pairs across the constriction, is clearly visible for the samples of constrictions w=$20\mu m$ and $50\mu m$. We label the edge in which V_{xx}, displays significant dissipation whilst its counterpart remains dissipationless the 'hot edge'. Accordingly the opposite edge to the hot edge is labelled the cold edge. Measurements indicate that the hot edge corresponds to the negative edge. Samples made from NU439 and NU1624 showed hot and cold edge behavior. However, the higher mobility NU1624 wafer kept an 'edge identity' for constrictions of widths $50\mu m$ and also the constriction of width $100\mu m$ showed a small difference in V_{xx} measured on opposite contact pairs.

Measurements of V_{xx}, made on opposite contact pairs in the wide regions of the samples showed hot and cold edge effects also. For the wide section of the sample, after the constriction, from the reference of the electrons motion, a significant difference was noticed between opposite edges. The breakdown current was found to be unexpectedly low for such a wide part of the sample $I_c \approx 50 - 100\mu A$. The difference in V_{xx}, measured by opposite contact pairs, was marked for both wafer types. Unfortunately, the measurements on the wide section, before the constriction from the electrons perspective, were affected by the proximity of the current injecting contacts for these higher current. Therefore discerning whether the hot/cold edge features were an artifact of current injection, or a consequence of QHBD, in the wide parts of the samples was not possible.

Figure 5-12 presents the experimental data measured at $\nu = 2$ in constriction samples with widths from 1-$100\mu m$. The samples with physical constriction w=$2\mu m$

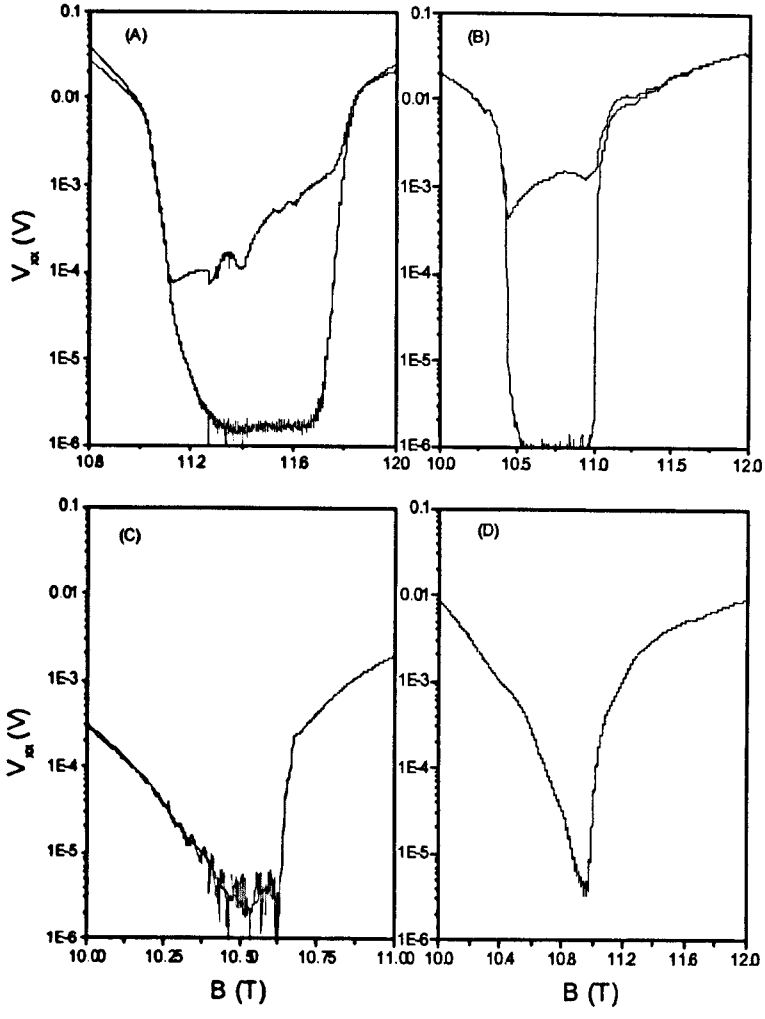

Figure 5-11: The V(B) plots for samples made from wafer NU439, with different constriction widths. Each plot contains V_{xx} for exactly opposite voltage probes across the constriction region. **It is emphasised that plots C and D both contain two almost identical traces, measured for each edge.** Figure (A) shows the $V_{xx}(B)$ dependence for a constriction of w=100μm, L=10μm and I=85μA. The difference between the opposite edges can be clearly seen. Whilst one of the edges remains dissipationless the other has significant dissipation. Figure (B) shows the $V_{xx}(B)$ dependence for a constriction w=20μm, L=10μm and I=28μA. A difference can be seen between the edges with one edge showing dissipation whilst the other remains dissipationless. Figure (C) shows the $V_{xx}(B)$ dependence for a constriction w=1μm, L=10μm and I=5μA. The edges show an identity in V_{xx}. Figure (D) shows the $V_{xx}(B)$ dependence for a constriction w=1μm, L=2μm and I=9μA. Again V_{xx} is identical between the edges.

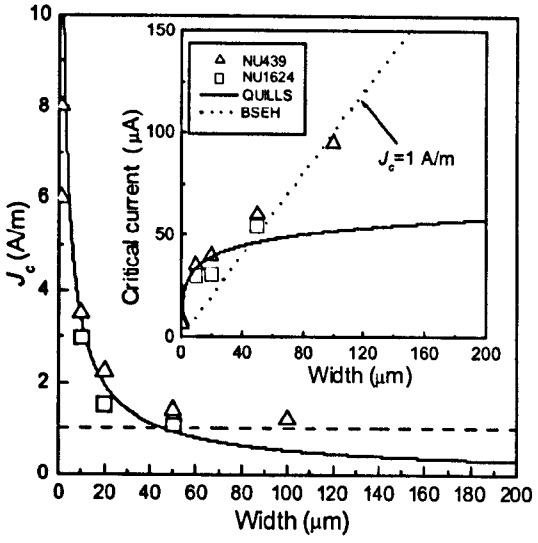

Figure 5-12: J_c and I_c (inset) versus the constriction width at $\nu = 2$. Dashed lines represent the linear behaviour of $J_c = 1Am^{-1}$. The solid lines represent the QUILLS model.

were determined to have an effective width of $1\mu m$ from the resistance measurements at zero field. Samples with width $w < 50\mu m$ show a clear non linear $I_c(w)$ dependance with a maximum critical current density for the $1\mu m$ samples of $6 - 8Am^{-1}$. Wider samples ($w \geqslant 50\mu m$) show results similar to conventional Hall bars, with $J_c = 1Am^{-1}$. When I_c was found to be different when determined from opposite contact pairs i.e. for the wider samples with hot and cold edges, the average value was taken for I_c and then plotted on figure 5-12.

Figure 5-13 plots the critical current density over filling factor J_c/ν versus the magnetic field for a wide range of samples measured by different groups including data taken as part of this thesis project. These include conventional Hall bars, corbino-type and constriction samples. The empirical relation $J_c = 0.05\nu B$ or equivalently a critical group velocity of $v_c = 1300ms^{-1}$, close to the critical velocity predicted by Streda [93]. This fit is at least as good if not better than that given by the BSEH model equation 4.16. Note the two models would nearly coincide if the electron phonon relaxation time in the BSEH model is assumed to remain constant

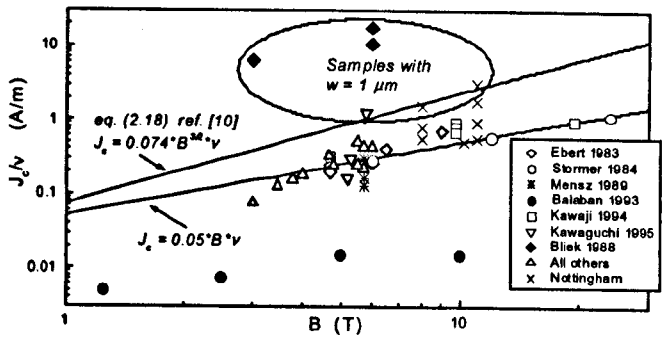

Figure 5-13: J_c/ν measured by 14 authors. Solid lines represent approximations made by the phenomenological $J_c = 0.05\nu B$ and the BSEH expression for $E_c(B)$. All data inside the ellipse were measured on samples with $1\mu m$ constricitons.

with changing B at $\tau_e = 2ns$. Figure 5-13 is quite hard to interpret with so many results plotted with no account taken of temperature or length of the sample. However, the majority of the samples can be roughly predicted by the Streda and BSEH models. There are a few groups findings that lie outside the main trend of data: that of Balaban et al. [78], [76] and that of the $1\mu m$ samples of Bliek et al. [70] Kawaguchi et al. [87] and our data. The $1\mu m$ data of Bliek et al., Kawaguchi et al. and of the Nottingham group have J_c values 1 to 6 times that of the general trend and are best described by the QUILLS model. The data taken by Balaban et al. falls way short of the main trend but interestingly was described using the QUILLS model.

5.6 Discussion of the constriction sample results

The lack of dissipation in the wide part of our samples, either side of the dissipative constriction region, indicates that breakdown is occurring in a local region of the sample in the constriction. There are no effects due to the current injecting contacts as the wide regions of the sample show no dissipation. The constriction length is small, either $2\mu m$ or $10\mu m$, indicating that BSEH is unlikely to be the cause of breakdown as the required length for BSEH, $\backsim 100\mu m$, cannot be achieved in

the constriction region. Instead once the electron leaves the constriction it enters the wide part of the sample where the electric field is much less than that needed for BSEH to occur [86], [16]. The constrictions of effective width $1\mu m$ displayed a critical current density of the order $6-8Am^{-1}$. From the general trend of results and BSEH, a critical current density of roughly $1\mathrm{Am}^{-1}$ is expected. These high critical current densities coupled with the short constrictions indicates that BSEH is not the dominant mechanism for the breakdown of our narrow short constrictions.

The observed edge identity within the plateau region is indicative of a microscopic type process in the QHBD. In the microscopic viewpoint of QHBD, the system is in the QHE regime for integer filling factor values i.e. $\nu = 2$. However, for currents close to $\mathrm{I_c}$, impurities are creating electron-hole pairs. The holes in the lower Landau level move toward the negative edge and thermalise allowing dissipation to be observed on that edge. Electrons scatter across the sample toward the positive edge where they in turn thermalise and dissipation will be observed. It is thought that a macroscopic model cannot describe an edge identity to an accuracy of <0.1%, due to the randomness of the sample. In a macroscopic model a small difference would be expected between the edges, because the disorder within the sample is slightly different on each edge. However, in narrow samples this difference may be immeasurably small.

Let us now consider the result that the critical current determined from $\mathrm{I}(\mathrm{V}_{xx})$ measurement is different depending upon which edge of the sample we investigate. We have described a hot edge and a cold edge effect which is observed by other authors [86], although it is not commented upon. At present there is no model for such behavior. In the following, it is proposed that such an effect can be described by a microscopic viewpoint of QHBD rather than the BSEH model. The conclusions, while plausible, will need further experiments to confirm their validity.

The QUILLS condition requires a high electric field to occur. From the theory of MacDonald, modified by Beenacker and van Houten [52], it has been shown in the previous chapter that close to the sample edges, the electric field is high enough to

meet the QUILLS condition. Evidence for this has also been found in the experiments of Balaban et al. and Bliek et al. [78], [70]. We make the assumption that the breakdown occurs at the negative or hot edge of the sample as indicated by our experiments. Why the negative edge is the hot edge is not considered. We note that the electric field is as large at the opposite edge in the model of McDonald. However, in real systems, at the positive edge the potential due to the Hall field has to fight the sample edge potential, see figure 4-11, resulting in a lowering of the electric field. We consider for simplicity, the case of a single impurity. When the critical electric field is reached for an impurity, an electron-hole pair are created. The electron is excited into the empty upper Landau level and a hole is left in the lower Landau level. As the process is thought to occur close to the sample edge, in the edge state model, the electric field is high and the hole will quickly scatter towards the nearby negative edge and the electron will scatter toward the distant cold edge. It is worth remembering that the electron and hole retain their velocity in the x direction $v_x = E/B$. The electron on its journey across the sample will find itself in the middle of the sample where the electric field is weakest and therefore its scattering across the sample will be slowed until it can reach the far edge where the electric field increases again and backscattering can occur. This process of QHBD is illustrated in figure 5-8. The electrons resultant velocity v_e is shown as a combination of the velocity due to the Hall field v_x and the cross sample scattering velocity v_s. It is this idea of the electrons scattering across the sample whilst retaining a velocity in the x direction that will be used in the following discussion.

For our constriction samples, the edge identity found in narrow samples w<20μm, and hot edge behavior in the wide samples w>20μm can be qualitatively explained in terms of a QUILLS excitation followed by cross sample scattering. Electrons excited into the upper Landau level in short narrow constrictions will scatter quickly across the sample within the constriction region. According to the model of MacDonald [53], in narrow samples the electric field in the middle of the sample is greater than in wide samples if the current density is kept constant. Consequently, the cross sample scattering of the electrons will be quicker for narrow samples than wide ones because

of the higher electric field in the sample interior. Furthermore, electrons only need scatter a short distance to reach the opposite edge in narrow samples. Therefore it is likely the electrons will scatter across the sample whilst in the constriction region and an edge identity occurs. We are assuming that the increase in the electron velocity v_x, is offset by the increase in scattering rate and therefore v_s, due to the increased electric field and the small width of the narrow samples.

The wide, short constriction samples show hot and cold edge effects in their breakdown characteristics. We understand such a result by noting the lower electric field in the middle of the sample as compared to that of narrow samples. It is also apparent that the electrons have to scatter a large distance in order to reach the opposite edge for wide samples. Electrons scattering across the sample will find themselves slowing their cross sample scattering in the sample interior, due to the lower electric field, whilst retaining a small velocity v_x along the sample length see figure 5-8. It is likely that some of the excited electrons fail to cross the sample before the short constriction region finishes. The excited electrons leave the constriction region and enter the middle of the wide part of the sample where the electric field is significantly lower than in the constriction region. The cross sample scattering velocity of the electrons will therefore decrease. Peaks and valleys in the potential change across the sample due to disorder may well stop the electrons crossing the sample. For simplicity we apply the condition that these excited electrons cannot relax into the filled lower Landau level. The excited electrons will continue slowly scattering across the sample until they reach the far edge. However, the point at which these electrons reach the positive edge of the sample may be outside the edge interval at which the contacts measure V_{xx}. Conversely, the holes will scatter the short distance to the samples edge quickly, compared to the electrons, as the electric field in the sample edge regions is high and the hole is close to the sample edge. For contact pairs measuring V_{xx} on exactly opposite sections of the samples edge across the constriction greater numbers of holes than electrons will thermalise. Therefore the hot (negative) edge will register greater amounts of dissipation in V_{xx}, than the cold edge in the constriction region. Removing the simplification of no relaxation

processes for the excited electrons further increases this effect. The longer the excited electron is present in the upper Landau level the more likely it will relax.

The observation of hot and cold edge behavior in the wide parts of the samples after the constriction, from the viewpoint of the electrons, may also be explained using the idea of electrons and hole scattering towards the sample edges. As an aid to the following explanation we refer back to figure 5-9. The electrons are chosen to be travelling from left to right. The negative edge is the top edge with contacts 2, 3, 4, 5 being used for measurements of V_{xx}. The contacts used to measure V_{xx} across the constriction on the negative edge, are 3 and 4 ($V_{xx}(3,4)$). The measurements of V_{xx} on the wide part of the sample utilised contacts 4 and 5 ($V_{xx}(4,5)$). Note that in the wide part of the sample measured, the electrons have already passed through the constricted region. Previously we inferred that because electron-hole pairs are created close to the sample edge, the holes all manage to thermalise on the sample edge within the constricted region. To understand the unexpectedly low breakdown current $I_c = 50 - 100\mu A$, and differing hot/cold edge behavior in the wide part of the sample, we suggest that not all the created holes reach the sample edge within the constriction region. Consider the case where a tiny fraction of the excited holes have not reached the sample edge within the constriction region. We suggest a similar argument for the holes as for the electrons mentioned previously. The holes will have a velocity v_x in the x direction and a scattering velocity v_s towards the negative edge. Some of the created holes fail to reach the sample edge before contact 4 is reached. The holes are considered to be close to the sample edge in the region of a high electric field; therefore any holes having not reached the sample edge by contact 4, will do so before contact 5. All of the created holes will have then thermalised. For the case of the excited electrons we believe that because the electrons must scatter across a wide section of the sample in a region of weak electric field, not all of them will reach the positive edge; some may stay in the upper Landau level and travel past contact 7. If the constriction is broken down, we ask the question, "why we do not measure dissipation in the wide part of the sample as soon as the constriction undergoes QHBD?". The reason for this is that the percentage

of holes thermalising on the sample edge between contacts 4-5 is small. The number of holes created within the constriction region would have to be very large in order for dissipation to be measured in the wide section. Consequently, we would expect that at a critical current less than that expected for the wide section and larger than I_c, for the constriction region, dissipation should be measured in the sample edge region 4-5. Retrospectively we can now see a design flaw in our samples, namely that the current contacts were only $200\mu m$ from the first voltage contacts. In order to show that the proposed hot edge behavior of the wide part of the sample was due to breakdown within the constriction region, measurements were made on the wide section of the sample before the constriction region ($V_{xx}(2,3)$). The results seem to concur with such a description but unfortunately the proximity of the current probe obscures the evidence.

The BSEH model also considers electrons moving in the upper Landau level. However, the BSEH model does not consider the scattering of the electron across the sample. Instead the emphasis lies on the increase in energy of the electron, as it is accelerated by the Hall field along the sample length. It is thought that an excited electron excites an electron-hole pair, then these excite two more and so on. It is this avalanche process that creates the expansion of dissipation across the sample. When measuring dissipation due to the BSEH model the precise point at which it becomes measurable is unclear. It may be that once enough electrons are excited dissipation is measured. Or dissipation may only be measured once the span of the excited electrons connects the edges. In the BSEH model the electric field across the sample is considered to be uniform. The avalanche model of BSEH makes no assumption as to where in the sample the breakdown occurs. An intrinsic feature of the BSEH model is that the electric field is considered to be uniform across the sample. There is no region that is more likely to breakdown than another. BSEH cannot therefore predict a hot edge breakdown that is consistent between different samples. The lowering of the critical current in a wide part of a sample after a constriction region can be explained by BSEH. We can consider the constriction region when it is producing excited electrons to be like a jet, shooting excited electrons into the middle of the

wide part of the sample. These excited electrons will diffuse out like a cloud as they start to cool and relax into the lower filled Landau level. Dissipation will not be measured on the wide part of the sample until the cloud of excited electrons is large enough to reach the contacts at the sample edges. We suppose that an increase of the current increases the jet-like effect of the constriction and so does the electron cloud size. Such a description cannot however, describe the hot edge behavior observed in the wide parts of our samples after the constriction region. The identity of the V_{xx} value for the exactly opposite edge sections may be explainable using BSEH for narrow samples but not for wide samples. We believe that topological variations of a macroscopic length scale within the sample would create a difference in V_{xx} measured on different parts of the sample. It is possible that in narrow samples the topological variation is not large enough to measure a significant difference between the sample edges.

Below $50\mu m$ the width dependence of the critical current is sub-linear and indicates a logarithmic nature. For constrictions widths above $50\mu m$ a linear width dependence of the critical current is observed. Such a result indicates that for short narrow constrictions an edge state model, like QUILLS, can be applied to the experimental data. For wider samples the BSEH model may explain the linear behavior seen in the data. The constriction width of $50\mu m$ could be the value where a microscopic process is superceded by the BSEH model.

We will now try to understand the sub-linear to linear change in width dependence. At a critical current density of $1Am^{-1}$, samples of width greater than $100\mu m$, have regions at either edge (170nm for a sample w=$200\mu m$) where the electric field satisfies the QUILLS condition. For constant critical current density, the wider the sample, the wider this region. The QUILLS process therefore may be the source of excited electrons for the BSEH model and not thermal processes. Evidence for this may be seen in our narrow short samples. The narrow samples have little or no regions at or above the critical electric field needed for QUILLS when $J_c = 1Am^{-1}$. We suggest that in order for QHBD to be observed, the QUILLS condition must be met for a region of finite width. Applying this statement and referring to section

4.4.4 indicates that high current densities are needed to achieve QHBD in narrow samples. Our result that J_c =6-8Am^{-1} for our narrowest samples indicates that this may be the case. In the wider samples, w$\geqslant 50\mu m$, at a current density 1Am^{-1}, the QUILLS condition is met for a large enough region of the sample and will produce excited electrons. Once the electrons are excited, BSEH may take over and drive QHBD. At present defining the size of region at or above the QUILLS field needed for QHBD is difficult. The model of MacDonald [53] for the electroscopic potential across the Hall bar becomes divergent at the sample edges and is therefore unreliable close to the sample edge. However, we do gain an understanding of what is occurring in these narrow samples using the present model and perhaps further work will validate this.

Considering the QUILLS condition for wide samples, (we refer to section 4.4.4 an figure 4-12) we may expect a decrease in J_c with increasing sample width. Very wide samples will have large regions at or above the electric field needed for QUILLS to occur before $J_c = 1Am^{-1}$ is reached. The lowering of J_c with sample width is not observed. We consider the movement of the electrons across the sample in an attempt to explain this behavior. We envisage that as the electric field in the sample interior (region V_2 in figure 5-8) will be low and the interior region large. Once a large enough region of the sample reaches the QUILLS condition, electrons will be excited into the upper Landau level. A large number of electrons will build up in the sample interior of the upper Landau level. Using the screening argument of Martin et al. the potential drop at the sample edge will increase, but the potential drop in the sample interior will decrease as V_{xy} remains constant. Now the excited electrons in the upper Landau level will be prevented from crossing the sample by the potential rise due to electrons residing in the sample centre. Therefore any further excited electrons will be kept close to the sample edge and have a large chance of recombining with a hole. An equilibrium is met and breakdown is not measured.

5.7 Summary

Let us now summarise what our cross sample scattering model has predicted. We can explain the observed opposite edge identity in the increase of V_{xx} for samples with short narrow constriction regions. We also predict and observe that dissipation will be measured on the negative edge, before the positive edge and that holes are important in explaining the observed effects. In the case of a constriction in the centre of a sample, we predict and observe that breakdown occurs within the constriction region and we hypothesise that the constriction region is providing a jet of electrons (and holes) in the upper (lower) Landau levels which fire into the wide section of the Hall bar. If the holes are not considered as in BSEH, then we would expect the positive edge to register dissipation before the negative edge. Such a statement is based on the fact that the electrons must scatter toward the positive edge no matter where in the sample they are excited into the upper Landau level. However, we show that by considering the created holes it is the negative edge voltage contacts that register dissipation first.

The length dependence of the breakdown cannot be explained using a microscopic theory. Indeed, one of the difficulties in measuring QHBD is that the exact position within the sample at which breakdown occurs is unknown. The length dependence observed by Komiyama et al. [86] could possibly be explained as follows. The sample is disordered and the current is possibly high enough that there is an impurity somewhere in a long Hall bar that is producing electron-holes pairs. If the region for which QHBD is measured is small and close to the electron injecting end of the Hall bar, then the probability of that impurity residing between the measuring contacts is small. However, if the current direction is reversed, the electrons will travel the length of the Hall bar before reaching the measuring contacts. The impurity that has created dissipation would be upstream of the contacts and we would measure some dissipation. Although this argument may explain the length dependence, it is thought to be an unlikely and unsatisfying explanation for the observed results.

The presence of step-like features, from measurements of V_{xx}, in the NIST wide

samples is remarkable. We now consider reasons why steps are not observed in the majority of samples. Firstly, the experimental conditions may play a factor e.g. the sweep rate of the magnetic field, as mentioned in chapter 2. Aside from experimental factors we will now examine an inter-Landau level tunneling model for wide samples. In our model all the excited electrons have to cross the entire width of the sample at the same rate as they are created. Any variations or randomisation in the rate at which the electrons cross the sample may smooth the step features out. Electron scattering across the sample will be affected by the temperature. Thermal broadening could smear out steps by affecting the scattering rate. Furthermore, electrons crossing the sample may also change the scattering rates locally within the sample. In the sample bulk the electric field due to the line charges at the sample edges is small. Therefore, the potential profile due to an impurity will present a 'hill' for the electron to try to scatter against. A build-up of electrons on the disorder potential of an impurity will inhibit cross sample scattering. The cross sample scattering rate therefore decides the rate at which electrons cross the sample and not the creation rate. For the majority of samples measured QHBD occurs close to the field necessary for BSEH. The electrons will be affected by BSEH before they manage to cross the sample, smoothing any features like steps. Indeed in the samples for which step-like features are observed, the critical current density was much less than that of $1Am^{-1}$. The two samples considered in the previous section had for sample N, $I_c = 220\mu A$ w=$400\mu A$ and sample P I_c =$9.2\mu A$ w=$200\mu m$. These results of $J_c^N = 0.55Am^{-1}$ and $J_c^P = 0.046Am^{-1}$ for samples N and P respectively, show that in such samples, BSEH would be unlikely, and the excited electrons are free to scatter across without deviation and hence steps are observed. Finally, in the case of wide samples it has already been suggested that recombination would occur if there is a large enough build up of electrons in the centre of the sample. Such a process would also smear out any steps.

From the cross sample scattering viewpoint, opposite edge identity in wide samples is possible provided a long enough interval is left between measuring voltage probes. The edge identity can be seen without steps, due to the fact that all the

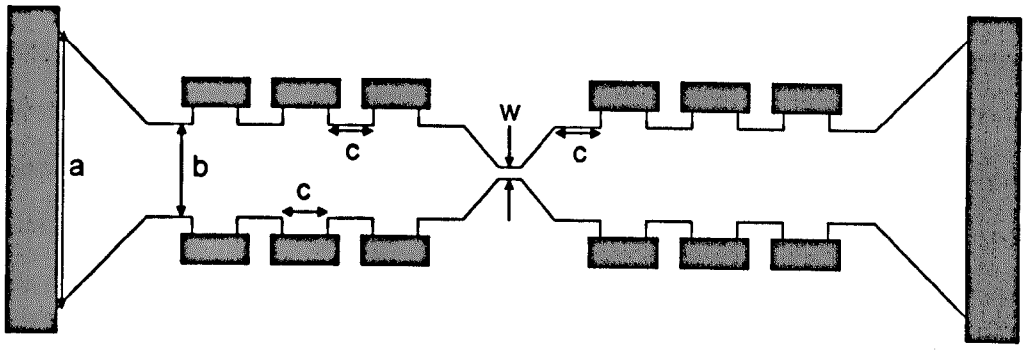

Figure 5-14: An improved design of the constriction samples. The dimensions are a=800μm, b=400μm, c=200μm and w=1-100μm.in 10μm steps. The wide sections at either end of the sample ensure that the hot spots due to current injection do not occur. More contacts are placed in the wide section of the sample before and after the constriction region to investigate hot and cold edge behaviour. The constriction region ensures that breakdown occurs at a known point in the sample.

excited electrons reach the positive edge, which matches the number of holes reaching the negative edge. The rates at which they do so are not relevant and it may be that the cross sample scattering will have affected the rates which the electrons and holes reach the sample edge, hence steps will not be observed.

In summary we find that a microscopic model as yet cannot describe all the observed features of QHBD. However, it does appear from this research that by utilising a microscopic model combined with consideration of the motion of the excited electron-hole pairs, many of the QHBD features can be explained. We believe that further developing this model will bridge the gap between BSEH and the microscopic breakdown model of Martin et al of magneto-exciton formation at charged impurities.

To further investigate the new cross-sample scattering idea it would be interesting to look at a new constriction sample design as shown in figure 5-14. The sample would have a large butterfly configuration for the current injecting probes to ensure that we can neglect the current injection effects. Using a short constriction design would allow the position of QHBD to be known fairly precisely and BSEH to be minimised. The long wide regions on either side of the constriction would allow the hot and cold edge

effects of the wide section of sample before and after a constriction to be investigated fully. Using the constriction region design proposed here, it would be possible to further investigate the reported length dependence [86]. We propose that if the constriction regions were made with varying lengths and widths a phase diagram of QHBD could be constructed. For example the constriction region could have a length of 1-150μm in steps of 10μm and width 1-100μm in steps of 10μm. The critical current density for each constriction could be mapped onto a plot of constriction length versus width. It seems possible that such a plot would show a region of high critical current density for short narrow constrictions (the microscopic regime) and a region of low critical current density (the macroscopic regime). Furthermore, the length dependence will be known to an accuracy of $\pm 10\mu m$ for several widths of sample. Constructing samples that will produce step-like breakdown of V_{xx} is difficult. We suggest a wide sample >100μm would be needed to achieve high electric fields close to the sample edge for low critical current densities. Introducing some impurities so that within the edge region for low current densities there would be an average of 10-20 impurities between contacts would permit inter-Landau level transitions at low current densities. However, as we have already discussed, the potential variation in the bulk of a wide sample may well inhibit the measurement of step-like breakdown.

Chapter 6

Summary of results and future work

6.1 Probing the magneto-compression of Si-donors in a quantum well by magneto-tunneling spectroscopy

The experiments described in chapter 3 have demonstrated that the shallow donor confined in the centre of a semiconductor quantum well heterostructure, provides an ideal system in which the spatial form of an electron wavefunction can be modified by an external perturbation, in this case a strong magnetic field. Simultaneously the form of the wavefunction can be mapped out using the magneto-tunneling spectroscopy technique. To our knowledge this is the first time that such an experiment has been performed. Although the proposed model provides a good fit to the data over an extended range of magneto-compression of the wavefunction, the tunnel distance of the electron, which gives the best fit to our data, is smaller than was initially expected. Possible reasons for this discrepancy are put forward e.g. scattering of tunneling electrons and diffusion of Si-donors from the centre of the quantum well. These ideas could be tested in further experiments by studying the effect of an inter-barrier placed layer of impurities on the tunneling electrons. The effect of charged

impurity scattering may reduce the momentum gained by the tunneling electron by the effect of the Lorentz force due to the magnetic field, $B_{\perp}$, applied perpendicular to the tunneling direction. In addition, the effect of diffusion of donor impurities in the quantum well could be assessed by studying a new series of samples grown at lower temperatures. It would be very interesting to examine magneto-tunneling spectroscopy of many body states e.g. when an electron tunnels into an already neutral donor i.e. $e_{emitter} + D^0_{QW} \rightarrow D^-_{QW}$, where a second electron is weakly bound to the donor, its binding energy increasing with magnetic field [96], [97], [98].

6.2 Quantum Hall effect breakdown

The experiments described in chapter 5 demonstrate that the two very different models for describing the breakdown of the quantum Hall effect (QHBD) are complementary and not contradictory. It appears that the microscopic breakdown that can account for the steps observed by NIST and by us, could act as a trigger for bootstrap electron heating observed in our and other experiments. The onset of dissipation in the longitudinal voltage, V_{xx}, which appears in a step-like manner can be readily described by a microscopic model. However, the dependence of breakdown on sample length reported by other authors (section 4.3.4) cannot be easily described by a microscopic model. Our experiments on the dependence of breakdown on sample width showed that a microscopic model can provide a good description of QHBD in our short narrow constrictions. Bootstrap electron heating describes the QHBD most effectively in our wide long samples. The observed identity of V_{xx} as measured on opposite edges of the sample for narrow constriction samples and the large difference in V_{xx} during QHBD for wide constriction samples is explained using a microscopic model. This is done by considering the motion of the electrons and holes following their production by magneto-exciton formation when the quantum Hall fluid flows past a charged impurity at high velocity. Ideas for further experiments are discussed in the conclusions of chapter 5.

Bibliography

[1] J.W. Sakai et al., Phys. Rev. B **48**, (1993) 5664

[2] S. Komiyama et al, Solid State Communications **54**, (1985) 479

[3] A. M. Martin et al. Phys. Rev. Lett. **91**, (2003) 126803

[4] O. Makarovsky et al. Physica E **12**, (2002) 178

[5] F. Capasso (ED) Physics of Quantum Electron Devices, ISBN 3-540-51128-8

[6] E. Shomburg et al. Appl. Phys. Lett. **74**, (1999) 2179

[7] A. J. Fitzgerald et al. Phys. in Med. and Biol. **47**, (2002) 3865

[8] A. Patanè et al., Phys. Rev. B **65**, (2002) 165308

[9] O. Millo, D. Katz, Y.W. Cao, and U. Banin, Phys. Rev. Lett. **86**, (2001) 5751; R. Rinaldi, T. Johal, M. De Giorgi, A. Passaseo, and R. Cingolani, in Proceedings of the 25th International Conference on the Physics of Semiconductors, Osaka, Japan, edited by N. Miura and T. Ando (Springer-Verlag, Berlin, 2001).

[10] J.F. Zheng et al., Phys. Rev. Lett. **72**, (1994) 1490

[11] B. Grandidier et al., Phys. Rev. Lett. **85**, (2000) 1068

[12] P. Beton et al., Phys. Rev. Lett. **75**, (1995) 1996

[13] E.E. Vdovin et al., Science **290**, (2000) 122

[14] I. P. Roche et al. J. Phys Condens. Matter **2**, (1990) 4439

[15] G. Nachtwei, Physica E 4, (1999) 79

[16] S. Komiyama, Kawaguchi, Phys. Rev. B **61**, (2000) 2014

[17] S.A. Trugman, Phys. Rev. B **27**, (1983) 7539

[18] L. Eaves, F. W. Sheard, Semicond. Sci. Tech. **1**, (1986) 346

[19] O. Heinonen, P.L. Taylor and S.M. Girvin, Phys. Rev. B **30**, (1984) 3016

[20] V. Tsemekhman et al, Phys. Rev. B **55**, (1997) R10201

[21] V.L. Pokrovsky et al, J. Phys. Condens. Matt. **2**, (1990) 93

[22] www.nobel.se/physics/laureates/1998/press

[23] M.J. Kelly, Low Dimensional Semiconductors, 1995 ISBN 0 19 851781 5

[24] J.H. Davies, The Physics of Low Dimensional Semiconductors, 1998, ISBN 0 521 48491 X

[25] M.L. Leadbeater, Thesis submitted to the University of Nottingham 1990

[26] J. M. Chamberlain, R.A. Stradling, Sol. State Comm. **7**, (1969) 1275

[27] F. J. Keller et al, Physics Classical and Modern, ISBN 0-07-023460-4

[28] L.D. Landau, E.M. Lifshitz, Quantum Mechanics, 1991, ISBN 0 08 020940 8

[29] M. E. Cage et al. Semicond. Sci. Technol. **5**, (1990) 351

[30] M.L. Leadbeater, F.W. Sheard, and L. Eaves, Semicond. Sci. Technol. **6**, (1991) 1021

[31] A. Patane et al. Physica B **298**, (2001) 254

[32] I.E. Itskevich et al. Phys. Rev. B **54**, (1996) 16401

[33] P. C. Main et al. Physica E **12**, (2002) 794

[34] R.J.A Hill, Thesis submitted to the University of Nottingham 2002

[35] P. C. Main et al. Phys. Rev. Lett. **84**, (2000) 729; P. C. Main et al. Physica B **256-258**, (1998) 507

[36] R. K. Hayden et al Phys. Rev. Lett. **66**, (1991) 1749

[37] S. Chaudhuri and K.K. Bajaj, Solid State Commun. **52**, 967 (1984); R.L. Greene and K.K. Bajaj, Phys. Rev. B **31**, 913 (1985); **34**, 951 (1986); **37**, 4604 (1988).

[38] R.L. Greene K.K. Bajaj, Phys. Rev. B **31**, (1985) 913

[39] K. Jayakamur et al. Phys. Rev. B **33**, (1986) 4002

[40] S. Chuadhuri K.K. Bajaj, Phys. Rev. B **29**, (1984) 1803

[41] J. W. Sakai et al. Appl. Phys. Lett. **64**, (1994) 2563

[42] J. Bardeen, Phys. Rev. Lett. **6**, (1961) 57

[43] L. Eaves et al. Appl. Phys. Lett. **52**, (1998) 212

[44] T.M. Fromhold, F.W. Sheard et al 22nd Intl. Conference Physics Semiconductors, Vancouver Canada, World scientific Vol **2,** 19959

[45] M.C. Payne, Solid State Phys. **19**, (1986) 1145

[46] N. Mori et al., Microelectronic engineering **63,** (2002) 109; N. Mori unpublished communication, 10 Jan 2000

[47] F. W. Sheard, J. C. Arce, Private Communications 2002-2003

[48] K. v. Klitzing et al. Phys. Rev. Lett. **45**, (1980) 27

[49] R. B. Laughlin Phys. Rev. B **23**, (1981) 35

[50] M. E. Cage et al. Semicond. Sci. Technol. **7**, (1992) 1119

[51] K. v. Klitzing, Rev of Modern Phys. **58**, (1986) 519

[52] Edited by Ehrenreich and D. Turnbull, Quantum Transport in Semiconductor Nanostructures by C. W. J. Beenacker, H. v. Houten, Solid state physics volume **44**, (1991) 1

[53] A.H. Macdonald, T.M. Rice and W.F. Brinkman, Phys. Rev. B **28,** (1983) 3648

[54] M. E. Cage, J. Res. Natl. Inst. Stand. Technol. **102**, (1997) 677

[55] W. Dietsche et al. Surf. Sci. **361/362**, (1996) 289

[56] D. B. Chklovskii et al. Phys. Rev. B **46**, (1992) 4026

[57] K. Oto et al.Physica B **298**, (2001) 18

[58] R. Knott et al. Semicond. Sci. Technol. **10**, (1995) 117

[59] P. F. Fontein et al. Phys. Rev. B **43**, (1991) 12090

[60] S. Kawaji et al. J. Phys. Soc. Japan **67**, (1998) 1110

[61] H. Iizuka S. Kawaji, T. Okamoto, Physica E **6**, (2000) 132

[62] A.J. Matthews Physica E **6**, (2000) 140

[63] L.B. Rigal, Phys. Rev. Lett. **82**, (1999) 1249

[64] T. Sanuki et al. Sol. State Comm. **117**, (2001) 343

[65] L. Eaves et al, Physica E **6**, (2000) 136

[66] S. Kawaji. Physica B **216,** (1996) 393

[67] S. Kawaji, Semicond. Sci. Technol. **11**, (1996) 1546

[68] Takako Shimada et al. Physica B **249-251**, (1998) 107

[69] C. Chaubet, F. Geniet, Phys. Rev. B **58**, (1998) 13015

[70] L. Bliek et al. Surf. Sci. **196**, (1998) 156

[71] G. Boella et al. Phys. Rev. B **50**, (1994) 7608

[72] S. Kawaji et al. J. Phys. Soc. Jap. **63**, (1994) 2303

[73] A. Boisen et al. Phys. Rev. B **50**, (1994)

[74] Y. Kawaguchi et al. Physica B **227**, (1996) 183

[75] A. M. Song, P. Omling, Sol. State Pys., Nanometer Strucutre Consortium (2001) 1

[76] N.Q. Balaban, U. Meirav, H. Shtrikman, Phys. Rev. B **52**, (1995) R5503

[77] B.E. Sagol et al. Phys. Rev. B **66**, (2002) 075305

[78] N.Q. Balaban, U. Meirav, H. Shtrikman, Phys. Rev. Lett. **71**, (1993) 1443

[79] R.J. Haug et al. Solid state Sci. **87**, (1989) 185

[80] K. Morita et al. Physica E **12**, (2002) 169

[81] M. E. Cage et al. Phys. Rev. Lett. **51**, (1983) 1374

[82] C. F. Lavine et al. J. Res. Natl. Stand. Technol. **99**, (1994) 757

[83] V. G. Mokerov et al. Pis'ma Zh. Eksp. Theor. Fiz. **47**, (1998) 59

[84] F. J. Ahlers Semicond. Sci. Technol. **8**, (1993) 2062

[85] S. Kawaji, Physica B **216**, (1996) 393

[86] S. Komiyama, Y. Kawaguchi, Phys. Rev. Lett. **77**, (1996) 558

[87] Y. Kawaguchi et al. Jpn. J.Appl. Phys. **34**, (1995) 4309

[88] I.I. Kaya et al. Phys. Rev. B **58**, (1998) R7536

[89] I. I. Kaya et al, Physica E **6**, (2000) 128

[90] I. V. Lerner, Yu. E. Lzovik, Sov. Phys. JETP **51**, (1980) 588

[91] C. Kallin, B.I. Halperin, Phys. Rev. B **30**, (1984) 5655

[92] A. H. MacDonald, J. Phys. C **18**, (1985) 1003

[93] P. Streda, K. von Klitzing, J. Phys. C **17**, (1984) L483

[94] P. C. Son et al. Phys. Rev. B **42**, (1990) 11267

[95] Y. Kawano, S. Komiyama Physica E **7**, (2000) 799

[96] J.G.S. Lok, A.K. Geim and J.C. Maan Phys Rev B **53**, (1996) 9554

[97] P. O. Holtz et al. Surf. Sci. **361/362**, (1996) 439

[98] J. M. Shi et al. Phys. Rev. B **51**, (1995) 7714